



Defense Threat Reduction Agency
8725 John J. Kingman Road, MS
6201 Fort Belvoir, VA 22060-6201



DTRA-TR-16-65

TECHNICAL REPORT

All-Optical Quasi-Phase Matching for Laser Electron Acceleration

Distribution Statement A. Approved for public release; distribution is unlimited.

June 2016

HDTRA1-11-1-0009

Igor Jovanovic et al.

Prepared by:
The Pennsylvania State
University
228 Reber Building
University Park, PA 16802

DESTRUCTION NOTICE:

Destroy this report when it is no longer needed.
Do not return to sender.

PLEASE NOTIFY THE DEFENSE THREAT REDUCTION
AGENCY, ATTN: DTRIAC/ J9STT, 8725 JOHN J. KINGMAN ROAD,
MS-6201, FT BELVOIR, VA 22060-6201, IF YOUR ADDRESS
IS INCORRECT, IF YOU WISH IT DELETED FROM THE
DISTRIBUTION LIST, OR IF THE ADDRESSEE IS NO
LONGER EMPLOYED BY YOUR ORGANIZATION.

REPORT DOCUMENTATION PAGE

Form Approved
OMB No. 0704-0188

The public reporting burden for this collection of information is estimated to average 1 hour per response, including the time for reviewing instructions, searching existing data sources, gathering and maintaining the data needed, and completing and reviewing the collection of information. Send comments regarding this burden estimate or any other aspect of this collection of information, including suggestions for reducing the burden, to Department of Defense, Washington Headquarters Services, Directorate for Information Operations and Reports (0704-0188), 1215 Jefferson Davis Highway, Suite 1204, Arlington, VA 22202-4302. Respondents should be aware that notwithstanding any other provision of law, no person shall be subject to any penalty for failing to comply with a collection of information if it does not display a currently valid OMB control number.

PLEASE DO NOT RETURN YOUR FORM TO THE ABOVE ADDRESS.

1. REPORT DATE (DD-MM-YYYY) 00-06-2016		2. REPORT TYPE final		3. DATES COVERED (From - To) March 2011-August 2015	
4. TITLE AND SUBTITLE All-Optical Quasi-Phase Matching for Laser Electron Acceleration				5a. CONTRACT NUMBER HDTRA1-11-1-0009	
				5b. GRANT NUMBER	
				5c. PROGRAM ELEMENT NUMBER	
6. AUTHOR(S) Igor Jovanovic, Ming-wei Lin, Bryan Morgan, Abdurahim Rakhman				5d. PROJECT NUMBER	
				5e. TASK NUMBER	
				5f. WORK UNIT NUMBER	
7. PERFORMING ORGANIZATION NAME(S) AND ADDRESS(ES) The Pennsylvania State University 228 Reber Building University Park, PA 16802				8. PERFORMING ORGANIZATION REPORT NUMBER	
9. SPONSORING/MONITORING AGENCY NAME(S) AND ADDRESS(ES) Defense Threat Reduction Agency 8725 John J. Kingman Road Fort Belvoir, VA 22060-6201				10. SPONSOR/MONITOR'S ACRONYM(S) DTRA	
				11. SPONSOR/MONITOR'S REPORT NUMBER(S) DTRA-TR-16-65	
12. DISTRIBUTION/AVAILABILITY STATEMENT This report is available to the public.					
13. SUPPLEMENTARY NOTES					
14. ABSTRACT This report summarizes the technical outcomes of the project "All-Optical Quasi-Phase Matching for Laser Electron Acceleration", a project awarded to the Pennsylvania State University by the Defense Threat Reduction Agency. The results of test particle simulations, particle-in-cell simulations, experimental production of plasma channels, and novel optical diagnostics for radially polarized modes are discussed in detail.					
15. SUBJECT TERMS Lasers, particle acceleration, laser plasma accelerators, direct laser acceleration.					
16. SECURITY CLASSIFICATION OF:			17. LIMITATION OF ABSTRACT	18. NUMBER OF PAGES	19a. NAME OF RESPONSIBLE PERSON
a. REPORT	b. ABSTRACT	c. THIS PAGE			Igor Jovanovic
					19b. TELEPHONE NUMBER (Include area code) 814-867-4329

UNIT CONVERSION TABLE

U.S. customary units to and from international units of measurement*

U.S. Customary Units	<div style="display: flex; align-items: center; justify-content: center;"> <div style="margin-right: 10px;"> </div> Multiply by </div> <div style="display: flex; align-items: center; justify-content: center;"> <div style="margin-right: 10px;"> </div> Divide by† </div>	International Units
Length/Area/Volume		
inch (in)	2.54 $\times 10^{-2}$	meter (m)
foot (ft)	3.048 $\times 10^{-1}$	meter (m)
yard (yd)	9.144 $\times 10^{-1}$	meter (m)
mile (mi, international)	1.609 344 $\times 10^3$	meter (m)
mile (nmi, nautical, U.S.)	1.852 $\times 10^3$	meter (m)
barn (b)	1 $\times 10^{-28}$	square meter (m ²)
gallon (gal, U.S. liquid)	3.785 412 $\times 10^{-3}$	cubic meter (m ³)
cubic foot (ft ³)	2.831 685 $\times 10^{-2}$	cubic meter (m ³)
Mass/Density		
pound (lb)	4.535 924 $\times 10^{-1}$	kilogram (kg)
unified atomic mass unit (amu)	1.660 539 $\times 10^{-27}$	kilogram (kg)
pound-mass per cubic foot (lb ft ⁻³)	1.601 846 $\times 10^1$	kilogram per cubic meter (kg m ⁻³)
pound-force (lbf avoirdupois)	4.448 222	newton (N)
Energy/Work/Power		
electron volt (eV)	1.602 177 $\times 10^{-19}$	joule (J)
erg	1 $\times 10^{-7}$	joule (J)
kiloton (kt) (TNT equivalent)	4.184 $\times 10^{12}$	joule (J)
British thermal unit (Btu) (thermochemical)	1.054 350 $\times 10^3$	joule (J)
foot-pound-force (ft lbf)	1.355 818	joule (J)
calorie (cal) (thermochemical)	4.184	joule (J)
Pressure		
atmosphere (atm)	1.013 250 $\times 10^5$	pascal (Pa)
pound force per square inch (psi)	6.984 757 $\times 10^3$	pascal (Pa)
Temperature		
degree Fahrenheit (°F)	[T(°F) – 32]/1.8	degree Celsius (°C)
degree Fahrenheit (°F)	[T(°F) + 459.67]/1.8	kelvin (K)
Radiation		
curie (Ci) [activity of radionuclides]	3.7 $\times 10^{10}$	per second (s ⁻¹) [becquerel (Bq)]
roentgen (R) [air exposure]	2.579 760 $\times 10^{-4}$	coulomb per kilogram (C kg ⁻¹)
rad [absorbed dose]	1 $\times 10^{-2}$	joule per kilogram (J kg ⁻¹) [gray (Gy)]
rem [equivalent and effective dose]	1 $\times 10^{-2}$	joule per kilogram (J kg ⁻¹) [sievert (Sv)]

* Specific details regarding the implementation of SI units may be viewed at <http://www.bipm.org/en/si/>.

† Multiply the U.S. customary unit by the factor to get the international unit. Divide the international unit by the factor to get the U.S. customary unit.

Abstract

This report summarizes the technical outcomes of the project “All-Optical Quasi-Phase Matching for Laser Electron Acceleration”, a project awarded to the Pennsylvania State University by the Defense Threat Reduction Agency. This work involved one faculty member, one postdoctoral research associate, and two graduate students. One Ph.D. and one M.S. degree were awarded to two students who were fully committed to this project, and are based solely on the technical outcomes described in this report.

Innovative electron acceleration schemes, exhibiting compact size, low weight, and low cost, are desirable for many applications, such as production of high-energy X-rays for detection of special nuclear materials in active interrogation. Direct laser acceleration (DLA) of electrons using the axial electric field of a radially polarized, guided laser pulse has the potential to lead to such compact accelerators. An acceleration gradient on the order of tens of GV/m can be achieved when a radially polarized femtosecond laser pulse with a few TW peak power is focused to ~ 10 μm diameter; as a result, the dimensions of the accelerator can be considerably reduced compared to conventional technologies. Density-modulated plasma waveguides can be used to simultaneously extend the acceleration distance beyond several Rayleigh ranges and to achieve quasi-phase matching between the laser field and the electrons. Through a set of detailed simulations and experiments, the objective of this project was to contribute to the scientific basis for implementation of this laser acceleration technique.

A deterministic test particle simulation has been developed to facilitate the design of the optimal axial structures in density-modulated plasma waveguides for achieving quasi-phase matched DLA. The results indicate that a positively chirped density modulation of the waveguide structure is required to accelerate electrons injected with low initial energies ($\lesssim 20$ MeV). A simple analytical approach for DLA gain estimation was also derived, in which the walk-off effect between the injected electrons and the laser pulse is included. The walk-off effect can be significant and limit the overall DLA efficiency, especially when an ultrashort pulse (few fs pulse duration) is used. Larger axial and radial acceleration regions exist for electrons injected with a higher initial energy ($\gtrsim 20$ MeV). A 3-D particle-in-cell simulation model was developed to gain a detailed understanding of the interactions among the electron bunch, the laser pulse, and the background plasma in the DLA process. When a short bunch is injected, the results confirm that the injection delay is important for controlling the final transverse properties, but it also affects the final energy gain. With a long injected bunch length (of order of a quarter of the plasma wavelength), the enhanced ion-focusing force helps

to collimate the electrons and a relatively small final emittance can be obtained. Microbunching is clearly observed due to the focusing and defocusing of electrons by the radially directed Lorentz force. Results indicate that a moderate laser power is preferred to maintain favorable final bunch transverse properties, while the waveguide length can be extended to obtain a higher maximum energy gain, with the commensurate increase of laser pulse duration and energy.

An important challenge for effective DLA is realizing the guided propagation of a radially polarized laser pulse in a density-modulated plasma waveguide. An all-optical method based on the ignitor-heater scheme was experimentally implemented to machine density-modulated plasma channels. Experimental results show that it is important to prevent the ionization of gas atoms by the heater itself; otherwise, the heating of plasma by the inverse bremsstrahlung mechanism is significantly inhibited. A density-modulated plasma structure was demonstrated with argon plasma using an intensity-modulated ignitor, which serves as a proof-of-principle foundation for producing the density-modulated plasma waveguides suitable for DLA in the future. In addition, micrometer-scale, high-aspect-ratio supersonic gas jet nozzles were designed and fabricated by use of metal additive manufacturing to support the DLA research. The designs were simulated using the COMSOL Multi-Physics framework with high Mach number fluid modeling. Nozzles were manufactured in titanium and aluminum and the surface quality of the nozzles were evaluated with optical interferometry and computed tomography.

To characterize the radially polarized laser pulse, an angle-multiplexed spatial-spectral interferometric technique able to extract the polarization state and relative spectral phase of an ultrashort laser pulse, was developed and experimentally demonstrated. In this device, the interferogram is produced between an arbitrary polarized signal pulse and two orthogonal linearly polarized reference pulses. This technique is limited by the interferometric phase drift, necessitating a calibration procedure prior to data collection. The accuracy of measurement was verified by reconstructing the known relative spectral phase arising from material dispersion and the known elliptical polarization state. Measurement of the relative spectral phase and the spatially variable polarization state of a radially polarized pulse was also demonstrated.

Contents

Abstract	i
Contents	iii
List of Figures	v
List of Tables	xi
1 Introduction: the major goals of the project	1
2 Modeling of DLA in plasma channels	4
2.1 Test particle simulations for DLA	4
2.1.1 Development of the test particle model	5
2.1.2 Results of test particle simulations and discussion	7
2.1.3 Conclusion from test particle simulations	11
2.2 PIC simulations of DLA	12
2.2.1 Development of the PIC model	12
2.2.2 Results of the PIC simulations and discussion	15
2.2.2.1 Effect of the electron bunch injection delay	15
2.2.2.2 Effect of the electron bunch length	18
2.2.2.3 Effect of the transverse electron bunch size	21
2.2.2.4 Effect of the laser power and waveguide length	22
2.2.3 Conclusion from DLA PIC simulations	24
3 Fabrication of density-modulated plasma channels	26
3.1 Experimental setup for fabrication of plasma channels	27
3.2 Experimental results in production of plasma channels	33
3.2.1 Fabrication of argon plasma channels	33
3.2.2 Conclusions drawn from experimental results	38
3.3 Micrometer-scale supersonic gas jet design, simulation and fabrication . .	39
3.3.1 Finite element analysis for nozzle design	41
3.3.1.1 Frictional pressure loss simulation with stability extension	42
3.3.1.2 Mach number and shock wave analysis	43
3.3.2 Nozzle fabrication	47
3.3.3 Conclusions drawn from nozzle design and fabrication	51
4 Radially polarized ultrashort pulse characterization	53
4.1 Generation of ultrafast radially polarized laser pulses	53

4.2	Characterization of ultrafast radially polarized laser pulses	55
4.2.1	Description of the method	55
4.2.2	Experimental setup	58
4.2.3	System calibration	59
4.2.4	Measurement of a linearly polarized pulse with dispersion	62
4.2.5	Radially polarized pulse measurement	63
4.2.6	Summary of the results	65
5	Conclusion and perspective	66
5.1	Discussion of Results	66
5.1.1	Injection of electrons for DLA	67
5.1.2	Maintenance of the transverse bunch properties	67
5.1.3	Improvement of the heating efficiency of plasmas for plasma waveguide production	68
5.2	Perspective: Future development of DLA experiments	68
	Bibliography	70

List of Figures

2.1	(a) Dependence of dephasing length L_c on electron kinetic energy for $n_e = 2.5 \times 10^{18} \text{ cm}^{-3}$, $1.25 \times 10^{19} \text{ cm}^{-3}$, and $2.5 \times 10^{19} \text{ cm}^{-3}$, with $w_0 = 8.5 \text{ }\mu\text{m}$ and $\lambda = 800 \text{ nm}$. (b) Quasi-phase-matched DLA is performed in a preformed density-modulated plasma waveguide.	5
2.2	Dependence of the electron energy gain ΔT on propagation distance z for electrons with different initial energies in plasma waveguides with (a) constant and (b) chirped density modulation.	7
2.3	(a) Dependence of the electron energy gain ΔT on propagation distance z in plasma waveguides for electrons of $T_0 = 40 \text{ MeV}$ with laser pulse durations $\tau_p = 5 \text{ fs}$, 10 fs , 20 fs , 40 fs , and 80 fs . The other parameters are the same in Fig. 2.2. (b) Comparison of estimated DLA electron energy gain ΔT from Eq. 2.4 to the results obtained by the test particle simulation.	9
2.4	(a) Final electron energy gain ΔT as a function of electron initial phase ϕ_0 for electrons of $T_0 = 5 \text{ MeV}$, 15 MeV , 40 MeV and 100 MeV . (b) Final electron energy gain ΔT as a function of electron initial radial position r_0 for electrons of $T_0 = 5 \text{ MeV}$, 15 MeV , 40 MeV , and 100 MeV and 2-mm long plasma waveguide. The other parameters are the same as in Fig. 2.2.	10
2.5	Snapshots of (a) axial E_x and (b) transverse E_y electric fields of a 20-fs, 0.5-TW, radially polarized laser pulse with a diameter $w_D = 15 \text{ }\mu\text{m}$; (c) illustration of a density-modulated plasma waveguide, along with the axial position x and the bunch propagation time t ; (d) transverse plasma density profile $n_r(y, 0)$ defined for the waveguide regions; (e) ionization of neutral hydrogen gas by the electric field illustrated in (a) and (b).	14
2.6	(a) On-axis axial field E_x and the plasma electron density n_{pe} with laser power $P = 0.5 \text{ TW}$. (b) Comparison of the plasma electron density n_{pe} and on-axis bunch density n_b when 6-fs bunches, with $\tau_d = 6.2 \text{ fs}$ and 0, are injected, with other conditions corresponding to (a). Insets in (a) and (b) show the corresponding 2-D total charge ρ_t and bunch density distributions.	15
2.7	Variation of the (a) electron distribution ($ z \leq 0.4 \text{ }\mu\text{m}$), (b) trace space, (c) energy spectrum, and (d) θ_y distribution for an bunch injected with $\tau_d = 6.2 \text{ fs}$, $T_0 = 40 \text{ MeV}$, $\tau_b = 6 \text{ fs}$, and propagates in a 2.1-mm long plasma waveguide.	17
2.8	(a) Bunch emittance $\epsilon_{N,y}$ as a function of the propagation time t for different time delays $\tau_d = 6.2 \text{ fs}$, 3.2 fs , 0 , and -3 fs . Comparison for the final (b) trace space distributions, (c) electron distributions, (d) energy spectra, and (e) θ_y distributions for bunches injected with $\tau_d = 3.2 \text{ fs}$, 0 , and -3 fs	18

2.9	(a) Comparison of the on-axis bunch density n_b and plasma electron density n_{pe} at $t = 0.832$ ps for bunches injected at $\tau_d = 0$ with durations $\tau_b = 6$ fs, 13 fs and 20 fs. The corresponding (b) variations of the 2-D bunch density from $t = 0.166$ ps to $t = 0.832$ ps and (c) the trace space distributions at $t = 0.832$ ps. Inset in (a) shows the corresponding on-axis axial field E_x with the bunch of $\tau_b = 20$ fs.	19
2.10	(a) Bunch emittance $\epsilon_{N,y}$ as a function of propagation time t for bunches with durations $\tau_b = 13$ fs and 20 fs. (b) Sampled trace space distributions and final (c) electron distributions, (d) energy spectra and (e) θ_y distributions.	19
2.11	(a) Sampled 2-D bunch density variation in the entire propagation for a 20-fs injected bunch. The corresponding on-axis axial field E_x , bunch density n_b , axial P_x and transverse P_y momentum distributions at (b) $t = 0.83$ ps, (c) $t = 5.83$ ps, and (d) $t = 6.83$ ps	21
2.12	(a) Bunch emittance $\epsilon_{N,y}$ as a function of propagation time t for bunches with sizes $w_b = 9$ μm and 15 μm . (b) Sampled trace space distributions for $w_b = 9$ μm . Final (c) energy spectra and (d) θ_y distributions for $w_b = 9$ μm and 15 μm	22
2.13	Effect of the laser power ($P = 1$ TW and 2 TW). (a) Comparison of the on-axis bunch density n_b and plasma electron density n_{pe} at $t = 0.832$ ps for bunches injected at $\tau_d = 0$ with durations $\tau_b = 6$ fs and 20 fs. (b) The emittance $\epsilon_{N,y}$ as a function of propagation time t . (c) Final energy spectra for bunch with $\tau_b = 20$ fs. (d) The final trace space and electron distributions for bunch with $\tau_b = 20$ fs with laser power $P = 2$ TW. The waveguide length $L_{wg} = 2.1$ mm is fixed for all cases.	23
2.14	(a) Dependence of C_{env} on the variable injection delay τ'_d for waveguide length $L_{wg} = 2.1$ mm and 4.3 mm. (b) Final energy spectrum for the bunch of $\tau_b = 20$ fs injected at $\tau_d = 0$, with waveguide of $L_{wg} = 4.3$ mm and laser power of $P = 0.5$ TW. (c) The corresponding emittance $\epsilon_{N,y}$ change with time t . Final (d) trace space and electron distributions and (e) on-axis bunch density n_b and electron momentum distributions.	24
3.1	System design for fabrication of density-modulated plasma channels. . . .	27
3.2	(a) High-energy laser: Nd:YAG pump laser (top), the multi-pass CPA amplifier (right) and the grating-pair compressor (left). The output (b) intensity profile and (c) spectrum of the laser pulse from the compressor . . .	28
3.3	Layout of the experimental system for DLA	28
3.4	Detailed experimental layout for the fabrication of plasma waveguides using the laser machining technique	29
3.5	(a) Experimental setup in the vacuum chamber: gas jet (at center), pump beam line (red), ignitor beam line (purple) and image system (orange), heater beam line (green), side scattering image (blue), interferometer probe beam (pink, the relay image/longitudinal shadowgram (fuchsia) and the transverse shadowgram (light green). (b) Illustration for the propagation of probe beams of the longitudinal and transverse shadowgrams when diagnosing a plasma structure above the gas nozzle.	30

3.6	Experimentally obtained (a) interferogram and (b) side scattering image of a N plasma column produced by a laser pulse with the peak intensity 4.8×10^{16} W/cm ² at a 700 psi backing pressure of the N gas to the gas valve. Interferograms (c) with a N plasma column with 100 psi backing pressure and (d) without plasma in the target space; (e) retrieved plasma density distribution from (c) and (d).	31
3.7	Stainless steel mask is used to create the ignitor intensity modulation with a (a) constant and (b) chirped period. (c) On-target ignitor intensity patterns with various mask pattern.	32
3.8	(a) Transverse (upper) and longitudinal (right) shadowgrams of the Ar plasma channel produced with 3.7-mJ ignitor and 36-mJ heater, along with the corresponding interferogram (lower) sampling the central region. With the same parameters, transverse shadowgrams are shown in cases when only the (b) ignitor and (c) heater was used. Detailed parameters are provided in the text.	34
3.9	Transverse (left) and longitudinal (right) shadowgrams, along with the interferogram (center) measured for the study of the effect of the heater energy on Ar plasma channel production when the ignitor energy was set to (a) 3.7 mJ and (b) 6.3 mJ. The other parameters were the same as those producing the results in Fig. 3.8.	35
3.10	With 6.3-mJ ignitor and 36-mJ heater, the (a) transverse shadowgrams and (b) corresponding interferograms for a series of 5 measured Ar plasma channels. The other parameters were the same as those those producing the results in Fig. 3.8.	36
3.11	Transverse (left) and longitudinal (right) shadowgrams, along with the interferogram (center) measured when studying the effect of the heater delay on Ar plasma channel production with 6.3-mJ ignitor and 36-mJ heater. The other parameters were the same as those producing the results in Fig. 3.8.	36
3.12	With 6.3-mJ ignitor and 36-mJ heater, (a) measured transverse shadowgrams and interferograms of Ar plasma channels for various probe delays and (b) retrieved plasma density profiles around the density peaks at selected probe delays. The other parameters were the same as those producing the results in Fig. 3.8.	37
3.13	With 6.3-mJ ignitor and 36-mJ heater, intensity-modulated ignitor (upper) and the measured transverse shadowgrams (center) and interferograms (lower) of the corresponding Ar plasma structure. The other parameters were the same as those producing the results in Fig. 3.8.	38
3.14	An example de Laval nozzle designed to produce the gas profile for an optical plasma waveguide. The nozzle begins as a cylindrical flow at the left, and transitions to rectangular flow at the critical point; (a) parallel projection of the nozzle; (b) transparent offset projection of the nozzle that shows the transition from a cylindrical flow system to an asymmetric rectangular flow system.	40
3.15	Offset transparent rendering of the de Laval micrometer-scale supersonic gas jet used in DLA experiments.	40

3.16	Depiction of the model for the frictional pressure loss simulation. The inlet boundary condition is identified by the blue disk in the right image. The inlet feed pipe is 10 mm in length with a 1 mm diameter. The constriction to the critical point is 4 mm in length and constricts from a 2 mm diameter to a 0.6 mm diameter.	41
3.17	Nitrogen nozzle target gas density isosurface plot from the frictional pressure loss simulation with a 100 psi reservoir pressure. The target gas density is reached within the nozzle expansion chamber prior to the exit into the vacuum chamber.	43
3.18	Nitrogen nozzle target gas density isosurface plot from the frictional pressure loss simulation with a 190 psi reservoir pressure. The target gas density is reached after the nozzle exit in the vacuum chamber.	43
3.19	Nitrogen gas density at various heights across the width of the nitrogen nozzle outlet for the frictional pressure loss simulation with the 2 mm straight extension at 190 psi reservoir pressure. The target nitrogen gas density is reached at 400 μm above the center of the slit jet outlet.	44
3.20	Isosurface 3D plot of the supersonic velocity regions from Mach 1 to Mach 3 for the nitrogen supersonic gas jet nozzle without the stability extension at a 180 psi static reservoir pressure. The scale indicates the Mach number and corresponding color per isosurface. The left image displays the continuous acceleration from the critical point. The right image depicts the expanding and accelerating gas in the vacuum chamber represented by the red Mach 3 isosurface plot.	45
3.21	Isosurface plot of the subsonic regions for the nitrogen gas jet without the stability extension at a 180 psi reservoir pressure.	45
3.22	Isosurface plot of the Mach 1 ($M=1$) regions at the beginning of the expansion length and at the area around the perimeter of the nozzle exit.	46
3.23	Isosurface plots of the Mach 1 ($M=1$) regions at the beginning of the expansion length and at the area around the perimeter of the nozzle exit. The left image is the shock wave generated by the flow exiting the nozzle, and the right image is the transition from subsonic to supersonic flow after the critical point.	46
3.24	EOS M280 DMLS platform was used to manufacture the micrometer supersonic gas jet.	48
3.25	Three concept nozzles printed in titanium still mounted to the solid titanium build plate. The left nozzle has a 6 mm long slit outlet, the center nozzle a 2 mm long slit outlet, and the right nozzle a 1.4 mm diameter circular outlet.	48
3.26	Final nitrogen supersonic micrometer gas jet nozzle created in titanium after post processing. The left image is a view of the top of the nozzle with the outlet stem, and the right image is a view of the bottom of the nozzle with the 2 mm diameter inlet.	49
3.27	Optical profilometry images of the titanium nozzle surfaces. The left image is of the weld surface. The center image is of an exterior wall surface of the nozzle base. The right image is an interior surface image taken near the exit plane of the expansion length, and the transition to a top weld surface can be seen at the far right of the image. For all images blue is the lowest height and red is the highest point.	50
3.28	CT scan of a titanium nitrogen nozzle expansion length.	51

4.1	Configuration of the LC polarization converter.	54
4.2	(a) The LC radial polarization converter; (b) intensity distributions of converted, radially polarized laser pulses (first column) and corresponding horizontal (second column) and vertical (third column) components taken with a optical analyzer.	54
4.3	(a) Principle of the angle-multiplexed spatial-spectral interferometric technique. After being dispersed by a grating, two reference pulses and the signal pulse are vertically multiplexed on a cylindrical mirror and reflected at small angles θ_1 and θ_2 . A CCD camera is used to record the 2D interference pattern produced at the focus of the cylindrical mirror. (b) The orientation angle $\psi(\omega)$ and the ellipticity angle $\chi(\omega)$ of the polarization ellipse	56
4.4	The spectral phase and polarization ellipse retrieval algorithm using simulated data. (a) Simulated interferogram corresponding to two orthogonal reference pulses and a signal pulse. The reference pulses have a group delay dispersion (GDD) of -100 fs^2 and -30 fs^2 and a third-order dispersion (TOD) of -250 fs^3 and -50 fs^3 , respectively. The signal pulse has a GDD of 2000 fs^2 and a TOD of 1200 fs^3 . The phase shift δ between the two polarization components of the signal pulse varies between $-\pi$ to π . (b) The 1D Fourier transform of this interferogram along x -dimension. (c) In the k_x -domain, either the top or bottom sidebands were filtered out. (d) and (e) The extracted sidebands were inverse-Fourier transformed back to the x -domain. (f) and (g) The resulting product of the interfering fields is divided by the spectral field of the reference pulse to obtain the spectral field and phase difference $\phi_i^s(\omega) - \phi_i^r(\omega)$ of the corresponding polarization components of the signal and reference pulses. (h) The spectral phase difference $\delta(\omega)$ between the two polarization components of the signal pulse was calculated by taking the sum of the extracted value of $\Delta\phi(\omega)$ and $\Delta\phi^r(\omega)$. (i) The polarization ellipse parameters at central wavelength ($\lambda_0 = 800 \text{ nm}$) was retrieved by using the extracted spectral fields $E_1^s(\omega)$, $E_2^s(\omega)$ and spectral phase difference $\delta(\omega)$	57
4.5	(a) The schematic illustrates the experimental geometry used for angle-multiplexed spatial-spectral interferometry technique. M, mirror; SM, spherical mirror. Polarization of the signal beam is rotated to an arbitrary polarization state by a zero-order wave plate ($\lambda/4$ or $\lambda/2$) after reflection from the beamsplitter BS_1 . Two zero-order half-wave plates ($\lambda/2$) after two linear polarizers (LP_1 and LP_2) keep the polarization of two reference pulses highly orthogonal. Two delay lines (Delay1, Delay2) equipped with two high precision translation stages provide correct timing between signal pulse and two reference pulses. Three beams are vertically multiplexed at zero delay and collimated before being spectrally dispersed on the CCD using the grating (GR) and the cylindrical mirror (CM). (b) Photo for the device.	59
4.6	Experimental interferograms with three different temporal delays τ between the two reference pulses: (a) $\tau < 0$, (b) $\tau = 0$, (c) $\tau > 0$. The extracted spectral phase shift $\delta(\omega)$ corresponding to respective temporal delays of: (d) $\tau < 0$, (e) $\tau = 0$, (f) $\tau > 0$	60

- 4.7 Effect of measured fast phase jitter: (a) phase drift corresponding to the relative phase difference between the two reference arms; drifts in corresponding polarization ellipse parameters, such as (b) ellipticity angle $\Delta\chi_o^r$ and (c) orientation angle $\Delta\psi_o^r$. The corresponding drifts for those quantities is also measured over longer time scales and shown in (d)–(f). . 61
- 4.8 (a) Experimental spectral interferogram of a signal pulse linearly polarized at 45° passing through SF11 glass rod and interfering with two orthogonally polarized reference pulses. (b) The retrieved spectrum (red) is compared to the measured spectrum (blue). The extracted net spectral phase (green) introduced by the SF11 glass rod is also compared to the calculated phase (magenta) due to material dispersion. (c) Extracted polarization angles for several tested polarization states are plotted against the set linear polarization angle of the signal. 62
- 4.9 (a) Measured far-field image of a radially polarized beam. Also shown is the far-field image of the same beam after passing through a rotating linear analyzer set at (b) 0° , (c) 45° , (d) 90° , and (e) 135° 63
- 4.10 Two interferograms were taken with two reference beams interfere with the sampled signal beam taken at point 1 (a) and point 2 (b), respectively. (c) Extracted relative spectral phases corresponding to two sampling points (1 and 2) were compared. The inset indicates the sampling position in the beam. (d) The ellipse orientation angles ψ that represent sampled points (1 and 2) were calculated and compared. 64
- 5.1 Illustration of a possible future DLA configuration. An electron bunch from the output of a LWFA is injected into a density-modulated plasma waveguide for subsequent DLA. 69

List of Tables

2.1	Assigned lengths, $L_{d,L}$ and $L_{d,H}$ (in μm), for low- and high-density regions in each section of the plasma waveguide for DLA of electrons with initial energies $T_0 = 5$ MeV and 15 MeV shown in Fig. 2.2(b).	8
3.1	Static reservoir pressure and temperature with the inlet flow pipe diameter and critical point diameter used for the helium and nitrogen de Laval nozzle solutions.	42

Chapter 1

Introduction: the major goals of the project

Radiation signatures of fissile materials, such as highly penetrating neutrons and gamma-rays, are most promising for their detection at long range. Since the available spontaneous radiation signatures are usually rare and emitted into the full solid angle, active interrogation systems such as those that utilize high-energy X-rays to induce photofission or nuclear resonance fluorescence are a better alternative. High-energy interrogation photons can be generated from electron beams produced by particle accelerators using processes such as bremsstrahlung or inverse Compton scattering. Innovative accelerator schemes meeting the typical specifications for this application are required, exhibiting compact size, low weight and low cost.

Direct laser acceleration (DLA) of electrons, such as inverse Cherenkov acceleration, has the potential to meet the requirements for future compact accelerator driven active interrogation systems, particularly because of its low peak power requirement. In DLA, electrons are accelerated by the axial component of the electric field of a focused, radially polarized laser pulse. The acceleration gradient scales as the square root of the laser peak power, and is estimated to be 77 GV/m for 800 nm laser wavelength with peak power of 0.5 TW and 8.5 μm mode radius. Therefore, field gradients on the order of hundreds of GV/m are expected even below TW peak power available from state-of-the-art, compact, high repetition rate laser systems. These peak powers are rapidly becoming available from the state-of-the-art fiber sources.

The objective of this project has been to tackle a selected set of important DLA challenges and thus materially contribute to the scientific basis for low-energy implementation of high-gradient DLA, a high-gradient acceleration technology holding significant promise for compact active sensing systems for fissile materials. Two significant challenges associated with DLA exist and have to be addressed. They are (1) realization of

guided propagation of ultraintense pulses over extended distances and (2) phase matching between the propagating electrons and laser pulses. Optical guiding in DLA using a preformed plasma waveguide can extend the accelerating distance. Density-modulated plasma waveguides with proper axial structure could be used for the quasi-phase matching (QPM) between the laser pulses and electrons. Therefore, a net energy gain for the electrons can be produced by breaking the symmetry between acceleration and deceleration phases.

This work had two underlying thrusts: (1) develop a detailed model involving novel methods for all-optical control of QPM in DLA, and (2) conduct critical experiments to validate the key assumptions and predictions of this model, with significant impact on a broader set of promising laser acceleration schemes. The work was proposed to be conducted in two phases, corresponding to Base and Option period of the grant. In Phase I of this work the necessary modeling and experimental work was performed to demonstrate the feasibility of all-optical QPM control. In the proposed Phase II the goal was to perform an integrated experimental demonstration of all-optically controlled DLA with laser-injected electrons. Major tasks are summarized as follows:

Phase I (Base Period)

- Task 1: Model propagation of femtosecond radially polarized laser pulses in plasma waveguides.
- Task 2: Design of plasma channel shaping system.
- Task 3: Demonstrate an all-optical method for tailoring plasma waveguides.
- Task 4: Develop new spatially and temporally resolved diagnostics.
- Task 5: Generate radially polarized femtosecond pulses for use in DLA.
- Task 6: Characterize propagation of femtosecond radially polarized pulses in plasma waveguides.

Phase II (Option Period)

- Task 7: Design and construct a laser-based electron injection system.
- Task 8: Integrated demonstration of DLA on laser-injected electrons.

During the project, most of the research goals in Phase I have been accomplished. Phase II of the project was not carried out since the project did not extend into the Option Period. The content of this report is summarized as follows.

Chapter 2 show the results under the development of simulation models for DLA (Task 1). A simple test particle model has been developed to study the DLA performance. The axial density modulation structure in a plasma waveguide is optimized for

different injection energies of the electrons. A simple analytical approach for the estimation of DLA energy gain is presented and the effect of injection phase and acceleration of electrons injected at various radial positions is also studied. More importantly, a 3D particle-in-cell simulation model is developed to study DLA in density-modulated plasma waveguides. The goal of this work is to understand how the initial parameters of the injected bunch, such as the bunch injection delays, bunch lengths and bunch sizes, can be chosen to optimize the DLA performance. The results help to understand interactions among the electron bunch, the laser pulse and the background plasma in the QPM DLA process.

In Chapter 3, an all-optical method, based on the igniter-heater scheme for plasma waveguide fabrication, designed and experimentally implemented to machine the density-modulated plasma structure with argon gas (Tasks 2 and 3), is described. The goal of this work has been to demonstrate the method developed for the fabrication of density-modulated plasma waveguides as the first step to realize a DLA platform (Task 6). Detailed analysis of a room-temperature gas nozzle design using analytical and finite-difference multi-physics models, coupled to testing of novel fabrication methods based on additive manufacturing in polymers and metals are also reported.

In Chapter 4, development of a novel angle-multiplexed spatial-spectral interferometry technique used for characterizing the generated, radially polarized laser pulses is reported (Tasks 4 and 5). The interferometric technique is able to extract the polarization state and relative spectral phase of an ultrashort laser pulse. Measurement of the relative spectral phase and the spatially variable polarization state of a radially polarized pulse was also demonstrated.

The main conclusions and perspectives resulting from this work are summarized in Chapter 5. The technical report ends with Chapter 6, where the executive summary is provided.

Chapter 2

Modeling of DLA in plasma channels

The development of simulation models for DLA and their application to study the QPM conditions for DLA in a laser-machined plasma waveguide is introduced in this Chapter to address the Task 1 of this research project. In Sec. 2.1, a test particle model is described, which was developed to simulate the trajectory and momentum changes of electrons when interacting with laser field in DLA and is used to optimize DLA designs for the axial density structure of the plasma channels. Closed-form descriptions of a guided radially polarized laser pulse and the plasma waveguide are provided, along with the relativistic equations of motion that govern the electron acceleration by the laser field. More importantly, 3-D plasma particle-in-cell (PIC) simulations of DLA have been conducted to elucidate the physics of electron beam dynamics and resolve how initial parameters of the injected electron bunch can be chosen to optimize DLA, as described in Sec. 2.2. Selected time delays with respect to the laser pulse, bunch lengths, and bunch sizes are assigned to the injected electrons in a series of simulations. The energy spectrum, trace space, emittance, and density (or electron particle) distribution of the injected bunch are analyzed to understand the variation of bunch properties throughout the DLA process and how they relate to the initial conditions.

2.1 Test particle simulations for DLA

In this section, we describe the development of a test particle model and its application to study the QPM conditions for DLA in a laser-machined plasma waveguide. This model is developed to study the optimal axial density modulation structure of plasma waveguides for laser pulses to efficiently accelerate co-propagating electrons. A simple analytical approach is also presented, which can be used to estimate the energy gain in DLA. The analytical model is validated by the test particle simulation. The effect

of injection phase and acceleration of electrons injected at various radial positions are studied. The results indicate that a positively chirped density modulation of the waveguide structure is required to accelerate electron with low initial energies, and can be effectively optimized. A wider tolerance on the injection phase and radial distance from the waveguide axis exists for electrons injected with a higher initial energy.

2.1.1 Development of the test particle model

We have developed a DLA test particle model by considering the dispersion relation of a guided radially polarized laser pulse in a preformed plasma waveguide. The refractive index η associated with the guided propagation of a laser pulse in a plasma waveguide is [1]

$$\eta = (1 - \omega_p^2/\omega^2 - 8c^2/\omega^2 w_0^2)^{1/2}, \quad (2.1)$$

where ω_p is the plasma frequency, ω is the laser frequency, w_0 is the guided mode radius, and c is the speed of light in vacuum. The phase velocity $v_{ph} = c/\eta$ and group velocity $v_g = c\eta$ characterize the propagation of the guided laser pulse. Electrons fall out of phase by π with respect to the laser field after a dephasing length $L_c = \pi/|k_l - k_e|$, determined by the laser wave vector $k_l = 2\pi\eta/\lambda$ (with the laser wavelength λ) and $k_e = \omega/v_e$ being the equivalent wave vector for the electrons with velocity v_e . Figure 2.1(a) shows the dependence of the dephasing length L_c on the electron kinetic energy for three different plasma electron densities n_e . For low energies of injected electrons, the dephasing length changes during the acceleration process and a plasma structure with variable period is required to satisfy QPM conditions.

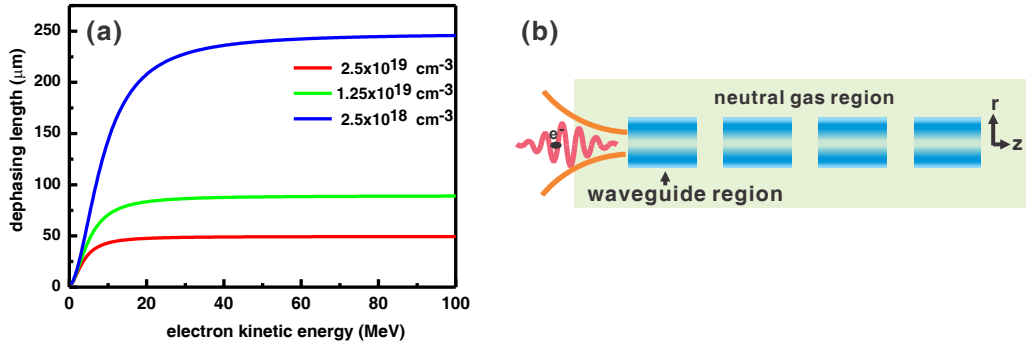


FIGURE 2.1: (a) Dependence of dephasing length L_c on electron kinetic energy for $n_e = 2.5 \times 10^{18} \text{ cm}^{-3}$, $1.25 \times 10^{19} \text{ cm}^{-3}$, and $2.5 \times 10^{19} \text{ cm}^{-3}$, with $w_0 = 8.5 \mu\text{m}$ and $\lambda = 800 \text{ nm}$. (b) Quasi-phase-matched DLA is performed in a preformed density-modulated plasma waveguide.

As illustrated in Fig. 2.1(b), a density-modulated plasma waveguide is considered in the test-particle simulation, which can be fabricated by the laser machining technique [2]. Using a gas target of a low atomic number Z (*e.g.*, hydrogen or helium), low and high

plasma density regions designed for meeting the QPM condition can be produced when the laser pulse passes through the waveguide and the neutral gas regions. The low plasma density regions are those waveguide regions in Fig. 2.1(b) which have the density profile with a lowered on-axis electron plasma density. Since the plasma has reached its highest ionization state in these low plasma density regions, the electron density profile is not further reshaped during the passage of the DLA drive pulse. The uniformly distributed, high-density plasma regions are created by the optical-field-ionization of the gas atoms when the laser pulse passes the neutral gas regions. In case a 0.5-TW, radially polarized laser pulse with a peak intensity $>10^{17}$ W/cm² is used, the low-Z neutral gas becomes fully ionized within a few optical cycles in the laser pulse front foot. As a result, the pulse experiences an uniformly distributed plasma for most of its duration, rather than being considerably defocused by ionization-induced refraction. Throughout most of the laser pulse duration, the pulse experiences alternating low and high plasma density regions along the propagation distance. As long as the neutral gas regions are shorter than the Rayleigh length for the guided mode radius, guiding of the laser pulse can be sustained with high efficiency over the waveguide length. The electron axial density profile chosen the simulation is $n_{e0}(z) = n_{e,L} + (n_{e,H} - n_{e,L})H(z - \lambda_{L,n})[1 - H(z - \lambda_{m,n})]$, where $n_{e,L}$ and $n_{e,H}$ are the plasma densities in low- and high-density regions, respectively, $\lambda_{m,n} = \lambda_{L,n} + \lambda_{H,n}$ is the length of n 'th modulation period composed of low- and high-density regions with lengths $\lambda_{L,n}$ and $\lambda_{H,n}$, respectively, and H is the Heaveside step function. Plasma electron densities chosen for the low and high density regions are $n_{e,L}=2.5 \times 10^{18}$ cm⁻³ and $n_{e,H}=1.25 \times 10^{19}$ cm⁻³, respectively. The electron trajectory and energy are calculated from the relativistic equation of motion $d\mathbf{p}_e/dt = q_e(\mathbf{E} + \mathbf{v}_e \times \mathbf{B})$ and the energy relation $m_e c^2 d\gamma/dt = q_e(\mathbf{v}_e \cdot \mathbf{E})$. The electromagnetic field of a co-propagating, guided, radially polarized laser pulse in a density-modulated plasma waveguide is considered as the driving field. For a guided radially polarized laser pulse, the electric field $\mathbf{E} = \hat{r}E_r + \hat{z}E_z$, in which the radial field E_r is [1]

$$E_r = E_0 \theta (r/w_0) \exp[-(r/w_0)^2] \exp[-2 \ln 2 (z - z_p)^2 / L_p^2] \cos(\phi) \quad (2.2)$$

and the axial field E_z is

$$E_z = E_0 \theta^2 (1 - r^2/w_0^2) \exp[-(r/w_0)^2] \exp[-2 \ln 2 (z - z_p)^2 / L_p^2] \sin(\phi), \quad (2.3)$$

for a Gaussian pulse at position z_p , with the phase ϕ , the beam diffraction angle $\theta = \lambda/\pi w_0$ and the pulse length L_p (measured as FWHM of a Gaussian longitudinal pulse envelope). The characteristic field amplitude E_0 relates to laser peak power P_0 as $E_0 = (8c\mu_0 P_0 / \pi w_0^2 \theta^2)^{1/2}$ [3]. The azimuthal magnetic field is defined as $B_\theta = (\eta/c) E_r$. The phase of the field is represented by $\phi = \omega(t - z\eta/c)$. The change of phase and position

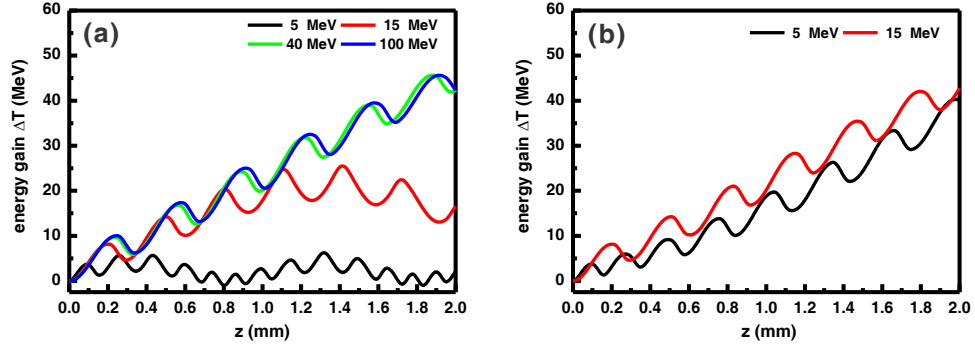


FIGURE 2.2: Dependence of the electron energy gain ΔT on propagation distance z for electrons with different initial energies in plasma waveguides with (a) constant and (b) chirped density modulation.

of the laser pulse can be described by $d\phi/dt$ and $dz_p/dt = v_g(z_p)$. A 20-fs ($L_p=6 \mu\text{m}$), 0.5-TW laser pulse, with maximum axial field amplitude $E_{z,max} = E_0\theta^2 \simeq 77 \text{ GV/m}$ and dispersion relation determined by the chosen $w_0 = 8.5 \mu\text{m}$ and $\lambda = 800 \text{ nm}$ is considered for simulation.

2.1.2 Results of test particle simulations and discussion

Since the dephasing length varies as a function of electron energy, QPM of DLA can be optimized by using variable modulation structures and electron densities in the plasma waveguide. We illustrate this by using electron densities $n_{e,L}=2.5 \times 10^{18} \text{ cm}^{-3}$ and $n_{e,H}=1.25 \times 10^{19} \text{ cm}^{-3}$ for low- and high-density regions of the waveguide, respectively. Figure 2.2(a) shows the dependence of the electron energy gain ΔT on axial position z in waveguides with constant density modulation periods, determined from dephasing lengths shown in Fig. 2.1(a). QPM with a constant density modulation can only be achieved for electrons having higher initial kinetic energies. Aperiodic density modulation is needed when lower energy electrons are injected in the waveguide and can be effective, as illustrated in Fig. 2.2(b). The optimal modulation period increases with the increase in electron energy and converges to L_c at higher electron energies. Each section length $L_{d,n}$ is chosen to be the average of its initial dephasing length $L_{c,i}$, obtained for the initial electron kinetic energy $T_{0,i}$ of that section, and the final dephasing length $L_{c,f}$, obtained by the approximated final kinetic energy $T_{0,f}$ after acceleration by $L_{c,i}$. The chirp rate of the axial modulation period of the plasma waveguide used in the simulations presented in Fig. 2.2(b) are summarized in Table 2.1.

For DLA in a plasma waveguide with the length L_{wg} , electron energy gain is

$$\Delta T \simeq C_e C_{qpm} C_{env} q_e E_{z,max} L_{wg}, \quad (2.4)$$

TABLE 2.1: Assigned lengths, $L_{d,L}$ and $L_{d,H}$ (in μm), for low- and high-density regions in each section of the plasma waveguide for DLA of electrons with initial energies $T_0 = 5$ MeV and 15 MeV shown in Fig. 2.2(b).

T_0		Index of the modulation period							
		1	2	3	4	5	6	7	8
5 MeV	$L_{d,L}$	100	120	150	180	210	220	230	240
	$L_{d,H}$	70	70	70	80	80	90	90	90
15 MeV	$L_{d,L}$	210	220	240	240	240	240	240	240
	$L_{d,H}$	80	80	90	90	90	90	90	90

where several correction factors are included in the estimation of energy gain and can be calculated. The first correction factor (C_e) takes into account the axial field change over one dephasing length:

$$C_e = \int_0^\pi \sin(\phi) d\phi / \pi = 0.637. \quad (2.5)$$

The second correction factor (C_{qpm}) takes into account the alternating acceleration and deceleration of electrons in the QPM process:

$$C_{qpm} = \frac{L_{d,L} - L_{d,H}}{L_{d,L} + L_{d,H}}, \quad (2.6)$$

where the electron is accelerated over a length $L_{d,L}$ of the low-density region and decelerated over a length $L_{d,H}$ of the high-density region. The third correction is associated with the difference between the electron velocity and laser group velocity, resulting in electrons sampling the field at various points of the laser pulse envelope. For an electron with a velocity v_e co-propagating with a Gaussian laser pulse with a pulse length L_p , the axial effective envelope width L_{en} the electron experience along the propagation direction z is related to the laser pulse length L_p by

$$L_{en} = \frac{v_e}{v_e - v_{g,avg}} L_p, \quad (2.7)$$

where $v_{g,avg}$ is the laser group velocity averaged over distance z . In a density-modulated plasma waveguide composed of high-density regions of length $L_{d,H}$ and low-density regions of length $L_{d,L}$, $v_{g,avg}$ is

$$v_{g,avg} = \frac{L_{d,L}v_{g,L} + L_{d,H}v_{g,H}}{L_{d,L} + L_{d,H}}, \quad (2.8)$$

where $v_{g,L}$ and $v_{g,H}$ are the laser pulse group velocities in high- and low-density regions, respectively. As a result, the average amplitude of the field envelope, as the final

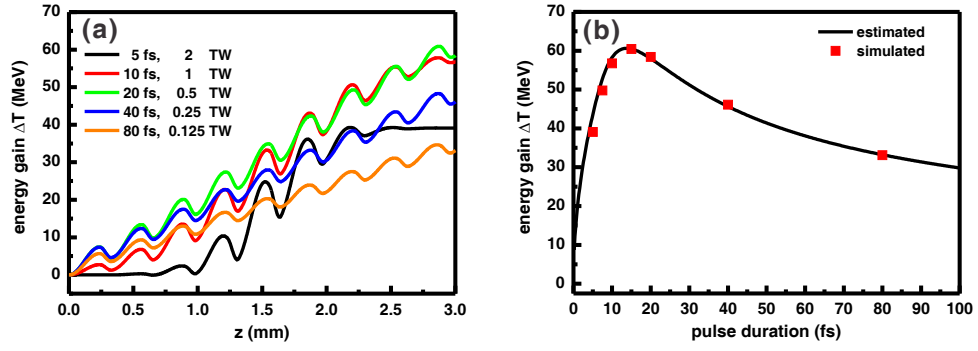


FIGURE 2.3: (a) Dependence of the electron energy gain ΔT on propagation distance z in plasma waveguides for electrons of $T_0 = 40$ MeV with laser pulse durations $\tau_p = 5$ fs, 10 fs, 20 fs, 40 fs, and 80 fs. The other parameters are the same in Fig. 2.2. (b) Comparison of estimated DLA electron energy gain ΔT from Eq. 2.4 to the results obtained by the test particle simulation.

correction factor, can be defined as

$$C_{\text{env}} = \frac{2}{L_{wg}} \int_0^{L_{wg}/2} \exp[-2 \ln 2 (z/L_{en})^2] dz. \quad (2.9)$$

For example, consider an electron with initial kinetic energy $T_0 = 40$ MeV ($v_e \simeq c$), plasma waveguide length $L_{wg} = 3$ mm, modulation lengths $L_{d,L} = 240$ μm and $L_{d,H} = 90$ μm for low- and high-density regions, respectively, with $n_{e,L} = 2.5 \times 10^{18}$ cm^{-3} and $n_{e,H} = 1.25 \times 10^{19}$ cm^{-3} , and a 0.5-TW laser pulse with length $L_p = 6$ μm ($\tau_p \simeq 20$ fs) and mode radius $w_0 = 8.5$ μm . These parameters result in $v_{g,avg} = 0.9976 c$, $L_{en} \approx 2.5$ mm, $C_{\text{env}} = 0.856$, $C_{qpm} \simeq 0.455$, and lead to energy gain of $\Delta T = 57.4$ MeV.

Several drive laser pulse durations are used to verify the effect of laser pulse duration on the estimated energy gain calculated by Eq. (2.4), and the results are shown in Fig. 2.3. In the case of an ultrashort laser pulse (≤ 10 fs), the peak power and field amplitude are increased, but the temporal walk-off effect limits the acceleration at the initial and terminating sides of the waveguide, eventually resulting in energy gain reduction. Increasing the laser pulse duration (≥ 20 fs) can reduce the walk-off effect; however, the decreased field amplitude and finite acceleration distance (L_{wg}) reduce the final energy gain as a result. Figure 2.3(b) shows the calculated energy gain ΔT from Eq. (2.4) as a function of laser pulse duration τ_p , with identical parameters as in Fig. 2.3(a), along with the results obtained by test particle model. The comparison of the results in Fig. 2.3(b) indicates that the simulation matches well with the results predicted by Eq. (2.4), which can be used as an empirical relation for calculating the energy gain in DLA.

In Refs. [4, 5], the energy gain from QPM of DLA can also be estimated by

$$\frac{\Delta T'}{m_e c^2} \simeq 4\delta a_0 \left(\frac{L_p}{w_0}\right) \left(\frac{\lambda_p}{\lambda}\right)^2 \left(1 + \frac{2\lambda_p^2}{\pi^2 w_0^2}\right)^{-2}, \quad (2.10)$$

where δ is the relative amplitude of the density modulation, $a_0 = q_e E_{r,max}/m_e \omega c$ is the normalized vector potential of the laser pulse and the plasma wavelength is $\lambda_p = 2c\pi/\omega_p$, with $\omega_p^2 = \langle \omega_{p0}(z)^2 \rangle_z$ representing the averaged axial plasma frequency over the propagation distance z . Energy gain estimated by Eqs. (2.4) and (2.10) can be compared by using the case with pulse duration $\tau_p=5$ fs and laser power $P_0=2$ TW shown in Fig. 2.3, in which the temporal walk-off effect is significant. With $a_0=0.55$ (2-TW laser peak power), $L_p=1.5$ μm (5-fs laser pulse duration) and the remaining identical parameters, Eq. (2.4) estimates a significantly larger energy gain of $\Delta T \simeq 42.1$ MeV than $\Delta T' \simeq 13.5$ MeV by using Eq. (2.10). This large difference results from the simplified dependence of energy gain $\Delta T' \propto L_p$ in Eq. (2.10), since the energy gain from the front and back of the pulse is not negligible. In addition, the calculated average laser pulse group velocities is $v'_g \simeq 0.9973c$ for Eq. (2.10), while $v_{g,ave} \simeq 0.9976c$ is obtained by Eq. (2.8) for Eq. (2.4). As a result, the pulse length dephasing time $t' \sim L_p/(c - v'_g)$ for Eq. (2.10) is about 50% shorter than that in Eq. (2.4), such that $\Delta T'$ is further reduced due to the greater temporal walk-off mismatch. Since the estimate of energy gain ΔT by Eq. (2.4) considers the variation of an Gaussian temporal pulse envelope, it is particularly useful when DLA with ultrashort laser pulses is considered. In contrast, the estimate of energy gain by $\Delta T'$ of Eq. (2.10) is more appropriate when a plasma waveguide with a sinusoidal density modulation [4, 5] is used, because of the definition $\omega_p^2 = \langle \omega_{p0}(z)^2 \rangle_z$. When DLA is performed with a 20-fs, 0.5-TW laser pulse as shown in Fig. 2.3, the energy gains $\Delta T \simeq 57.4$ MeV via Eq. (2.4) and $\Delta T' \simeq 50.1$ MeV via Eq. (2.10) are in reasonable agreement, representing a case when the temporal walk-off between the laser pulse and the electron becomes less effective due to the longer pulse length.

With optimally designed plasma structures, the axial acceleration phase region for QPM DLA can be investigated by injecting test electrons with various initial axial positions z_0 and phases ϕ_0 along the central axis. Figure 2.4(a) shows the final electron energy gain as a function of initial phase for various initial electron kinetic energies. When the electron are injected with higher energies, the acceleration phase region is broader. The finite laser mode size also limits the size of the radial acceleration region; as a result, electrons at greater radial positions cannot be accelerated as efficiently as the on-axis electrons. To investigate the features of the radial acceleration region, test electrons are assigned various initial radial positions. Figure 2.4(b) shows the final electron energy gain as a function of the initial radial position for several initial kinetic

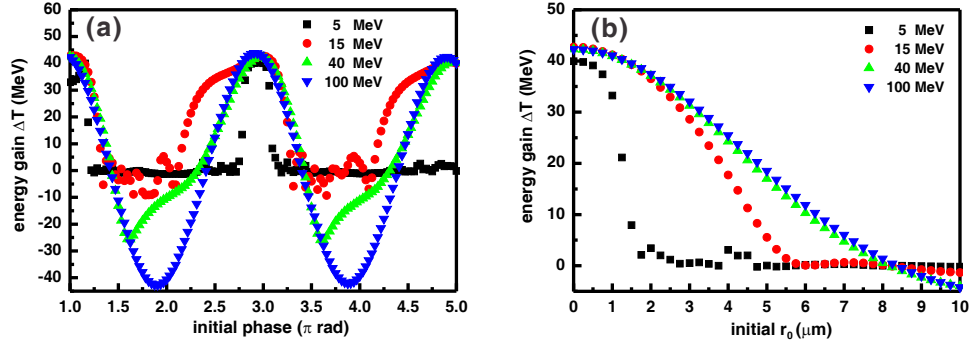


FIGURE 2.4: (a) Final electron energy gain ΔT as a function of electron initial phase ϕ_0 for electrons of $T_0=5$ MeV, 15 MeV, 40 MeV and 100 MeV. (b) Final electron energy gain ΔT as a function of electron initial radial position r_0 for electrons of $T_0=5$ MeV, 15 MeV, 40 MeV, and 100 MeV and 2-mm long plasma waveguide. The other parameters are the same as in Fig. 2.2.

energies. The results indicate that the radial acceleration region is narrower for lower initial electron energies.

2.1.3 Conclusion from test particle simulations

In summary, the test particle model that has been developed can therefore be used to provide an accurate estimate of the DLA energy gain. A positively chirped density modulation of the waveguide structure is required, especially for DLA with low electron kinetic energies ($\lesssim 20$ MeV). For such low injected electron energies, DLA dephasing length changes rapidly with the increased electron energy. Therefore, the plasma structure should be varied accordingly, so that electrons can remain in the acceleration phase over the propagation distance. The difference between the electron velocity and the laser group velocity leads to the temporal walk-off effect, which expands the laser pulse envelope to an equivalent acceleration field envelope with a dimension comparable to that of the plasma waveguide. For DLA driven by an ultrashort laser pulse, the electrons can overtake the laser pulse, so that the effective acceleration distance is limited. When a long laser pulse is used such that the width of effective acceleration envelope becomes larger than the length of the plasma waveguide, the acceleration distance is then limited by the waveguide length even though the walk-effect is reduced. A analytical formula is proposed to estimate the final energy gain, and it considers the correction factors for the average of field change over a dephasing length, the efficiency of QPM process, and the average amplitude of the acceleration field envelope.

The DLA energy gain also depends on the injected initial axial (related to the initial phase) and radial position of electrons. Only electrons having proper initial phases can continuously stay in the acceleration phase of QPM process to accumulate significant

final energy gain. The finite laser mode size limits the radial acceleration region such that off-axis electrons cannot be accelerated consistently with the QPM condition. A wider tolerance on the injection phase and radial distance from the waveguide axis exists for electrons injected with a higher initial energy.

2.2 PIC simulations of DLA

In DLA realized in density-modulated plasma waveguides, the electron beam interacts with the electromagnetic field of a co-propagating laser pulse, but also with the electrostatic field originating from the plasma. This electrostatic field has not been considered in the test particle model. To improve the fidelity of the DLA simulation, a PIC simulation is developed and used for more detail study of DLA. In addition to the electromagnetic field of the laser pulse, the closed-loop solutions for the total electric field in the PIC model include the electric field variation originating from the plasma density perturbation driven by the bunch charge and the laser ponderomotive force, which has not been considered in the test particle model. Therefore, PIC simulations offer a significantly improved understanding of the injected bunch electron dynamics during the DLA process. In addition to being driven directly by the laser field, the electrons also experience the laser ponderomotive force and the electrostatic force from the excited plasma waves. The results lead to improved understanding of the interactions between the electron bunch, the laser pulse, and the background plasma. Simulations have been conducted to study the scheme in which seed electron bunches with moderate energies are injected into a plasma waveguide and the DLA is performed by use of relatively low-power (0.5-2 TW) laser pulses. Selected bunch injection delays with respect to the laser pulse, bunch lengths, and bunch transverse sizes have been studied in a series of simulations. The energy spectrum and emittance of the accelerated electron bunch vary depending on those initial conditions, which can be chosen to optimize the DLA performance.

2.2.1 Development of the PIC model

The PIC model has been developed using the framework of the commercial software package VORPAL [6], in which a 3-D Cartesian coordinate system is defined and the laser pulse propagates along one of the coordinate system axes. In the PIC model a 3-D Cartesian coordinate system (x, y, z) is defined and the laser pulse propagates along the axial direction x . The size of the simulation box is $L_x = 23.38 \mu\text{m}$ in the axial x direction and $L_y \times L_z = 60 \mu\text{m} \times 60 \mu\text{m}$ in the transverse directions y and z . Each simulation has been performed in a moving frame co-propagating with the laser pulse at a speed of light in vacuum c . In all simulations, the transverse y - and z -cell sizes are fixed at $D_y = D_z = 400 \text{ nm}$ and $D_x = 12.5 \text{ nm}$ for the x -cell size. The time step is chosen as

$dt = 4.16 \times 10^{-2}$ fs for satisfying the Courant condition. The decomposition of the radial unit vector \hat{r} in cylindrical coordinates via $\hat{r} = \cos \phi \hat{y} + \sin \phi \hat{z} = y/(y^2 + z^2)^{1/2} \hat{y} + z/(y^2 + z^2)^{1/2} \hat{z}$ is applied to transform the radially polarized electric field, discussed in Ref. [3], in the transverse \hat{y} and \hat{z} Cartesian coordinate components. Consequently, the y and z components constituting the radially polarized field can be defined as

$$E_\alpha(x, y, z, t) = E_0 \theta_0 \frac{\alpha}{(y^2 + z^2)^{1/2}} \text{env}(x, y, z) \text{env}(t) \cos(\psi + 2\psi_G), \quad (2.11)$$

where $\alpha = y, z$ for the radial field components E_y and E_z , respectively. The function $\text{env}(x, y, z)$ defines the spatial envelope of the radial field as

$$\text{env}(x, y, z) = \left[\frac{(y^2 + z^2)^{1/2}}{w_0} \right] \left(\frac{w_0}{w(x)} \right)^2 \exp \left[-\frac{y^2 + z^2}{w(x)^2} \right], \quad (2.12)$$

with the laser beam size

$$w(x) = w_0 \sqrt{1 + \frac{(x - x_f)^2}{z_r^2}}, \quad (2.13)$$

which is characterized by the focused mode radius w_0 , Rayleigh length $z_r = \pi w_0^2 / \lambda$ and the focal position x_f . The $\text{env}(t)$ represents the temporal Gaussian envelope of the laser field as

$$\text{env}(t) = \exp \left[-2 \ln 2 \frac{(t - t_0)^2}{\tau_p^2} \right], \quad (2.14)$$

defined with a full-width at half-maximum (FWHM) Gaussian pulse duration τ_p and a delay time t_0 . The optical phase includes the following contributions:

$$\psi = \psi_0 + \omega t - k(x - x_f) - \frac{k(y^2 + z^2)}{2R}, \quad (2.15)$$

in which $R = (x - x_f) + z_r^2 / (x - x_f)$, ψ_0 is the an absolute phase and $\psi_G = \tan^{-1}(x - x_f) / z_r$ is commonly referred to as the Gouy phase of a Gaussian beam. As the transverse fields E_y and E_z are defined at the boundary and lunched into the simulation space, the axial field E_x and the magnetic field associated with the laser pulse are subsequently calculated via the finite-difference time domain (FDTD) method. For a laser pulse with $\lambda = 800$ nm that is focused into a FWHM diameter of $w_D = 15$ μm ($w_0 = w_D / \sqrt{2 \ln 2} \simeq 12.74$ μm) with a duration $\tau_p = 20$ fs and a peak power of $P_0 = 0.5$ TW, $E_0 \simeq 86$ TV/m gives the maximum radial amplitude $E_{y,\max} = E_0 \theta_0 \simeq 737.5$ GV/m and $E_{x,\max} = E_0 \theta_0^2 \simeq 34.4$ GV/m. Figures 2.5(a) and (b) show the snapshots of the longitudinal E_x and transverse E_y components of the electric field of a 20-fs, 0.5-TW, 800-nm radially polarized laser pulse with a diameter $w_D = 15$ μm in the simulation space. Unless specifically mentioned, those laser pulse parameters are used in the remainder of the simulations.

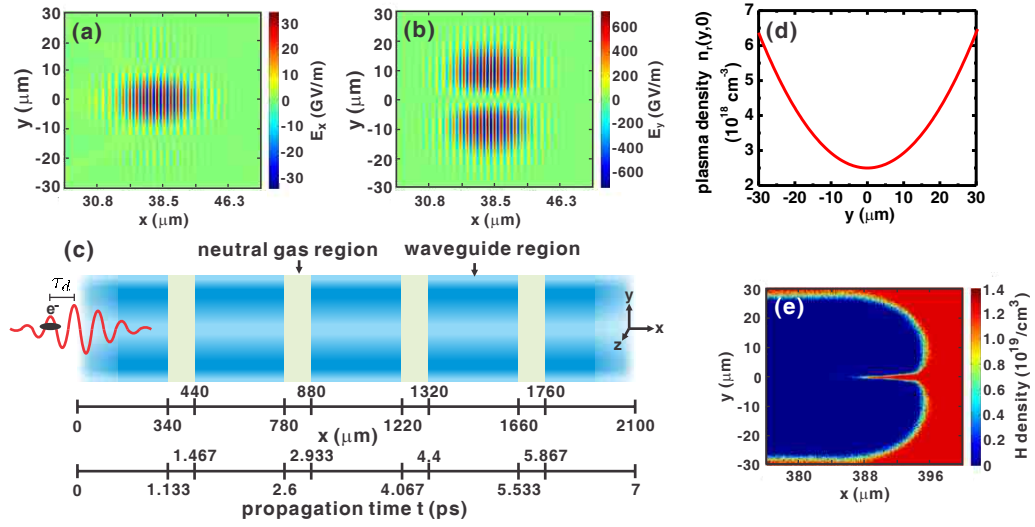


FIGURE 2.5: Snapshots of (a) axial E_x and (b) transverse E_y electric fields of a 20-fs, 0.5-TW, radially polarized laser pulse with a diameter $w_D = 15 \mu\text{m}$; (c) illustration of a density-modulated plasma waveguide, along with the axial position x and the bunch propagation time t ; (d) transverse plasma density profile $n_r(y, 0)$ defined for the waveguide regions; (e) ionization of neutral hydrogen gas by the electric field illustrated in (a) and (b).

For this model, hydrogen has been considered to be the gas target for irradiation by the spatially modulated ignitor and spatially uniform heater pulses to produce the density-modulated plasma waveguide, as illustrated in Fig. 2.5(c). The simulation starts at the moment when the hydrodynamic expansion of the plasma forms a proper radial plasma density profile for guiding an injected laser pulse in the longitudinal direction. The density profile $n_r(y, z)$ of a perfect plasma waveguide that guides a laser pulse in a mode radius w_0 is defined by a parabolic function:[1]

$$n_r(y, z) = n_{p0} + \Delta n \frac{(y^2 + z^2)}{w_0^2}, \quad (2.16)$$

where n_{p0} is the on-axis density, $\Delta n = 1/r_e \pi w_0^2$, and r_e is the classical electron radius. Figure 2.5(d) shows the transverse profile assigned to the waveguide at the beginning of the simulation, with a laser-guided diameter of $w_D = 15 \mu\text{m}$ (or $w_0 = 12.74 \mu\text{m}$) with $n_{p0} = 2.5 \times 10^{18} \text{ cm}^{-3}$, while $\Delta n = 6.975 \times 10^{17} \text{ cm}^{-3}$. In each waveguide section, hydrogen ions and electrons are both defined by the same plasma density function $n_p(x, y, z)$. Next, a neutral gas region of length $\lambda_{H,1}$ is defined with a uniformly distributed hydrogen atom density $n_a(x, y, z) = n_{a0} = 1.25 \times 10^{19} \text{ cm}^{-3}$. Hydrogen atoms can be ionized within a few optical cycles and the majority of the pulse experiences a uniformly distributed plasma rather than becoming defocused by ionization-induced refraction. As shown in Fig. 2.5(e), hydrogen atoms can be fully ionized by the front foot of a 20-fs, 0.5-TW laser pulse, which causes the sharp decrease of hydrogen density

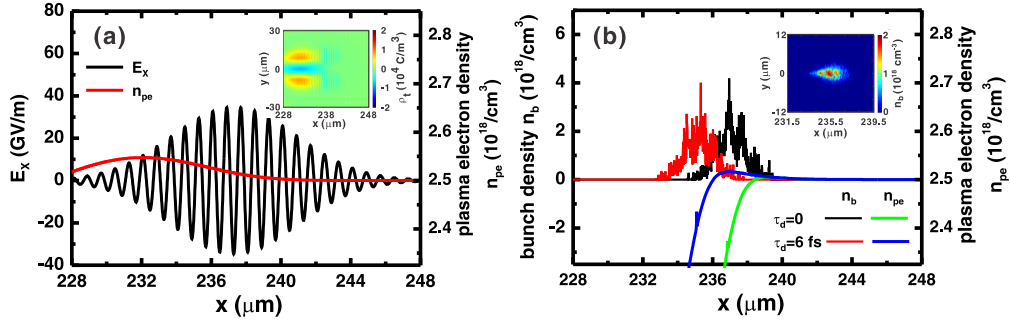


FIGURE 2.6: (a) On-axis axial field E_x and the plasma electron density n_{pe} with laser power $P = 0.5$ TW. (b) Comparison of the plasma electron density n_{pe} and on-axis bunch density n_b when 6-fs bunches, with $\tau_d = 6.2$ fs and 0, are injected, with other conditions corresponding to (a). Insets in (a) and (b) show the corresponding 2-D total charge ρ_t and bunch density distributions.

in the region $x \sim 386 - 395$ μm.

A 6-fs, 40-MeV bi-Gaussian (having transverse and longitudinal Gaussian shapes) electron bunch with a diameter $w_b = 3$ μm, bunch charge of $q_b = 5$ pC, and the peak density $n_{b0} = 1.6 \times 10^{18}$ cm $^{-3}$ are chosen as the default bunch parameters for the simulation. Those parameters are typical for laser wakefield accelerated electrons. The initial energy spectrum for bunch electrons exhibits an energy spread of 4 MeV with an average energy $T_0 = 40$ MeV. The default RMS normalized emittance in y -dimension is calculated to be $\epsilon_{N,y} \simeq 1\pi$ mm-mrad by the definition: [7]

$$\epsilon_{N,y} = \frac{4}{m_e c} \sqrt{\langle y^2 \rangle \langle P_y^2 \rangle - \langle y P_y \rangle^2} \pi \text{ mm} - \text{mrad}, \quad (2.17)$$

utilizing the particle positions y and momenta P_y . Absorbing boundaries for the laser field and all of the particle species are defined around the simulation box. Particles of the injected electron bunch that reach the boundaries are considered to have left the region-of-interest (ROI) of the simulation and are not included in the value of bunch emittance. The ROI of the simulation is equivalent to placing a collimator at the waveguide output in an experiment.

2.2.2 Results of the PIC simulations and discussion

2.2.2.1 Effect of the electron bunch injection delay

The effect of electron bunch injection delay has been parametrically studied first, defined as the time delay between the peak of laser pulse envelope and the peak of the electron bunch density distribution. The laser pulse and the electron bunch shape the plasma electron distribution, which in turn produces an electrostatic force that changes the bunch properties. Figure 2.6(a) illustrates the variation of the on-axis

plasma electron density $n_{pe}(x)$ when a 20-fs, 0.5-TW laser pulse with a beam size $w_D = 15 \text{ } \mu\text{m}$ propagates in the first waveguide section illustrated in Fig. 2.5(c). The resulting peak value of the perturbed plasma electron density $n_1(x) = n_{pe}(x) - n_{p0}$ is $n_{1p} \sim 4.6 \times 10^{16} \text{ cm}^{-3}$ (or $n_{1p}/n_0 \sim 1.8\%$), which produces a radial electrostatic force approximated by $F_s \sim w_b q_e^2 n_1 / 2\epsilon_0 \sim 10^9 \text{ N}$. As a result, the electron bunch diverges where the plasma electron density is increased, especially when it is injected near the tailing edge of the laser pulse. Under the same laser and waveguide conditions used in Fig. 2.6(a), Fig. 2.6(b) shows the variation of $n_{pe}(x)$ when electron bunches with $\tau_d = 6.2 \text{ fs}$ and $\tau_d = 0$ are injected. The bunch expels the electrons and an ion channel is gradually formed following the front edge of the bunch [8]. At this moment, the ion focusing force at both injection delays increases the peak density of the bunch to $n_{b0} \sim 3 \times 10^{18} \text{ cm}^{-3}$, thus fulfilling the condition for creating an underdense plasma lens. With $\tau_d = 6.2 \text{ fs}$, the bunch density distribution shown in the inset of Fig. 2.6(b) has evolved into a “trumpet” shape that contains an expanding *head* region and a *pinch* region (with a reducing radius), which are typical for an electron bunch propagating in the ion-focusing-regime. [9] However, as shown in Fig. 2.6(b), the bunch head experiences a higher on-axis plasma electron density (prepared by the laser pulse) when it is injected with a greater delay τ_d . In this situation, the head erosion of the bunch is amplified by the electrostatic force of the concentrated plasma electrons in addition to the inherent erosion due to a finite emittance. [10] The electron energy gain varies with the injection delay τ_d because of the walk-off effect between the laser pulse and the electron bunch. Equation 2.9 can be redefined as

$$C_{\text{env}} = \frac{1}{L_{wg}} \int_{x_{\text{int}}}^{x_{\text{fin}}} \exp \left[-2 \ln 2 \left(\frac{x}{L_{en}} \right)^2 \right] dx, \quad (2.18)$$

in which the initial electron position x_{ini} with respect to the effective field envelope is determined by the variable injection delay τ'_d :

$$x_{\text{ini}} = -\tau'_d c \frac{v_e}{v_e - v_{g,avg}}, \quad (2.19)$$

and the final electron position is $x_{\text{fin}} = x_{\text{ini}} + L_{wg}$. As a result, the maximum energy of the accelerated electrons is reduced when the bunch is injected with a smaller delay τ'_d .

We next considered the bunch characteristics following DLA with a delay $\tau_d = 6.2 \text{ fs}$. The spatial particle distribution (within $|z| \leq 0.4 \text{ } \mu\text{m}$), $\theta_y - y$ trace space, energy spectrum, and θ_y distribution for the bunch electrons are shown in Fig. 2.7. Figure 2.7(a) illustrates the effect of the electron injection phase on the acceleration or deceleration process, resulting the gradual broadening of the energy spectrum, shown in Fig. 2.7(c). The radial Lorentz force $F_r \propto q_e E_r$ also focuses or defocuses the bunch electrons according to their injection phases with respect to the radial field E_r . However,

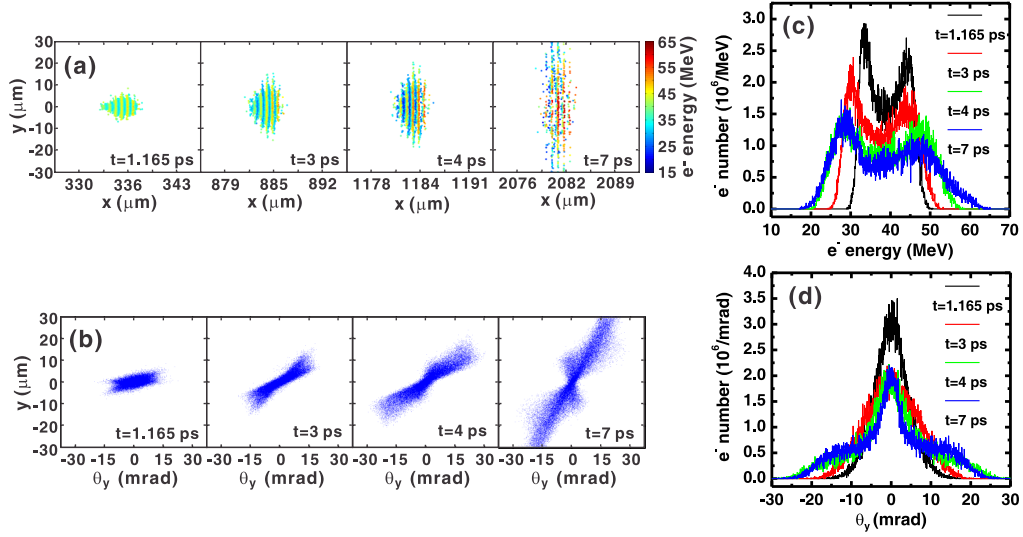


FIGURE 2.7: Variation of the (a) electron distribution ($|z| \leq 0.4 \mu\text{m}$), (b) trace space, (c) energy spectrum, and (d) θ_y distribution for an bunch injected with $\tau_d = 6.2$ fs, $T_0 = 40$ MeV, $\tau_b = 6$ fs, and propagates in a 2.1-mm long plasma waveguide.

the radial electrostatic force resulting from the concentrated on-axis plasma electrons shown in Fig. 2.6(b) acts to increase the divergence of the electron bunch along the entire propagation distance in the waveguide. The bunch electrons stay within the radial position $r \leq 9 \mu\text{m}$ (the peak of the radial field when $w_D = 15 \mu\text{m}$), experiencing focusing from the laser ponderomotive force. The confinement effect becomes prominent at a distance $x \sim 1200 \mu\text{m}$ (or at the propagation time $t = 4$ ps) when the electron bunch is synchronized with the laser pulse. Consequently, bunch electrons within $r \leq 9 \mu\text{m}$ are better collimated. As shown in the θ_y - y trace space in Fig. 2.7(b), particles in the vicinity of the on-axis region ($y = 0$) exhibit smaller values of θ_y , especially when $t = 7$ ps. This property can also be observed from the θ_y distribution shown in Fig. 2.7 (d), in which the collimation effect provided by the laser ponderomotive force is evident. However, the bunch still has an overall tendency to diverge, and its emittance $\epsilon_{N,y}$ increases from 1π -mm-mrad at the point of injection to approximately 14π -mm-mrad at the output ($x = 2.1$ mm), as shown in Fig. 2.8.

Reducing the injection delay τ_d helps to mitigate the bunch divergence. As shown in Fig. 2.6(a), the perturbed on-axis plasma density $n_1(x)$ is reduced near the leading edge of the laser pulse. Electron bunches injected with a smaller τ_d experience a reduced defocusing force from the perturbed background plasma. The ponderomotive force of the laser also peaks at $\tau_d = 0$; therefore, the confinement force increases with a smaller injection delay. To improve the emittance and collimation after DLA, selected injection delays $\tau_d = 3.2$ fs, 0, and -3 fs are assigned to the bunches, with the remaining bunch parameters the same as in the previous analysis. As shown in Fig. 2.8(a), the final emittance $\epsilon_{N,y}$ and the amplitude of its temporal oscillation are reduced at smaller

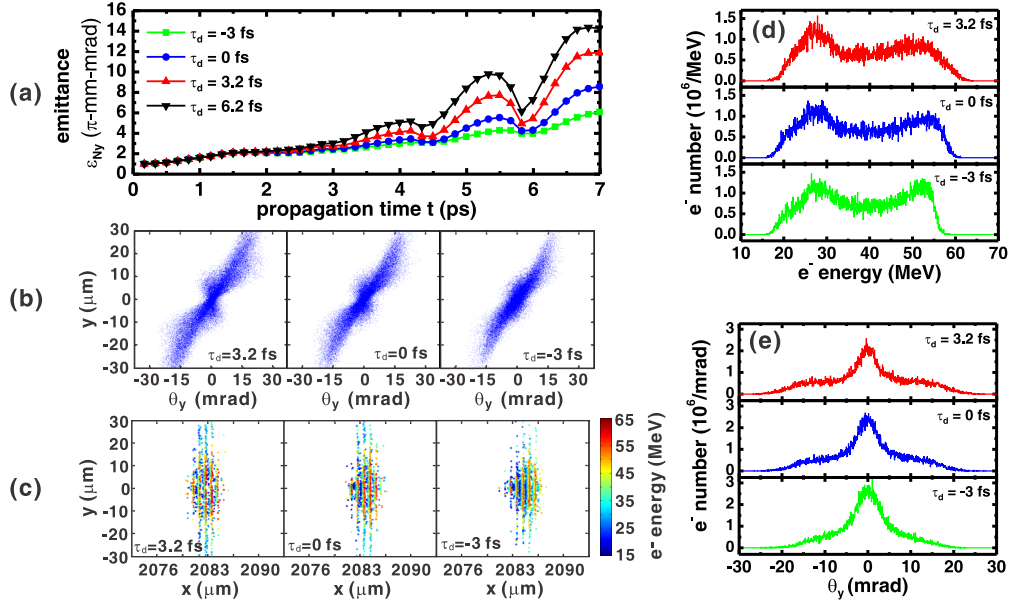


FIGURE 2.8: (a) Bunch emittance $\epsilon_{N,y}$ as a function of the propagation time t for different time delays $\tau_d = 6.2$ fs, 3.2 fs, 0, and -3 fs. Comparison for the final (b) trace space distributions, (c) electron distributions, (d) energy spectra, and (e) θ_y distributions for bunches injected with $\tau_d = 3.2$ fs, 0, and -3 fs.

injection delays τ_d . Because of the walk-off effect, the electron bunch overtakes the laser pulse and experiences the decreasing radial field at the leading edge of laser pulse as it approaches the waveguide output. With a smaller τ_d , the effective radial Lorentz force F_r experienced by the electrons is further decreased, which explains the reduced oscillation of $\epsilon_{N,y}$. This condition corresponds to the final θ_y - y trace space distributions shown in Fig. 2.8(b), in which particles lying around $y = \pm 10 \mu\text{m}$ are less scattered when τ_d is smaller. The improved collimation of the bunch at a smaller delay τ_d can also be observed from the comparison of the particle distributions in Fig. 2.8(c) and the θ_y distribution in Fig. 2.8(e) at three different injection delays. As more electrons remain in the region where the laser field is intense, the fraction of electrons accelerated to higher energies is increased. The comparison of electron energy spectra shown in Fig. 2.8(d) indicates an increased electron number in the range 50 – 60 MeV with a reduced τ_d that is attributed to the reduced bunch divergence.

2.2.2.2 Effect of the electron bunch length

Results described in the previous section indicate a trend of increasing divergence in DLA of short electron bunches. With a fixed injection delay $\tau_d = 0$ and bunch charge of $q_b = 5$ pC, Fig. 2.9(a) shows the comparison of on-axis plasma density $n_{pe}(x)$ when bunch duration is set to $\tau_b = 6$ fs, 13 fs and 20 fs, while the rest of the bunch and laser parameters are kept the same as in the previous analysis. Regardless of the bunch duration τ_b , the reduction of the plasma electron density $n_{pe}(x)$ is always initiated at the

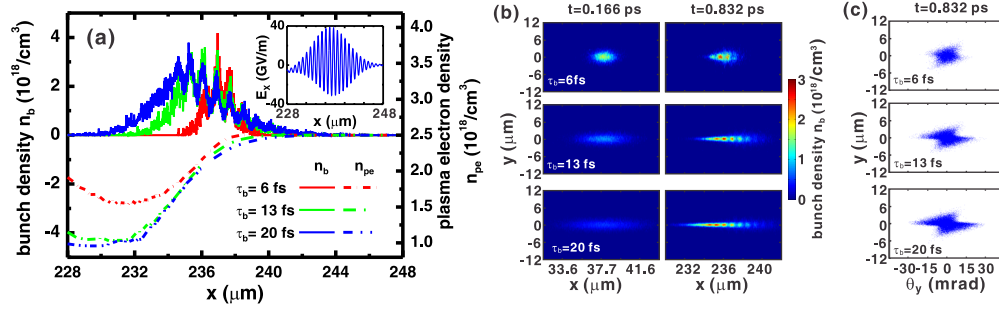


FIGURE 2.9: (a) Comparison of the on-axis bunch density n_b and plasma electron density n_{pe} at $t = 0.832$ ps for bunches injected at $\tau_d = 0$ with durations $\tau_b = 6$ fs, 13 fs and 20 fs. The corresponding (b) variations of the 2-D bunch density from $t = 0.166$ ps to $t = 0.832$ ps and (c) the trace space distributions at $t = 0.832$ ps. Inset in (a) shows the corresponding on-axis axial field E_x with the bunch of $\tau_b = 20$ fs.

leading edge of the bunch. For a 6-fs electron bunch having a length $L_b = \tau_b c = 1.8 \mu\text{m}$, the majority of bunch electrons do not experience a strong focusing force from the created ion channel since the variation of $n_{pe}(x)$ is of order $\lambda_p/4 = \pi c/2\omega_{p0} \simeq 5.3 \mu\text{m}$ for its falling edge. Therefore, for increased durations of the electron bunch of $\tau_b = 13$ fs and 20 fs, the corresponding bunch lengths $L_b = 3.9 \mu\text{m}$ and $6 \mu\text{m}$ are closer to the value of $\lambda_p/4$, such that more bunch electrons can be confined in the created ion channel. Consequently, the collimation and emittance of the DLA-accelerated bunch can be improved. The ion-focusing effect also rapidly increases the density of the injected bunch when $\tau_b = 13$ fs and 20 fs, as shown in Fig. 2.9(b). The increased density for bunches with $\tau_b = 13$ fs and 20 fs also enhances the ion-focusing force, which can be understood from the further reduced $n_{pe}(x)$ in Fig. 2.9(a). Comparing the trace space results in Fig. 2.9(c), larger θ_y values are characteristic for the electrons with a larger τ_b , since they experience an increased ion-focusing force in the trailing edge of the bunch.

Comparing Figs. 2.8(a) with 2.10(a), the emittance $\epsilon_{N,y}$ can be considerably reduced by increasing the bunch duration to $\tau_b = 13$ fs and 20 fs with the same delay time $\tau_d = 0$. The bunch electrons can be more concentrated at the waveguide center, as shown in Fig. 2.10(b) at those longer bunch durations, which is attributed to the enhanced ion-focusing effect. Examining the trace spaces at $t = 5.5$ ps and $t = 5.83$ ps, the range of θ_y is increased when the bunch propagates in the high-density regions, where the ion focusing force is enhanced by a higher plasma density n_p . Many of the bunch electrons are collimated in the next low-density region, as evidenced by the reduced range of θ_y between $t = 5.83$ ps and $t = 7$ ps, shown in Fig. 2.10(b). The final bunch particle distributions for $\tau_b = 13$ fs and 20 fs in Fig. 2.10(c) show that more electrons at the leading and trailing edges cannot be effectively accelerated/decelerated when the bunch duration becomes comparable to the laser pulse duration of $\tau_p = 20$ fs. Therefore, the final energy spectra in Fig. 2.10(d) become more uniform with increased bunch duration

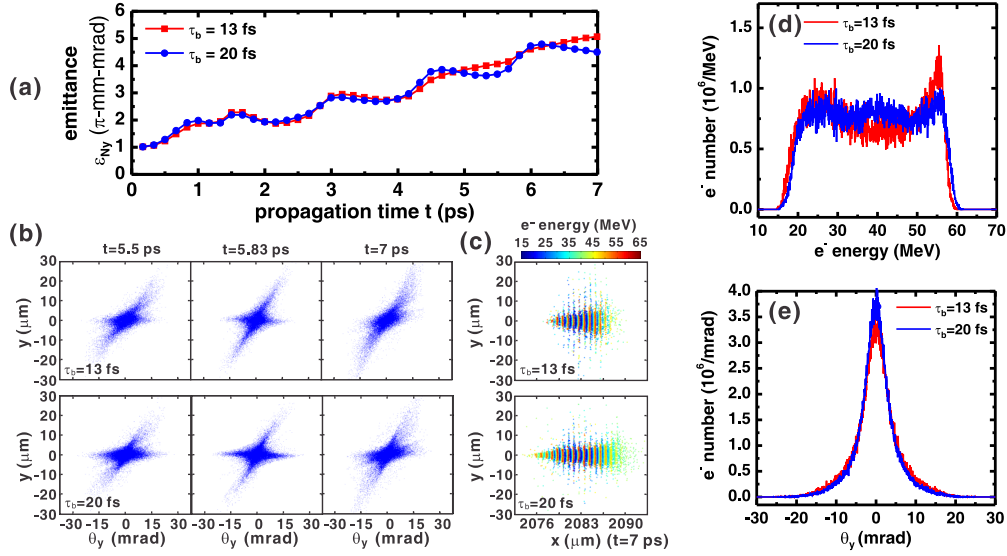


FIGURE 2.10: (a) Bunch emittance $\epsilon_{N,y}$ as a function of propagation time t for bunches with durations $\tau_b = 13$ fs and 20 fs. (b) Sampled trace space distributions and final (c) electron distributions, (d) energy spectra and (e) θ_y distributions.

τ_b .

The formation of density peaks becomes prominent when a long bunch is injected [8]. Since most of the bunch electrons can be confined in the ion channel over a long distance, a sufficient time exists during the DLA process for this density modulation to be realized. In a moving coordinate of the simulation box $\zeta = x - ct$, Fig. 2.11(a) shows the evolution of the bunch density throughout its propagation in the 2.1-mm long waveguide. In the early phase of propagation, the density modulation results from the focusing and defocusing of the bunch by the radial Lorentz force F_r . The on-axis bunch density n_b in the central axial region and the electron momenta (P_x and P_y) at $t = 0.83$ ps are shown in Fig. 2.11(b). This radial force induces a periodic change of the electron transverse momentum P_y , and the bunch density n_b peaks at the phases where electrons are focused (the corresponding regions with $P_y > 0$ are shown in red and with $P_y < 0$ are shown in blue). As the electrons are continuously accelerated/decelerated in the DLA process, the increased axial velocity difference between the electrons then gradually starts to dominate. From Fig. 2.11(c), at $t = 5.83$ ps the bunching happens at the regions where the acceleration phase (red) switches to the retarding phase (blue) with a period of 800 nm, equal to the laser wavelength. The peak density of the microbunches can be approximately one order of magnitude higher than the original peak density $n_{b0} = 4.8 \times 10^{17} \text{ cm}^{-3}$. The density of the microbunches continues to change as they propagate. At $t = 6.83$ ps, the densities of the microbunches drop, mainly driven by the defocusing of electrons by the radial Lorentz force F_r . Therefore, the density modulation in DLA is a highly nonlinear process that results from the combined effect of the radial

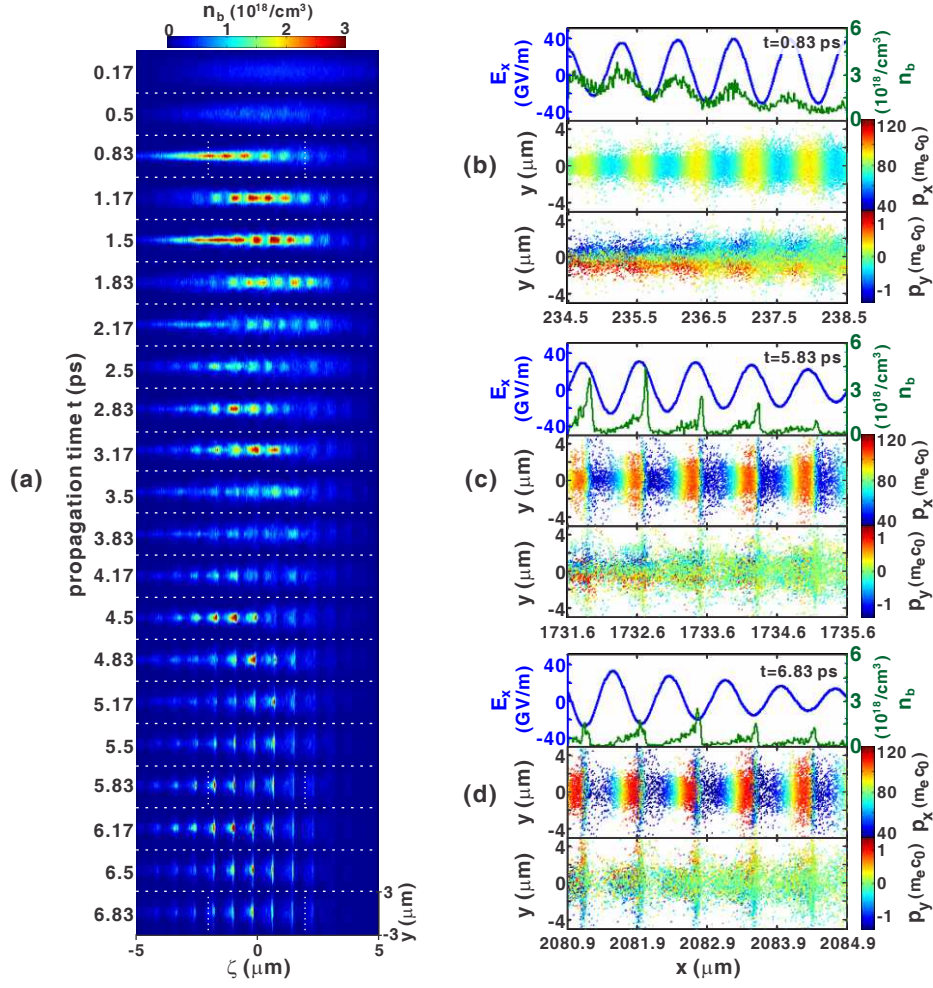


FIGURE 2.11: (a) Sampled 2-D bunch density variation in the entire propagation for a 20-fs injected bunch. The corresponding on-axis axial field E_x , bunch density n_b , axial P_x and transverse P_y momentum distributions at (b) $t = 0.83$ ps, (c) $t = 5.83$ ps, and (d) $t = 6.83$ ps

force and the axial momentum modulation on the bunch. Comparing Figs. 2.11(b) with (c), it can be observed that the bunch density peaks in the phases offset by π with respect to the axial electron momentum (P_x) modulation. Therefore, the phase of the P_x modulation can be used as a signature that identifies the dominant bunching mechanism in DLA.

2.2.2.3 Effect of the transverse electron bunch size

Effect of the transverse electron bunch size is discussed next. The finite diameter of the laser beam limits the size of the effective radial region and the efficiency of DLA because of the reduced axial field available to the off-axis electrons. [4, 5] On the other hand, the density modulation is enhanced as the off-axis electrons experience a stronger radial focusing/defocusing Lorentz force $F_r \propto q_e E_r$. For large bunch transverse size, the

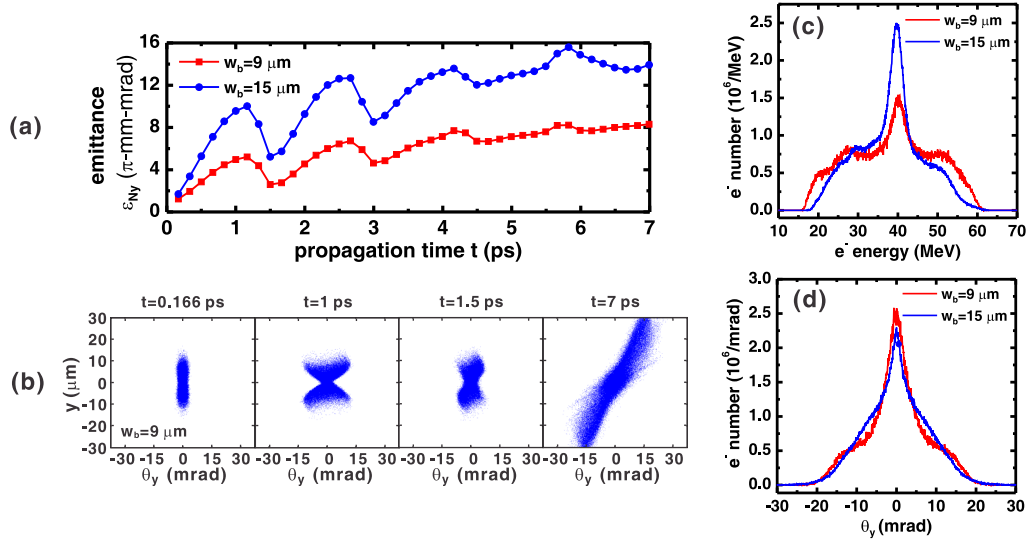


FIGURE 2.12: (a) Bunch emittance $\epsilon_{N,y}$ as a function of propagation time t for bunches with sizes $w_b = 9\text{ }\mu\text{m}$ and $15\text{ }\mu\text{m}$. (b) Sampled trace space distributions for $w_b = 9\text{ }\mu\text{m}$. Final (c) energy spectra and (d) θ_y distributions for $w_b = 9\text{ }\mu\text{m}$ and $15\text{ }\mu\text{m}$.

variation of emittance $\epsilon_{N,y}$ is directly related to the effect of focusing and defocusing of the bunch by the radial force F_r . Figure 2.12(a) shows the change of emittance $\epsilon_{N,y}$ when bunches of $w_b = 9\text{ }\mu\text{m}$ and $15\text{ }\mu\text{m}$ are injected. The emittance $\epsilon_{N,y}$ changes periodically and tends to increase as the bunch propagates through the waveguide. The periodic focusing and defocusing of many of the electrons by the radial force accounts for the rapid change of $\epsilon_{N,y}$ before $t = 3.5\text{ ps}$. When $w_b = 9\text{ }\mu\text{m}$, the trace spaces between $t = 0.166\text{ ps}$ and 1.5 ps in Fig. 2.12(b) become symmetrically distributed with respect to the two axes. The increasing magnitude of $|P_y|$ of those electrons, while being accelerated/decelerated by the radial force, leads to a broadened θ_y distribution at $t = 1\text{ ps}$. When the bunch propagates into the next high-density region, the reversal of the radial force F_r , due to the change of E_r pointing, decreases $|P_y|$ and the populated range of θ_y . When $w_b = 15\text{ }\mu\text{m}$, the enhanced effect of the radial force F_r leads to the further increased $\epsilon_{N,y}$ along the propagation. The DLA efficiency is reduced, as shown by the final energy spectra in Fig. 2.12(c), with $w_b = 9\text{ }\mu\text{m}$ and $15\text{ }\mu\text{m}$, where a large fraction of the bunch electrons still have energies around 40 MeV. Increased bunch sizes also lead to greater divergence angles $\Delta\theta_y$, as shown in the final θ_y distributions in Fig. 2.12(d). The results show that increasing the injected bunch transverse size negatively impacts DLA performance. However, the formation of microbunches can be enhanced by choosing a larger bunch diameter, whereby the electrons experience a greater radial force that drives the density modulations.

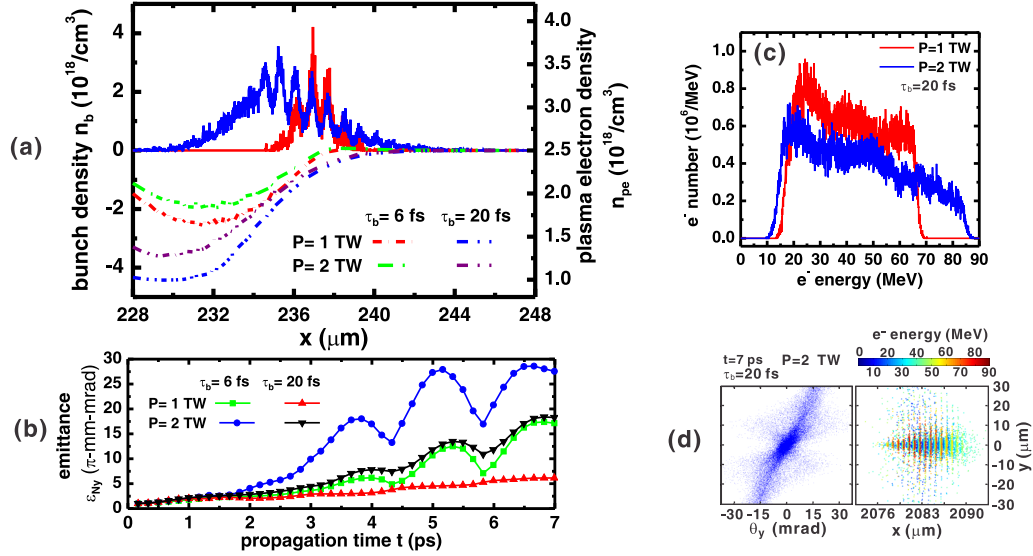


FIGURE 2.13: Effect of the laser power ($P = 1$ TW and 2 TW). (a) Comparison of the on-axis bunch density n_b and plasma electron density n_{pe} at $t = 0.832$ ps for bunches injected at $\tau_d = 0$ with durations $\tau_b = 6$ fs and 20 fs. (b) The emittance $\epsilon_{N,y}$ as a function of propagation time t . (c) Final energy spectra for bunch with $\tau_b = 20$ fs. (d) The final trace space and electron distributions for bunch with $\tau_b = 20$ fs with laser power $P = 2$ TW. The waveguide length $L_{wg} = 2.1$ mm is fixed for all cases.

2.2.2.4 Effect of the laser power and waveguide length

The maximum energy gain scales as $\Delta T_{max} \propto q_e E_{x,max} L_{wg}$ for DLA in a plasma waveguide. By increasing the laser power $P \propto E_{x,max}^2$ or the waveguide length L_{wg} , a higher energy gain can be achieved through DLA. To understand how the bunch properties change with the laser power, two laser pulse powers ($P = 1$ TW and 2 TW) are used to accelerate the electron bunches with two different durations ($\tau_b = 6$ fs and 20 fs), injected with a fixed delay $\tau_d = 0$ into waveguides with length $L_{wg} = 2.1$ mm. Figure 2.13(a) indicates the plasma density perturbation $n_1(x)$ can be inhibited by increased the laser pulse power, since a stronger laser ponderomotive force overcomes the electrostatic force from the bunch that acts to expel the plasma. The ion focusing force acting on the electrons is lowered accordingly. The increased radial field at higher laser power also leads to a greater defocusing of a fraction of the bunch electrons. As a result, the emittance $\epsilon_{N,y}$ increases with increased laser power, as shown in Fig. 2.13(b). Figure 2.13(c) shows the final energy spectra of the 20-fs bunches when laser powers of $P = 1$ TW and 2 TW are used. Compared to the results shown in Fig. 2.10(d) with $P = 0.5$ TW, the maximum energy gain is doubled ($\Delta T_{max} = 45$ MeV) by setting $P = 2$ TW. However, the strong radial field at $P = 2$ TW produces a greater radial force F_r , which significantly defocuses a fraction of the bunch electrons, as illustrated in the final trace space and electron distributions shown Fig. 2.13(d). This leads to a relatively large final emittance $\epsilon_{N,y} \simeq 18.3\pi\text{-mm-mrad}$. The results indicate that,

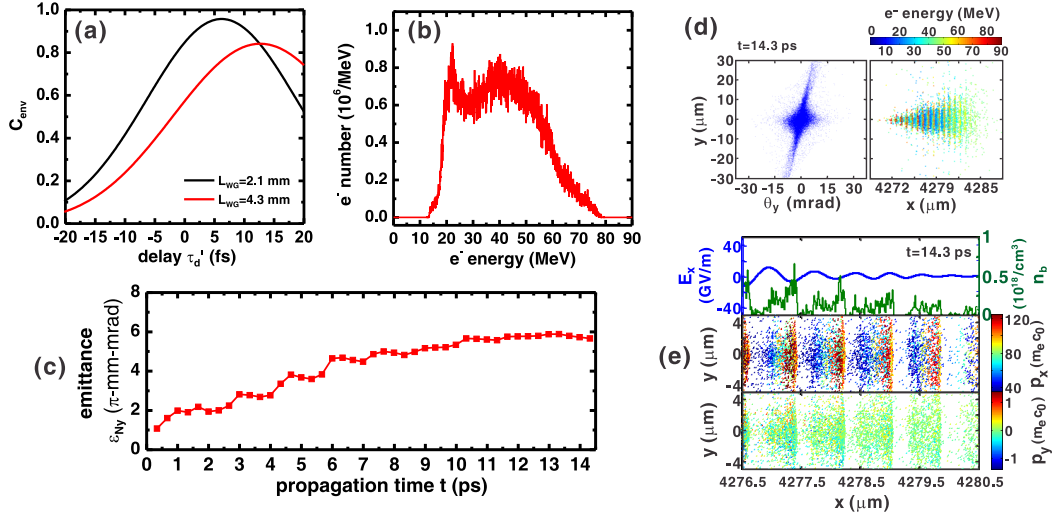


FIGURE 2.14: (a) Dependence of C_{env} on the variable injection delay τ'_d for waveguide length $L_{wg} = 2.1$ mm and 4.3 mm. (b) Final energy spectrum for the bunch of $\tau_b = 20$ fs injected at $\tau_d = 0$, with waveguide of $L_{wg} = 4.3$ mm and laser power of $P = 0.5$ TW. (c) The corresponding emittance $\epsilon_{N,y}$ change with time t . Final (d) trace space and electron distributions and (e) on-axis bunch density n_b and electron momentum distributions.

although the maximum DLA energy gain can be increased by using a laser pulse with higher peak power, the transverse properties of the bunch can be degraded due to the inhibited ion-focusing effect and the increased radial force that causes a greater bunch divergence.

A higher maximum energy gain ΔT_{max} can still be obtained by extending the waveguide length L_{wg} . This is studied by increasing the number of density modulation periods in the structure illustrated in Fig. 2.5(c), so that a plasma waveguide of $L_{wg} = 4.3$ mm is applied. Figure 2.14(a) shows the dependence of C_{env} (Eq. 2.18) on the injection delay τ'_d , with $L_{wg} = 2.1$ mm and 4.3 mm. If the bunches are injected with $\tau_b = 20$ fs and $\tau_d = 0$, the majority of electrons ranging from $\tau'_d = -10$ fs to 10 fs have a lowered C_{env} when $L_{wg} = 4.3$ mm. In addition, only the trailing electrons with $\tau'_d \sim 8 - 17$ fs can have a relatively high $C_{\text{env}} > 0.8$. As a result, a rapidly decreasing number of electrons up to the maximum gain $\Delta T_{\text{max}} \simeq 40$ MeV is present in the final energy spectrum shown in Fig. 2.14(b) when using $P = 0.5$ TW and $L_{wg} = 4.3$ mm. For comparison, a small final bunch emittance $\epsilon_{N,y} \simeq 5.7\pi$ -mm-mrad is obtained, as shown in Fig. 2.14(c), while $\epsilon_{N,y} \simeq 18.3\pi$ -mm-mrad in Fig. 2.13(b) when $P = 2$ TW and $L_{wg} = 2.1$ mm. The final trace space and electron distributions in Fig. 2.14(d) show that the ion channel can still confine most of the bunch electrons as they approach the waveguide output, which also helps to maintain a relatively small final bunch emittance $\epsilon_{N,y}$.

2.2.3 Conclusion from DLA PIC simulations

To summarize the overall results, self-consistent solutions for the interactions among the laser pulse, injected electrons, and the background plasma have been obtained, significantly improving the fidelity of the DLA simulations. When the bunch length is short compared to $\lambda_p/4$ in the low-density region, the choice of the injection delay τ_d is important for control of the final transverse properties of the bunch. When the injection delay is large, a significant divergence of the electron bunch results from the electrostatic force provided by the concentrated electrons of the background plasma and the defocusing force exerted by the radial field. The collimation of the bunch can be improved by using a smaller injection delay, in which case a stronger ponderomotive force provided by the laser pulse helps to confine the electrons. However, the maximum energy gain is reduced when a smaller injection delay is used. When the bunch length becomes closer to $\lambda_p/4$, the ion-focusing effect is enhanced and the final collimation of the bunch can be considerably improved. In this situation, a density modulation of the bunch driven by the radial Lorentz force and the axial momentum modulation can be observed. In the case when the bunch is injected with a large bunch transverse size, comparable to the laser beam diameter, the reduced axial field experienced by the off-axis electrons lowers the acceleration efficiency. On the other hand, the focusing and defocusing of the bunch is enhanced by the stronger radial forces, which contribute to micro-bunch formation. The peak density of the microbunches can be approximately 10-fold higher than the peak density of the bunch injected into the waveguide. From those combined results, it can be concluded that the injection of an electron bunch with a long bunch length (close to $\lambda_p/4$, referring to the low-density plasma region) and a small transverse size with respect to the laser pulse diameter is preferred for maintaining the favorable bunch transverse properties in DLA in a plasma waveguide. Under those conditions, the ion-focusing force can effectively collimate the bunch, so that a small emittance can be obtained following the DLA process.

The maximum energy gain can be increased by increasing the laser power or extending the waveguide length. In the case when a higher power laser pulse is used, the inhibited ion-channel formation and the stronger radial Lorentz force degrade the bunch collimation. The radial force can defocus a large fraction of the electrons in the bunch, even when a relatively long bunch is injected. If the waveguide length is extended to increase the maximum energy gain, the temporal walk-off between the laser pulse and the electron bunch limits the efficiency, such that only the tailing electrons in the bunch can be effectively accelerated to higher energies. From those results we conclude that the optimal DLA requires the use of a moderate laser power to help maintain good transverse properties of the bunch. When the waveguide length is increased, the laser pulse duration must also be increased to mitigate the walk-off effect. However, such longer

pulses also requires a greater pulse energy to maintain a high acceleration gradient.

Chapter 3

Fabrication of density-modulated plasma channels

An important challenge for effective DLA is realizing the guided propagation of a radially polarized laser pulse in a density-modulated plasma waveguide. To conduct the Tasks 2, 3 and 6 of this project, an all-optical method, based on the ignitor-heater scheme for plasma waveguide fabrication, was designed and experimentally implemented to fabricate the density-modulated plasma waveguides. Density-modulated plasma waveguides can also be realized by placing a ring grating before an axicon, such that an axially modulated line focus is produced that drives the waveguide formation [11]. Another technique has been developed by others, in which wire obstructions are used on the gas nozzle so that a modulated atom density exists in the target region. A density-modulated plasma waveguide can be fabricated with this preformed atom variation in a straightforward fashion [12]. Among the techniques for making density-modulated plasma waveguides, the laser machining method used in this work is the most versatile: changing the axial structure of the plasma waveguide is easily achieved by using different mask patterns [2]. The intensity modulation can also be applied on the heater pulse as a variation of the laser machining method to fabricate programmably structured plasma waveguides [13]. Figure 3.1 shows the conceptual design of the system for the fabrication of density-modulated plasma waveguides. The ignitor is horizontally imaged and vertically focused by a cylindrical lens pair onto a neutral gas target. The vertical focusing produces a line focus of the ignitor pulse in which the intensity is sufficiently high for optical field ionization (OFI) of the gas atoms to take place. The on-target longitudinal pattern of the ignitor is determined by the mask. Therefore, different axial structures of the plasma waveguide can be created by varying the mask pattern. The heater pulse is made to propagate orthogonally with respect to the ignitor through the target. According to the results by Volfbeyn *et al.* [14], this 90° geometry limits the transverse extent of the initial heat deposition volume to the small intersection of the two pulses.

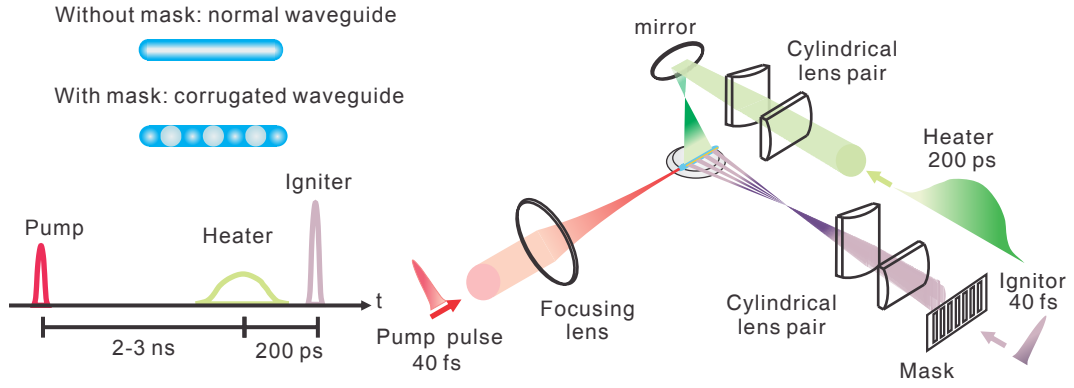


FIGURE 3.1: System design for fabrication of density-modulated plasma channels.

As a result, a cylindrically symmetric plasma waveguide can be created, which will be more appropriate for guiding a radially polarized laser pulse. The experimental set-up for DLA experiments is introduced in Sec. 3.1. Experimental results obtained when fabricating plasma channels in Ar are discussed in Sec. 3.2.

Finally, in Sec. 3.3, we discuss the micrometer-scale supersonic gas jets, designed via the principles of isentropic compressible fluid flow to support DLA experiments. The gas jet design uses the a de Laval valve concept and the principles of isentropic compressible fluid flow to accelerate a gas from a static reservoir into a vacuum chamber at supersonic velocities. The gas jet design was tested using COMSOL Multiphysics high Mach number flow simulation program. Nozzles were manufactured in titanium and aluminum and the surface quality of the nozzles was evaluated by X-ray computed tomography.

3.1 Experimental setup for fabrication of plasma channels

We upgraded our laser facility with an additional multi-pass amplifier in order to generate high-energy laser pulses needed to investigate the laser shaping technique for plasma channels. Figure 3.2(a) shows the related equipment: the Nd:YAG laser (Spectra-Physics, model Pro-250), the multi-pass chirped-pulse amplifier (Amplitude Technologies Centaurus) and the grating-pair compressor. Pumped at 810 mJ by the Nd:YAG laser, the amplifier produced the output pulse at 300-mJ at 795 nm, with near-200-ps pulse duration from the 4-mJ seed pulse. To realize the laser machining technique based on the ignitor-heater scheme, 80-mJ of the output energy is split for the ignitor and the rest of energy will be used for the heater for waveguide production. The ignitor beam is firstly expanded to the size of approximately 3 cm (clear aperture) and then directed to the grating-pair pulse compressor. Figures 3.2(b) and (c) show the output beam profile and spectrum measured after the compressor, for which the pulse can be compressed to 38 fs. Separate energy tuners for the ignitor and heater beams

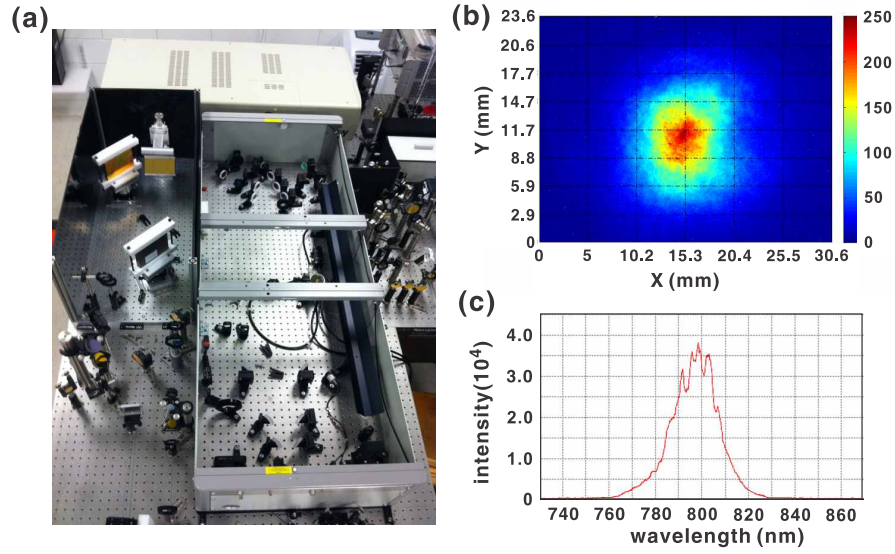


FIGURE 3.2: (a) High-energy laser: Nd:YAG pump laser (top), the multi-pass CPA amplifier (right) and the grating-pair compressor (left). The output (b) intensity profile and (c) spectrum of the laser pulse from the compressor

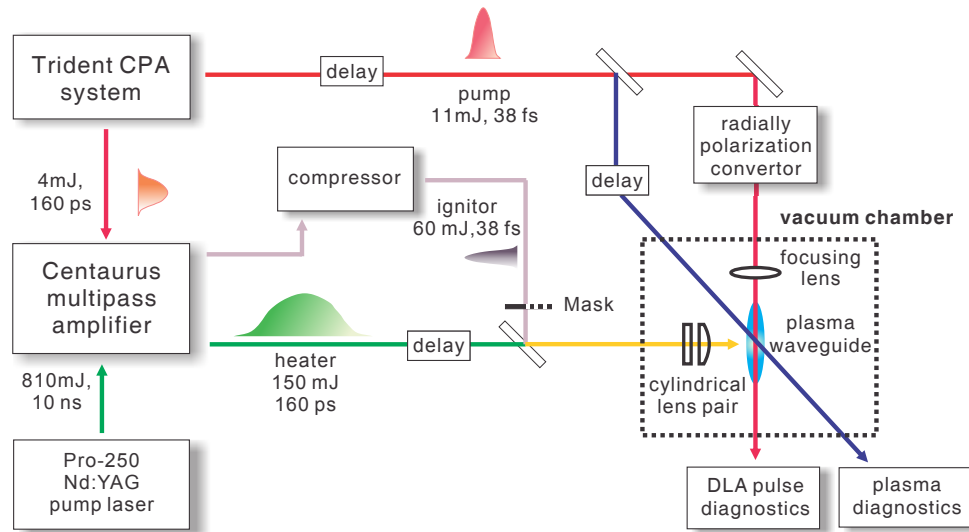


FIGURE 3.3: Layout of the experimental system for DLA

are prepared as well, which will help to fine tune beam energies when optimizing the plasma waveguide structure in experiments.

Figure 3.3 shows the complete system layout for the experiments with the laser system introduced above. The pulse energy of 80 mJ is split from the output of the Centaurus laser amplifier and compressed for use as the ignitor pulse. Considering the damage threshold ($<0.1 \text{ J/cm}^2$) of the compressor gratings, an energy tuner limits the maximum energy of 60 mJ for the ignitor when a 3-cm clear aperture size is used. After

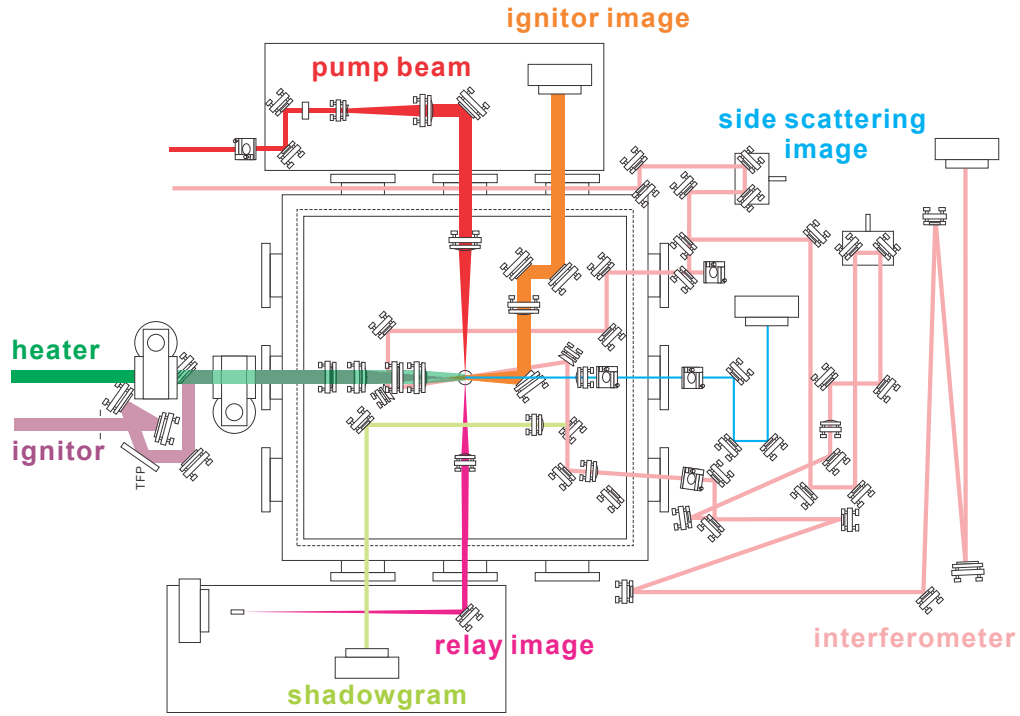


FIGURE 3.4: Detailed experimental layout for the fabrication of plasma waveguides using the laser machining technique

compression the ignitor pulse is directed to pass through a mask before propagating into the vacuum chamber. The heater beam is also expanded to a 3-cm clear aperture size, with a pulse duration ~ 160 ps and a maximum energy of approximately 150 mJ, controlled by a separate energy tuner. The arrival time to the gas target for the pump pulse, ignitor, and heater can be varied by controlling the corresponding delay lines. The time separation among those three pulses has to be optimized to create the optimal plasma guiding condition for the pump pulse. A vacuum chamber with a size of $30'' \times 30'' \times 16.2''$ and related vacuum, gas, signal control and CCD systems for running experiments have been constructed. The vacuum chamber can be pumped down to $\sim 10^{-4}$ torr in 30 mins and finally reaches the pressure of 3.3×10^{-5} torr after pumping for 5 hours. Diagnostics for the plasma waveguide have been set up surrounding the experimental chamber.

Figure 3.4 shows the detail of the experimental layout designed for experiments with plasma waveguides. A gas nozzle is placed at the center of the chamber, producing supersonic gas flow as the target for the laser shaping of plasma waveguide. The pump pulse is converted into the radially polarization state and then directed to pass through the waveguide produced in the gas target. Propagating perpendicularly to the pump pulse, the ignitor is horizontally imaged with a demagnification factor of 5–10 of the mask pattern (depending on the variable distance between the imaging lens and the gas target) and vertically focused by a cylindrical lens pair onto the neutral gas target.

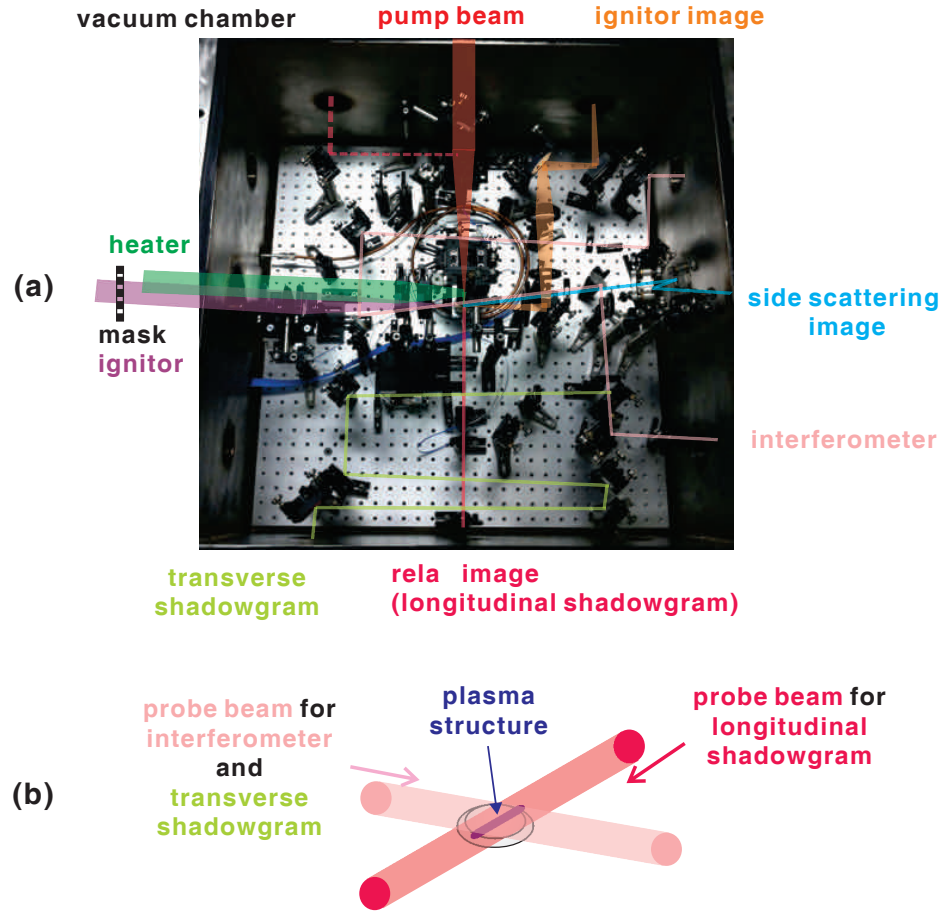


FIGURE 3.5: (a) Experimental setup in the vacuum chamber: gas jet (at center), pump beam line (red), ignitor beam line (purple) and image system (orange), heater beam line (green), side scattering image (blue), interferometer probe beam (pink, the relay image/longitudinal shadowgram (fuchsia) and the transverse shadowgram (light green). (b) Illustration for the propagation of probe beams of the longitudinal and transverse shadowgrams when diagnosing a plasma structure above the gas nozzle.

Using a spatially varying intensity pattern that is sufficiently intense to ionize the gas, plasma with relatively low electron densities are produced where the laser intensity is sufficiently high. The gas target is subsequently irradiated by another 160-ps, 160-mJ heater pulse which propagates orthogonally with respect to the ignitor. The heater is focused and imaged to a line-focus to overlap the plasma produced by the ignitor for further heating and ionizing of the plasma through the inverse bremsstrahlung (IB) heating mechanism. The increased temperature near the beam axis induces hydrodynamic expansion of the plasma starting from the center of the plasma column, lowering the on-axis electron density and forming a proper density profile to guide pump laser pulses in the longitudinal direction a few ns later. The heater pulse energy and the time delay between the heater pulse and the radially polarized pump pulse need to be optimized to realize the guiding condition. The axial plasma structure can be controlled by the mask pattern for the ignitor. The imaging system for ignitor is designed to monitor the

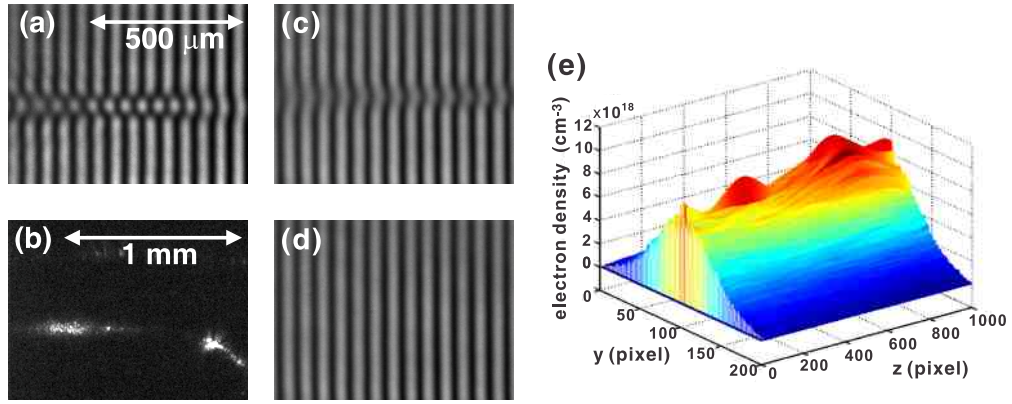


FIGURE 3.6: Experimentally obtained (a) interferogram and (b) side scattering image of a N plasma column produced by a laser pulse with the peak intensity $4.8 \times 10^{16} \text{ W/cm}^2$ at a 700 psi backing pressure of the N gas to the gas valve. Interferograms (c) with a N plasma column with 100 psi backing pressure and (d) without plasma in the target space; (e) retrieved plasma density distribution from (c) and (d).

on-target intensity pattern for laser pulse shaping. The shaped axial-structure of plasma waveguide can be diagnosed by the side scattering image system, the transverse shadowgraphic image system, and the interferometer. In addition, the guiding effect of the laser pulse in the plasma waveguide can be measured by the relay image system, setting the image plane at the exit of the plasma waveguide. Figure 3.5(a) shows the practical state of the DLA experimental station. In experiments, a probe beam propagating along the longitudinal direction of the plasma structure can be used to diagnose the transverse distribution of plasma by recording the longitudinal shadowgram depicted in Fig. 3.5. This longitudinal shadowgraphic image can be obtained by bypassing the pump beam to the focusing lens and then imaging the beam intensity distribution at the end of the gas jet via the relay imaging lens. Figure 3.5(b) illustrates the propagation directions of the two probe beams with respect to the created plasma structure when they are used to take the transverse and longitudinal shadowgraphic images above the gas nozzle.

The side scattering and the interferometry have been employed in previous experiments [2, 11, 12, 13] as powerful *in-situ* diagnostics techniques for characterizing the density-modulated structure of fabricated plasma waveguides. Figure 3.6 illustrates the proof-of-principle results for measuring plasma columns that are created by passing 2.3-mJ, 40-fs linearly polarized laser pulses with 10-μm focal spot diameter through a N gas target. A gas pulse valve with a 1.4-mm conical nozzle is used to produce the N gas target for experiments. With a 700-psi backing pressure to the gas valve, Fig. 3.6(a) and (b) shows the side scattering image and the corresponding interferogram of a ionized N plasma for comparison. In this case, the peak intensity of the laser pulse was estimated to be $4.8 \times 10^{16} \text{ W/cm}^2$, sufficiently intense to ionize N atoms to the fifth ionization state by the tunneling ionization mechanism. The recorded interferograms can be used

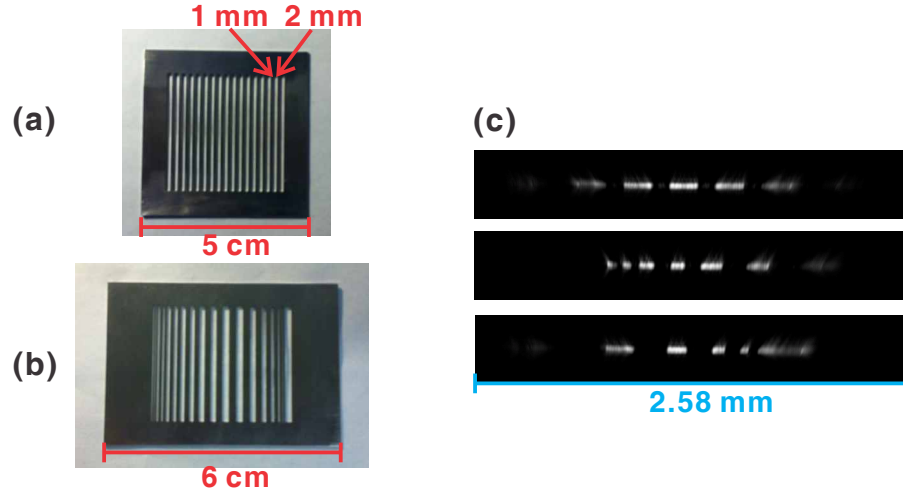


FIGURE 3.7: Stainless steel mask is used to create the ignitor intensity modulation with a (a) constant and (b) chirped period. (c) On-target ignitor intensity patterns with various mask pattern.

to retrieve the plasma density distribution by use of numerical methods. The Abel transformation method is utilized to estimate the 2-D plasma density profile with cylindrical symmetry, with an example provided in Fig. 3.6(c)–(e). The interferogram taken with a generated plasma column by 100 psi backing pressure is shown in Fig. 3.6(c), while Fig. 3.6(d) represents the null test (without plasma). Two sets of data are processed using a numerical algorithm to calculate the spatial phase shift and the spatial electron density distribution, as shown in Fig. 3.6(e). From those results, it is estimated that the on-target peak electron density is approximately 10^{19} electrons/cm³ at 100 psi backing pressure. The interferometer and the analysis of electron plasma density allows us to monitor the structure of the created plasma waveguide. In those tests, the magnification factor is set to approximately 3 for the side scattering image of the laser light and the shadowgram of the plasma to observe the plasma distribution in the entire gas target region. The interferogram is used to observe the detailed plasma distribution in the plasma waveguide structure with a larger magnification factor of 8.

The image system for the ignitor has been designed to monitor the on-target intensity pattern, and its image plane is carefully aligned on top of the gas nozzle center. Figure 3.7(a) shows an example stainless steel mask having the duty-on width of 2-mm and the duty-off width of 1-mm, with a constant modulation period. With a demagnification of 10 by the imaging lens, the corresponding on-target ignitor intensity pattern, measured by the ignitor beam image system, is shown in the upper part of Fig. 3.7(c) for a 7-mJ ignitor pulse. By using a mask with chirped duty period, as shown in Fig. 3.7(b), ignitor intensity patterns with an increasing and a decreasing modulation periods can be obtained, as shown in the middle and lower section of Fig. 3.7(c), respectively. In experiments, the ignitor beam energy can be increased to a maximum of 60 mJ, which

produces sufficiently high intensity to ionize the gas target and produce seed electrons in the specified spatial regions.

3.2 Experimental results in production of plasma channels

3.2.1 Fabrication of argon plasma channels

Based on the ignitor-heater scheme, a demonstration of optical fabrication of plasma channels was performed with Ar gas target. Compared to He and N, Ar exhibits a lower optical ionization threshold and a larger cross section for the collisional IB heating mechanism. Both of those characteristics help to obtain high-density plasma ($>10^{18} \text{ cm}^{-3}$) and effectively drive its hydrodynamic expansion with the laser pulse energies provided by the used laser system. In the experiments, the Ar gas jet was produced by a 1.6-mm long slit nozzle, in which a 1.2-mm flat-top density profile can be obtained. The ignitor beam was focused to a line of ~ 6 -mm full length in the target plane with a vertical width of 20 μm FWHM. The heater beam was focused into a line of ~ 9 -mm full length on the target. The lengths of ignitor and heater line foci are chosen to be longer than the gas jet length, so that more uniformly distributed laser intensities of the two beams in the target space can be obtained. It was experimentally observed that the stability of the produced plasma density profiles can be improved when longer full lengths of the ignitor and heater were applied. Increasing the density of the gas also helped to improve the stability of plasma density profiles; therefore, the Ar backing pressure of 750 psi was selected to be fed into the gas valve for all experiments.

With 3.7-mJ ignitor and 36-mJ heater, Fig. 3.8(a) shows the measured transverse and longitudinal shadowgrams of an Ar plasma channel, while the fringe shifts in the corresponding interferogram reveal the plasma distribution across the central region. The ignitor-heater separation is 100 ps and the probe delay of 1.5 ns after the ignitor was used to record the shadowgrams and interferograms. The transverse and longitudinal shadowgrams have spatial resolutions of 1.23 $\mu\text{m}/\text{pixel}$ and 0.91 $\mu\text{m}/\text{pixel}$, respectively, while the interferogram was measured with a resolution of 0.59 $\mu\text{m}/\text{pixel}$. Unless specifically mentioned, the scales of the shadowgram and interferogram images shown in Fig. 3.8(a) and the above delays between the ignitor, heater and probe pulses are used in the remainder of the measured results described in this chapter. Figure 3.8(b) indicates that a weakly ionized plasma, with a density below the sensitivity of the interferogram ($<10^{18} \text{ cm}^{-3}$), was produced when only the ignitor was introduced into the target space. The 36-mJ heater was not able to measurably ionize the Ar gas, as shown in Fig. 3.8(c).

With a fixed ignitor energy of 3.7 mJ, effect of varying the heater energy between 22.8–58.5 mJ on Ar plasma channel production are shown in Fig. 3.9(a). It can be observed that the enhanced heating and ionization process via the IB mechanism increased

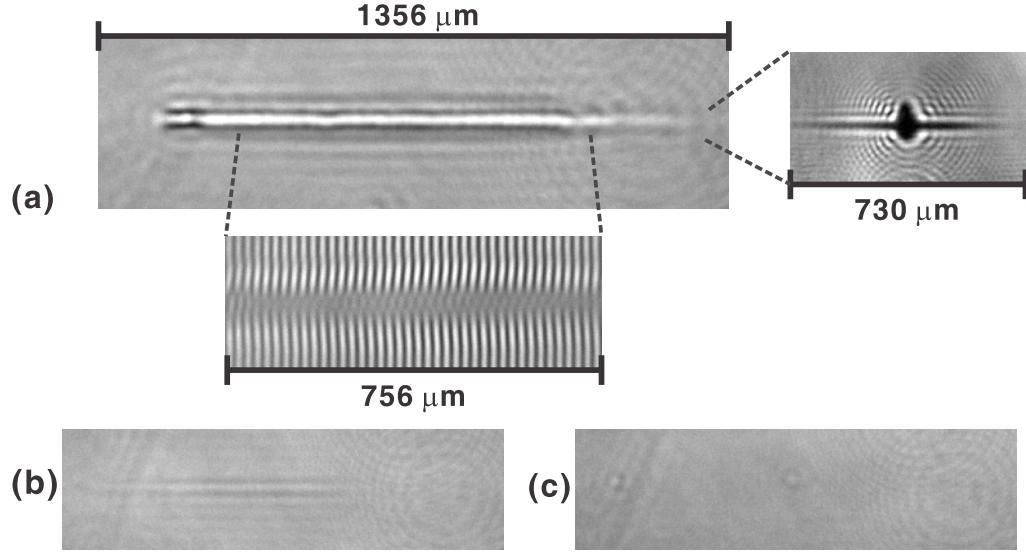


FIGURE 3.8: (a) Transverse (upper) and longitudinal (right) shadowgrams of the Ar plasma channel produced with 3.7-mJ ignitor and 36-mJ heater, along with the corresponding interferogram (lower) sampling the central region. With the same parameters, transverse shadowgrams are shown in cases when only the (b) ignitor and (c) heater was used. Detailed parameters are provided in the text.

the density of the plasma channel when the heater energy was raised from 22.8 mJ to 36 mJ. The heater alone can ionize the Ar gas when its energy is higher than 47.5 mJ, as shown in the corresponding shadowgrams. In the case of 58.5-mJ heater, the longitudinal shadowgram indicates that the heater can even ionize the gas atoms over a much larger space than that made by the ignitor. However, this random ionization process made by the energetic, long heater pulse significantly shapes the structure of the created plasma channel, which hinders the transfer of heater energy into the IB process that can further increase the plasma density and temperature of the gas region previously irradiated by the ignitor. Similar results were obtained, as shown in Fig. 3.9(b), when a higher ignitor energy of 6.3 mJ was introduced. As a consequence, a well-shaped plasma waveguide density profile cannot be achieved by increasing the heating energy with the current focusing of $f/5$ for the heater, since the ionization of gas by the heater itself limits the heating efficiency of plasma for waveguide production. The unfavorable ionization process made by the heater can be mitigated by using tighter focusing (smaller f of the focusing lens) for the heater, from which the Rayleigh region, where the focused heater beam exhibits high intensity capable of ionizing the gas atoms, can be reduced. The other solution is to use an axicon optical element to produce the line focus for the heater beam [11, 12]. Since the heater pulse energy is concentrated from the radial direction when the axicon is used, the unfavorable ionization process does not happen outside the focal region, which usually has a diameter $<20\text{ }\mu\text{m}$. The limited heating efficiency of plasma by the heater also limits the stability of the density profile of the

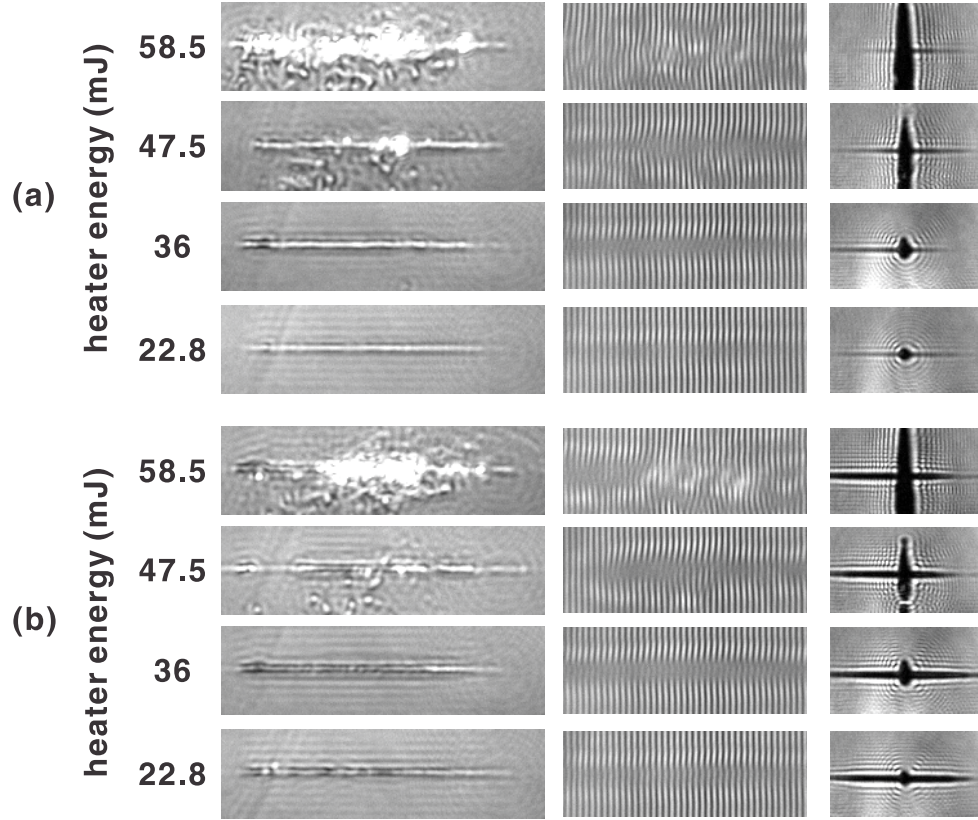


FIGURE 3.9: Transverse (left) and longitudinal (right) shadowgrams, along with the interferogram (center) measured for the study of the effect of the heater energy on Ar plasma channel production when the ignitor energy was set to (a) 3.7 mJ and (b) 6.3 mJ. The other parameters were the same as those producing the results in Fig. 3.8.

produced plasma channels. With 6.3-mJ ignitor and 36-mJ heater, Fig. 3.10 shows the transverse shadowgrams and interferograms corresponding to 5 consecutively produced Ar plasma channels. The results show significant variation of the length and plasma density distribution. The stability of produced plasma channels should be improved when a increased heating efficiency of plasma is achieved.

The time separation between the ignitor and heater pulse can be optimized in order to achieve a higher plasma heating efficiency. When 6.3-mJ ignitor and 36-mJ heater pulses are applied, Fig. 3.11 shows the measured shadowgrams and interferograms with various ignitor-heater time delays. From the longitudinal shadowgrams, it was observed that the heating of plasma is more efficient when the delay is longer than 67 ps, which is approximately one-third of the heater pulse duration (160 ps). When the delay becomes longer than 133 ps, the collisional IB heating and ionization process then extend the high plasma density region toward the region above the channel, where the heater arrives first and interacts with the seed plasma electrons created by the ignitor. Since the optical-field ionization process initiated by the ignitor also heats the plasma to some low temperature, a longer heater delay allow more seed electrons move to the outer radial region and then interact with the heater. Thus, the IB process occurs at a larger radial

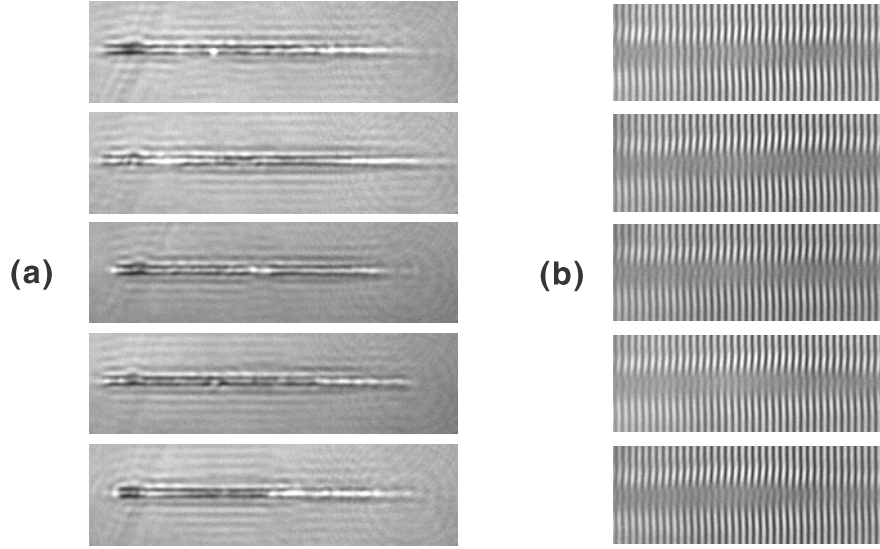


FIGURE 3.10: With 6.3-mJ ignitor and 36-mJ heater, the (a) transverse shadowgrams and (b) corresponding interferograms for a series of 5 measured Ar plasma channels. The other parameters were the same as those those producing the results in Fig. 3.8.

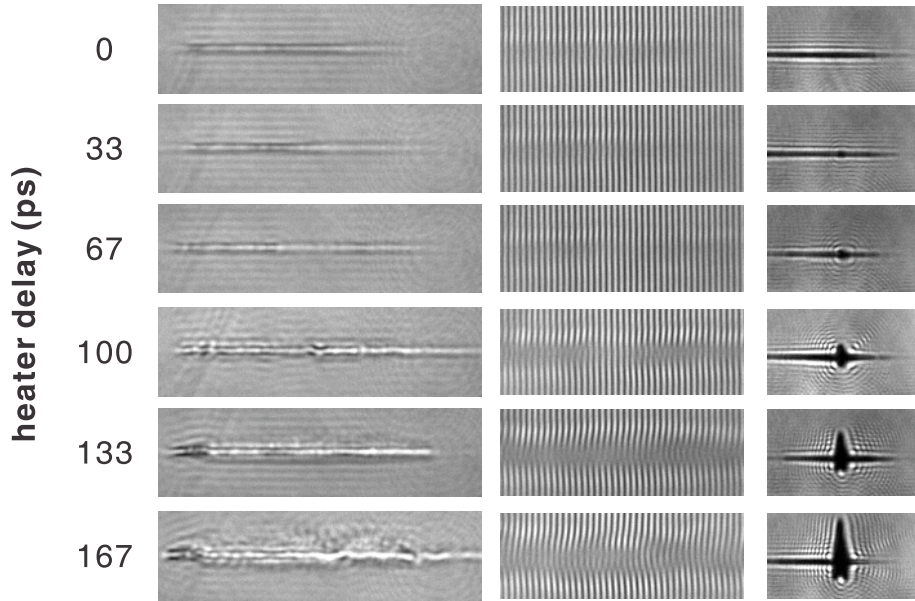


FIGURE 3.11: Transverse (left) and longitudinal (right) shadowgrams, along with the interferogram (center) measured when studying the effect of the heater delay on Ar plasma channel production with 6.3-mJ ignitor and 36-mJ heater. The other parameters were the same as those producing the results in Fig. 3.8.

distance. Using a tightly focused heater beam can inhibit the IB process induced in the regions away from the waveguide, since the heater intensity occurring away from focus (the center of the plasma channel) is reduced.

Time-resolved variations of plasma density profile can be observed by changing the delay of the shadowgram and interferogram probe pulse with respect to the ignitor pulse.

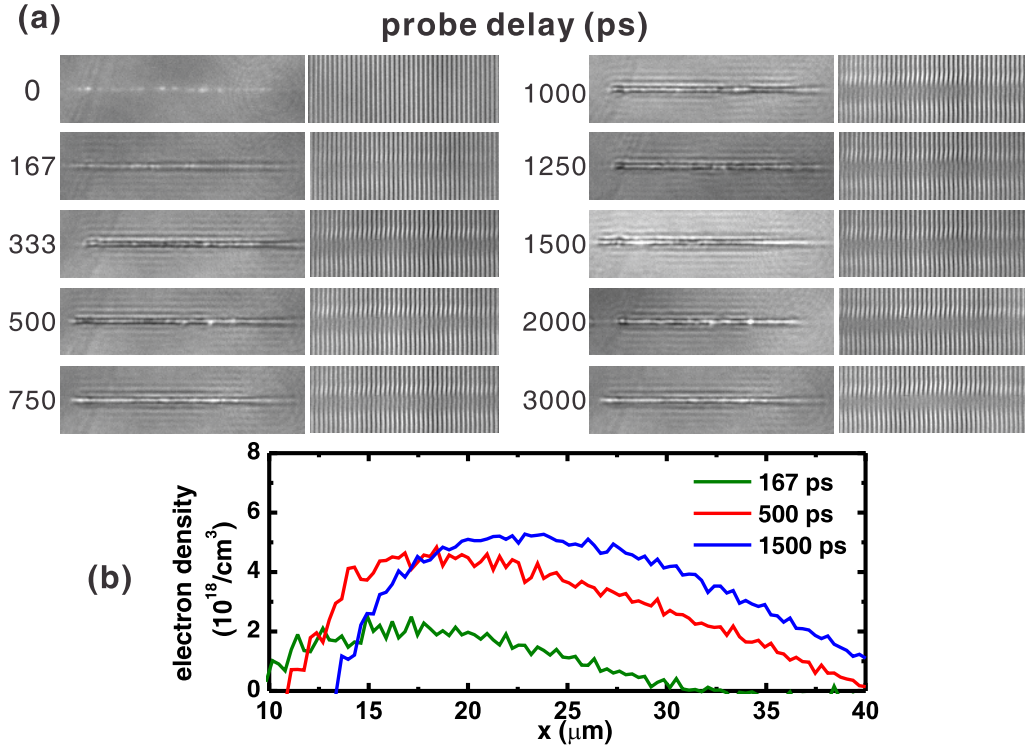


FIGURE 3.12: With 6.3-mJ ignitor and 36-mJ heater, (a) measured transverse shadowgrams and interferograms of Ar plasma channels for various probe delays and (b) retrieved plasma density profiles around the density peaks at selected probe delays. The other parameters were the same as those producing the results in Fig. 3.8.

With 6.3-mJ ignitor and 36-mJ heater, Fig. 3.12(a) shows the measured shadowgrams and interferograms with various ignitor-probe delays. The radial plasma electron profiles retrieved from the measured interferograms around their density peak are shown in Fig. 3.12(b) for selected probe delays. The results show that a rapid increase of plasma electron density occurs in the period of 200–500 ps after the arrival of the ignitor pulse. Afterwards, the expansion of plasma shifts the density peak to a larger radial position, until a delay of ~ 1500 ps.

Using of 6.3-mJ ignitor, 36-mJ heater, and an ignitor-heater delay of 100 ps, Fig. 3.13 shows the intensity-modulated ignitor pattern and the corresponding transverse shadowgrams and interferograms of the density-modulated Ar plasma structure. The ignitor pattern was created by passing the ignitor through the left side of the chipped mask shown in Fig. 3.7(b) and then imaging the ignitor with a demagnification of 5 on the target plane. The resulting shadowgrams and interferograms confirm the prediction that the plasma is produced in the regions where the ignitor and heater are spatially overlapped. As long as the heating efficiency can be improved, it is expected the effective hydrodynamic expansion of plasma can evolve into a density-modulated plasma waveguide to guide laser pulse for DLA in future experiments.

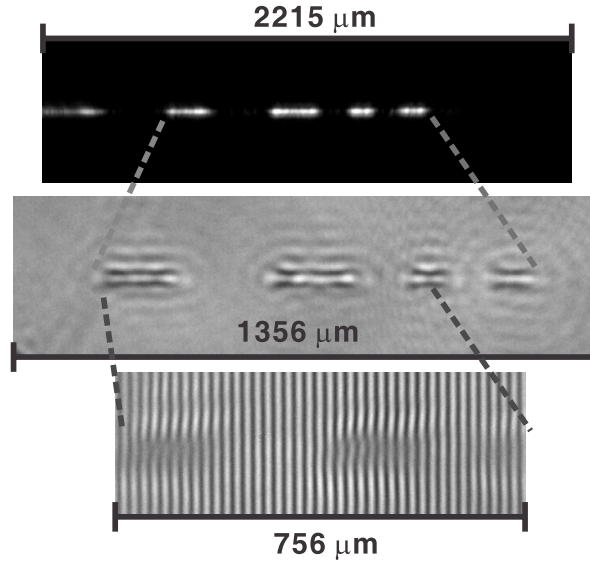


FIGURE 3.13: With 6.3-mJ ignitor and 36-mJ heater, intensity-modulated ignitor (upper) and the measured transverse shadowgrams (center) and interferograms (lower) of the corresponding Ar plasma structure. The other parameters were the same as those producing the results in Fig. 3.8.

3.2.2 Conclusions drawn from experimental results

By using the ignitor-heater scheme in the 90° geometry, in which the heater propagates orthogonally with respect to the ignitor through the gas target, production of density-modulated plasma channels has been demonstrated with Ar plasma. Experimental results show that an important challenge that has to be overcome is the ionization of gas atoms by the heater itself. If the heater produces the ionization, the IB heating process of the existing plasma created by the ignitor can be significantly inhibited. Since the heater has been focused by the lens with a relatively long focal length ($f/5$), the heater is capable of ionizing the Ar atoms over a large region when its energy is greater than 45 mJ. As a consequence, the IB process becomes less effective in further increasing the density and driving the hydrodynamic expansion of the existing plasma that are required for the formation of a high-quality plasma waveguide. To prevent the unfavorable ionization of gas made by the heater and improve the IB heating efficiency, a modification for the current heater configuration should be performed to reduce the focal length f , such as using a lens with a focal length <5 cm, for line focusing. Therefore, the volume where the heater intensity reaches the ionization threshold can be considerably reduced and the spatially overlapped IB heated space produced by the ignitor and heater can be smaller. In addition, the heater focusing lens can be replaced by an axicon, which focuses the heater pulse from the radial direction. In this configuration, seed electrons are created by the transversely projected ignitor and then heated by the heater line focus made by an axicon. Once a high IB heating efficiency is achieved for driving the expansion of plasma, a optimized plasma density profile [11, 13, 15, 16] with a high on-axis density

$>10^{19} \text{ cm}^{-3}$ and a density barrier $>5 \times 10^{18} \text{ cm}^{-3}$ that fulfills the guiding condition for the laser pulse can be realized. When a intensity-modulated ignitor is introduced on the Ar target, the experimental results demonstrate that a density-modulated plasma structure can be fabricated via the ignitor-heater scheme. This result provides the proof-of-principle foundation for producing the density-modulated plasma waveguides via the laser machining technique for future DLA experiments.

3.3 Micrometer-scale supersonic gas jet design, simulation and fabrication

The proposed DLA scheme requires a micrometer-scale supersonic gas jet nozzle. In prior work a variety of gas nozzles have been used, including the cryogenic systems with atomic clusters that allow the use of wire obstructions to define the gas density modulation [11, 12]. A strong motivation exists to reduce the system complexity by operating at room temperature, but this requires an effort to design, simulate, fabricate, and evaluate the performance of appropriate supersonic gas nozzles. We simulated and optimized the production of a uniform gas density profile at a specified distance from the nozzle and started developing fabrication methods that involve the use of additive manufacturing. Nitrogen and helium serve as the gas jet medium in simulations and experiments. Simulations for determination of the supersonic gas jet dimensions and resultant gas profile are conducted using the COMSOL multiphysics software with high Mach number fluid modeling physics. Micrometer gas jet nozzle prototype manufacturing is pursued through direct digital manufacturing techniques using stainless steel, titanium, and amorphous thermoplastic polyetherimide materials.

An example of a de Laval nozzle designed for this research is depicted in Figure 3.14. In (a), the side profile of the nozzle with the direction of fluid flow from left to right is shown. The flow constricts to the narrowest point of the design, or the critical point, and then expands after the critical point to increase the flow velocity and reduce the fluid density. In (b), the transition from left to right of the flow from a cylindrical pipe to a rectangular outlet is depicted, which is an essential factor in the design to obtain the requisite gas density profile. The most important consideration for the design of a de Laval nozzle for this research is the ratio of the cross sectional area of the critical point and the cross sectional area of the outlet. The ratio of the static reservoir pressure to the backing pressure of nearly perfect vacuum is kept high enough to ensure the fluid remains supersonic throughout the nozzle from the critical point to the exit. Ensuring the fluid remains supersonic within the nozzle reduces shock wave generation in the nozzle and provides a large degree of freedom regarding the length and shape of the expansion portion of the nozzle. The inlet portion is fixed as a 1 mm diameter pipe and

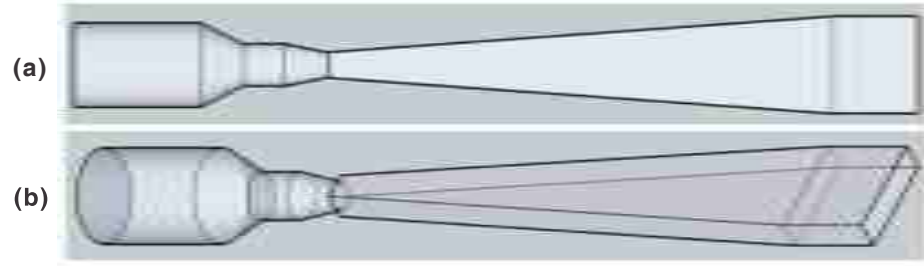


FIGURE 3.14: An example de Laval nozzle designed to produce the gas profile for an optical plasma waveguide. The nozzle begins as a cylindrical flow at the left, and transitions to rectangular flow at the critical point; (a) parallel projection of the nozzle; (b) transparent offset projection of the nozzle that shows the transition from a cylindrical flow system to an asymmetric rectangular flow system.

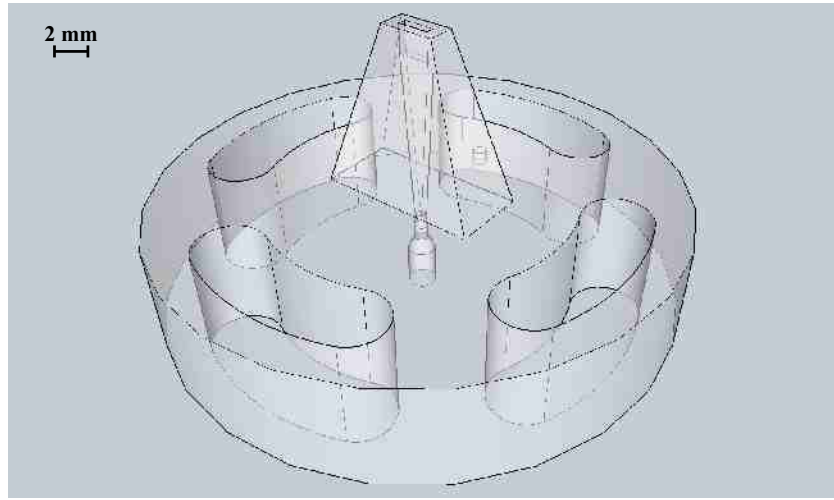


FIGURE 3.15: Offset transparent rendering of the de Laval micrometer-scale supersonic gas jet used in DLA experiments.

thus the diameter of the constriction to the critical point must be smaller than 1 mm to operate in the critical flow conditions.

The de Laval nozzle depicted in Fig. 3.14 is integrated into a metal body for integration with the DLA experiment. Figure 3.15 is an offset, transparent rendering of the nozzle design used in the experiment with the de Laval nozzle visible within the structure. The cylindrical entry into the de Laval nozzle is aligned with the 1 mm diameter flow feed pipe from the static reservoir. The nozzle transitions to a rectangular configuration at the critical point and the exit slit is visible at the top of the expansion section. The four mounting screw slots are visible in the base with the nozzle exit slit at the top of the expansion section. The inlet diameter for both nozzles is 2 mm, whereas the inlet pipe feed has a 1 mm diameter. The nozzle is designed this way to prevent any constriction of the 1 mm diameter feed pipe from any misalignment of the mounting hardware. The nozzle gradually constricts to a 1 mm diameter prior to the constriction to the critical point diameter of 0.6 mm.

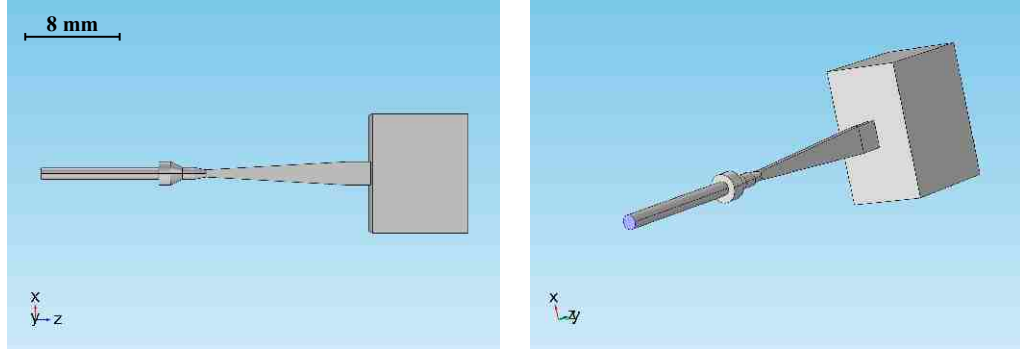


FIGURE 3.16: Depiction of the model for the frictional pressure loss simulation. The inlet boundary condition is identified by the blue disk in the right image. The inlet feed pipe is 10 mm in length with a 1 mm diameter. The constriction to the critical point is 4 mm in length and constricts from a 2 mm diameter to a 0.6 mm diameter.

3.3.1 Finite element analysis for nozzle design

The finite element analysis consisted of simulating the micrometer-scale supersonic slit jet design to evaluate the first principles analysis. These simulations were completed using COMSOL Multiphysics software. Only the simulations of the nitrogen slit jet design are presented here, but the same analysis was also applied to the helium nozzle. The simulations were initially focused on the expansion portion of the de Laval nozzles and the gas expansion behavior upon exiting the nozzle and expanding into the vacuum chamber. The outlet boundary conditions were set to simulate the conditions inside the vacuum chamber. Frictional pressure loss simulations introduced a feed pipe structure to analyze the friction effects in the flow system that are not accounted for in the isentropic first principles analysis.

The model for the frictional pressure loss simulation is shown in Fig. 3.16. The outlet boundary conditions for the square vacuum chamber remain the same as the initial simulation model. A 10 mm length of a 1 mm diameter inlet pipe with an additional 4 mm constriction to the critical point has been incorporated in the model to represent the flow length from the pulse valve to the critical point. The inlet boundary condition is now at the beginning of the inlet pipe, represented by the highlighted blue disk in Fig. 3.16.

There is a 2 mm rectangular extension at the end of the expanding portion of the de Laval nozzle. This extension maintains the designed exit cross sectional area and is added in an attempt to make the outlet gas density more uniform across the top. The frictional effects of this extension on the outlet gas density are also accounted for in the simulation. The 4 mm length constricted portion constricts from a 2 mm diameter to a 1 mm diameter and then to the 0.6 mm diameter critical point. The 2 mm diameter flow section was designed into the nozzle to avoid any blockage of the 1 mm diameter inlet point when the nozzle is mounted to the support structure in the vacuum chamber.

TABLE 3.1: Static reservoir pressure and temperature with the inlet flow pipe diameter and critical point diameter used for the helium and nitrogen de Laval nozzle solutions.

Pressure [psi]	Temperature [K]	Inlet diameter [mm]	Critical point diameter [mm]
100	293	1	0.6

This simulation is driven by the gas reservoir conditions given in Table 3.1 and provides for the effects of frictional pressure loss on the outlet gas density profile.

The target outlet gas number density for the supersonic slit jet is $1.25 \times 10^{19} \text{ cm}^{-3}$. COMSOL Multiphysics plots gas density in units of mass density, kg/m^3 , and does not have the option to plot in units of number density. For the analysis of the outlet density in this section, the gas number density for the supersonic slit jet is converted to be equal to 0.58147 kg/m^3 used in COMSOL. The desired shape of the outlet gas density profile is a flat density across the top at $500 \text{ }\mu\text{m}$ above the nozzle exit, with a width of at least $500 \text{ }\mu\text{m}$ perpendicular to the pump pulse propagation axis. The desired length of the gas profile in line with the pump pulse beam propagation axis is 2 mm . This profile provides a uniform spatial gas density for optical plasma wave guide generation.

3.3.1.1 Frictional pressure loss simulation with stability extension

The frictional pressure loss simulation accounts for the wall friction effects on the flow system from the pulsed valve exit to the critical point. The simulation with the profile stability extension includes the 2 mm extension at the end of the expansion length designed to stabilize the density profile. To accomplish this, several sections were added to the initial simulation model to take the wall friction of the flow system in consideration. Figure 3.16 shows the frictional pressure loss simulation model with the direction of flow from left to right. A 10 mm length of a 1 mm diameter pipe is added to represent the flow system from the pulsed valve to the nozzle mount. The nozzle constriction from a 2 mm diameter flow to a 0.6 mm diameter critical point is added after the 10 mm pipe length. Figure 3.17 shows the target density isosurface profile plot for the nitrogen frictional pressure loss simulation with a designed reservoir static pressure of 100 psi . These results indicate that the target density is achieved prior to the nozzle exit plane and within the vacuum chamber due to the effects of wall friction on the fluid flow. There is also a distinct dip in density profile in the center of the flow system due to the wall friction.

Using the same design dimensions for the nitrogen nozzle, the simulated reservoir static pressure was increased incrementally until the target density profile was achieved beyond the nozzle exit plane and in the vacuum chamber. These results can be seen in

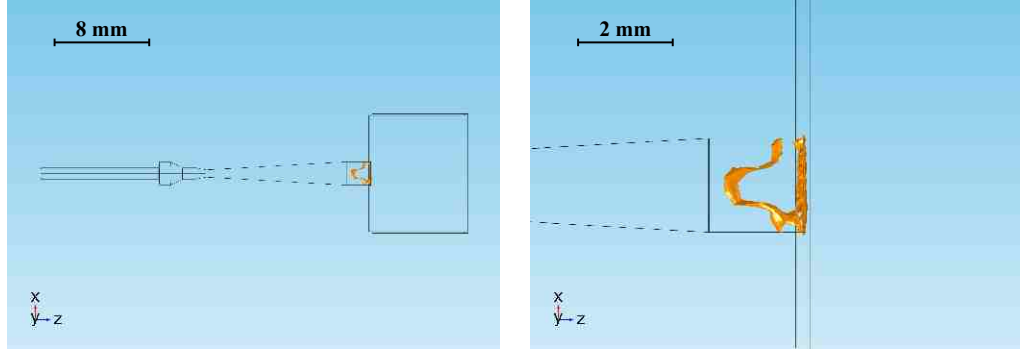


FIGURE 3.17: Nitrogen nozzle target gas density isosurface plot from the frictional pressure loss simulation with a 100 psi reservoir pressure. The target gas density is reached within the nozzle expansion chamber prior to the exit into the vacuum chamber.

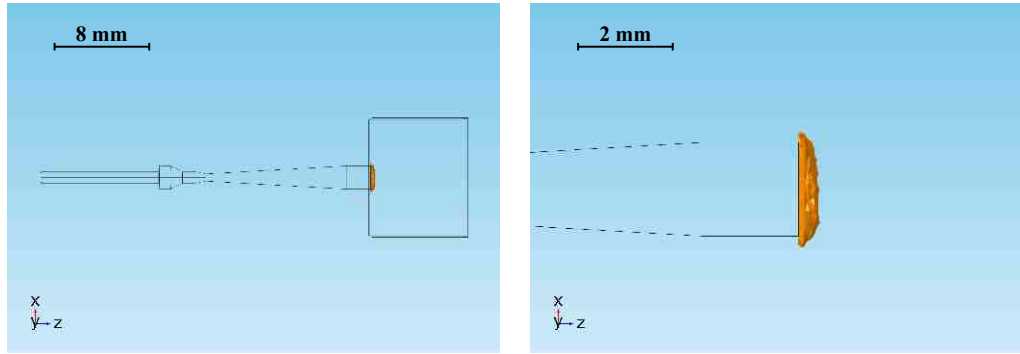


FIGURE 3.18: Nitrogen nozzle target gas density isosurface plot from the frictional pressure loss simulation with a 190 psi reservoir pressure. The target gas density is reached after the nozzle exit in the vacuum chamber.

Figure 3.18, where a reservoir static pressure of 190 psi resulted in achievement of the target density profile approximately 400 μm above the exit plane.

Figure 3.19 is a plot of the outlet nitrogen gas density by height above the outlet. The horizontal axis of the plot corresponds to the width of the slit jet perpendicular to the pump pulse propagation axis. The vertical axis of the plot is the nitrogen gas mass density. The height that the profile reaches the target density is 400 μm above the exit plane, which is below the target height of 500 μm . This is acceptable because the laser can be lowered to 400 μm above the outlet. However, the slit jet structure could obstruct the pump pulse in this configuration. The density profile width normal to the pump pulse propagation axis is approximately 200 μm and the desired width is 500 μm .

3.3.1.2 Mach number and shock wave analysis

Shock waves are a spontaneous change in fluid flow conditions where the velocity decreases and the pressure increases sharply [17]. Shock waves can only occur if the initial flow is supersonic. Shock waves significant to the design of a supersonic flow system because a shock wave can deform or redirect the flow in the system, and in

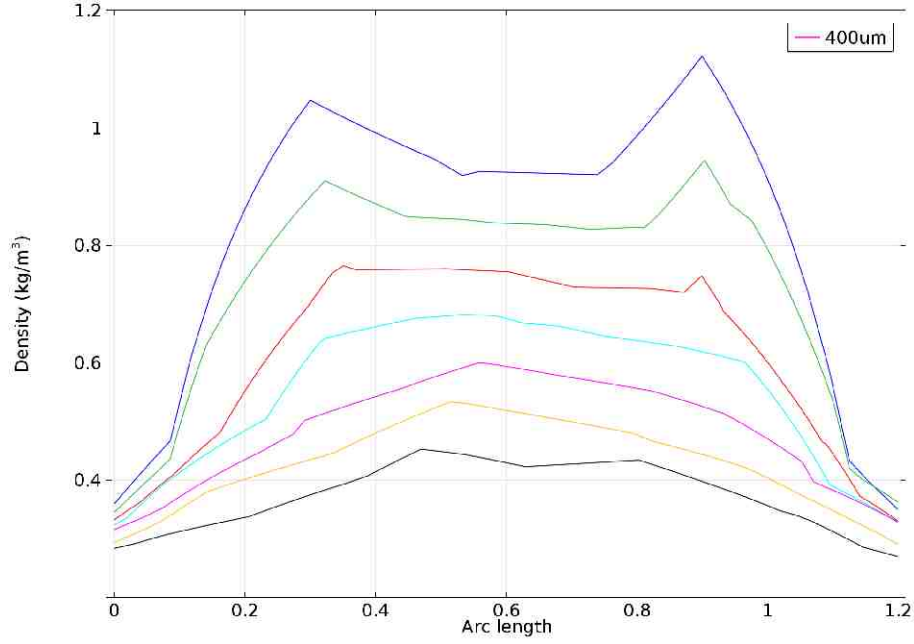


FIGURE 3.19: Nitrogen gas density at various heights across the width of the nitrogen nozzle outlet for the frictional pressure loss simulation with the 2 mm straight extension at 190 psi reservoir pressure. The target nitrogen gas density is reached at 400 μm above the center of the slit jet outlet.

this particular case disrupt the form or position of the target density profile. A shock wave will occur in the flow system under consideration only beyond the critical point, after the fluid has accelerated above Mach 1 and if it then decelerates below supersonic velocity. This means that the primary region of concern when considering shock waves is the expansion length of the nozzle after the critical point or choke point where the fluid is supersonic.

Shock waves can be generated by three factors in this supersonic gas jet design; deformities in the wall surface that disrupt the flow, a change in the direction of the flow that makes the flow nonlinear, or a deceleration of the flow due to excessive backing pressure present in the vacuum chamber. Deformities in the wall surface can be any discontinuity in the material that makes the wall not smooth. These deformities can arise through the manufacturing process, corrosion, or any damage to the interior surface of the nozzle. Deviations from the linear flow occur due to significant changes of geometry or cross sectional area of the flow system. Finally, if the reservoir pressure to backing pressure ratio is not high enough, then the fluid may decelerate below Mach 1 after the critical point prior to the exit plane and cause a shock wave within the expansion length.

Figure 3.20 are isosurface plots of the supersonic regions from Mach 1 to Mach 3 for the nitrogen supersonic gas jet nozzle without the stability extension at 180 psi static reservoir pressure. The flow appears to develop into a fully supersonic flow after the critical point and continues to accelerate into the vacuum chamber, which is ideal. The

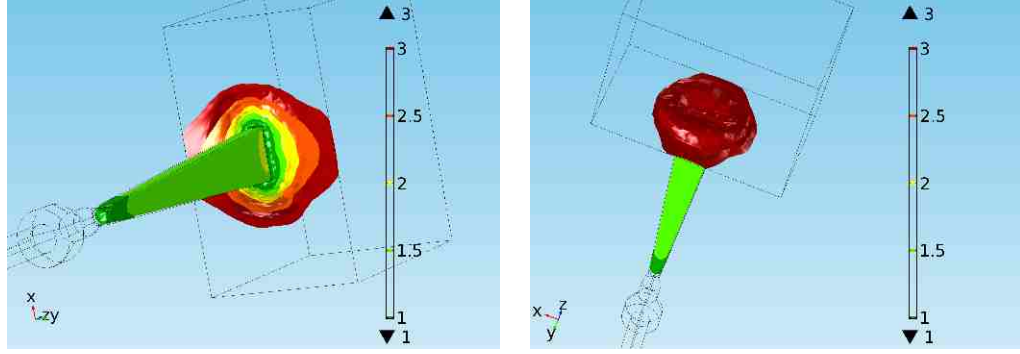


FIGURE 3.20: Isosurface 3D plot of the supersonic velocity regions from Mach 1 to Mach 3 for the nitrogen supersonic gas jet nozzle without the stability extension at a 180 psi static reservoir pressure. The scale indicates the Mach number and corresponding color per isosurface. The left image displays the continuous acceleration from the critical point. The right image depicts the expanding and accelerating gas in the vacuum chamber represented by the red Mach 3 isosurface plot.

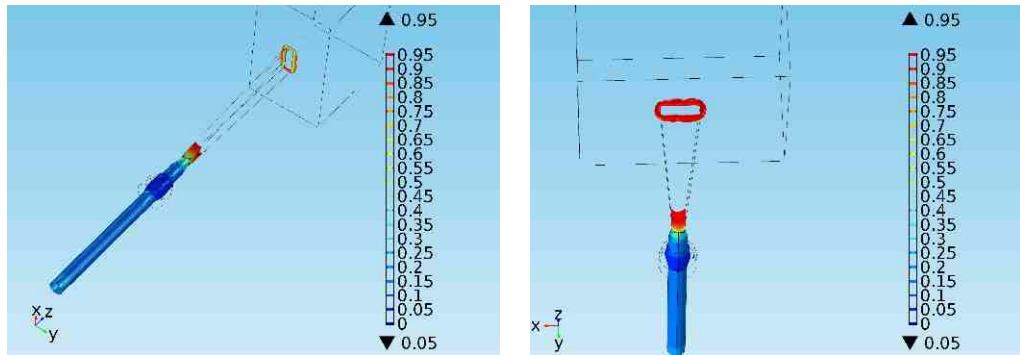


FIGURE 3.21: Isosurface plot of the subsonic regions for the nitrogen gas jet without the stability extension at a 180 psi reservoir pressure.

plot shows the Mach 3 region fully inside the vacuum chamber. If higher Mach numbers were plotted the plot would show a continuous acceleration away from the nozzle exit. Two regions of concern where shock waves could exist are seen in Figure 3.20. The first region of concern is the beginning of the expansion length after the critical point, and the second is the area immediately around the perimeter of the nozzle exit in the vacuum chamber. The flow is at Mach 1 in these regions. Thus this is where a shock wave is likely to occur.

Figure 3.21 are isosurface plots of the subsonic regions for the nitrogen supersonic gas jet nozzle without the stability extension at 180 psi static reservoir pressure. In the subsonic plots the two regions of concern, the beginning of the expansion length and the area around the perimeter of the nozzle exit, are clearly evident by the red isosurface. Consider the first region of concern at the beginning of the expansion length. Since a shock wave will only occur when a supersonic fluid decelerates below Mach 1, the first region of concern is not a shock wave and is simply a transition from subsonic to supersonic fluid flow [17]. The second region of concern, the area around the perimeter

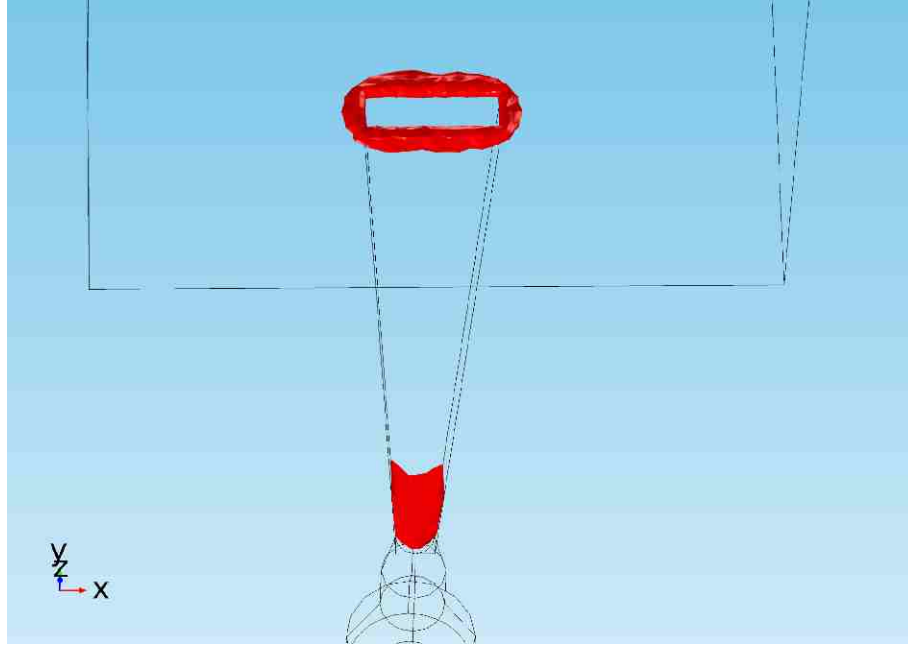


FIGURE 3.22: Isosurface plot of the Mach 1 ($M=1$) regions at the beginning of the expansion length and at the area around the perimeter of the nozzle exit.

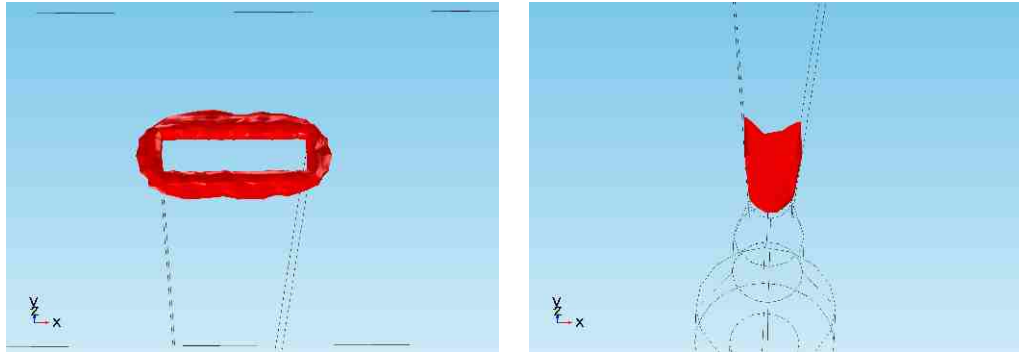


FIGURE 3.23: Isosurface plots of the Mach 1 ($M=1$) regions at the beginning of the expansion length and at the area around the perimeter of the nozzle exit. The left image is the shock wave generated by the flow exiting the nozzle, and the right image is the transition from subsonic to supersonic flow after the critical point.

of the nozzle exit, is a shock wave since the fluid is decelerating here as it becomes a non-linear flow upon exiting the nozzle into the vacuum chamber at the exit plane. Figures 3.22 and 3.23 are isosurface plots of the Mach 1 regions in the simulation of the nitrogen supersonic gas jet nozzle without the stability extension at 180 psi static reservoir pressure. The isosurfaces in these figures represent the transition from subsonic to supersonic flow at the beginning of the expansion length, and the shock wave generated at the nozzle exit. The shock wave generated at the nozzle exit is outside of the nozzle flow area and thus does not disrupt the linear flow of the nozzle. This shock wave assists in the continuity of the density uniformity as it propagates to the target height of 500 μm above the nozzle exit.

3.3.2 Nozzle fabrication

The micrometer supersonic slit jet de Laval nozzle was manufactured through collaboration with the Pennsylvania State University (PSU) Applied Research Laboratory (ARL). Manufacturing was conducted at the Center for Innovative Materials Processing through Direct Digital Deposition located at the PSU Innovation Park. Additive Manufacturing in metals is a cutting edge technology with constantly expanding potential and capabilities. The term AM is commonly referred to as 3D printing and encompasses processes such as powder bed fusion, direct metal laser sintering, direct metal laser melting, selective laser melting, laser curing, and laser melting. Direct Metal Laser Sintering (DMLS) is the specific AM process used to produce the supersonic gas jets for this research. The platform that produced the metal nozzles is the Electro Optical Systems (EOS) M280 with an image of the platform provided in Figure 3.24. The EOS M280 has a build volume of $250 \times 250 \times 290 \text{ mm}^3$ and uses a 200–400 W Yb-fiber laser with a spot size of $80 \text{ }\mu\text{m}$ to sinter the metal powder during component production. The component creation process begins with a solid build plate of the selected metal mounted within the M280 build volume. A single layer of metal powder is then deposited across the base plate mechanically. The layer thickness varies in the range of 20–60 μm depending upon the grain diameter of the metal powder used for production. The laser then welds that layer of the component design and a new powder layer is deposited and the process repeats as the DMLS platform continues the build vertically. Figure 3.25 shows three prototype nozzles produced in titanium to determine the feasibility of producing these designs. The visible support structure in Fig. 3.25 is the 2 mm substrate on the base of each plate, which was removed by wire electronic discharge machining (EDM) post-processing. The smallest aperture for these designs was the 0.2 mm diameter critical point of the circular nozzle at the far right which was successfully produced by the EOS M280. The EOS M280 can produce components in stainless steel, nickel, aluminum, and titanium alloys. The nozzles could be produced in titanium and aluminum. Titanium was the preferred material due to its hardness and resistance to damage. The titanium nozzles required heat treatment and EDM post-processing before they could be utilized in experiments.

Component post-processing for titanium micrometer supersonic nozzles involved heat treatment, wire EDM, and in one special case plunge EDM. The heat treatment for titanium was required to anneal material stresses imposed in the components from temperature differentials that occur during the layered DMLS production process. Heat treatment consisted of heating the components to 650°C for 3 hours, while still attached to the solid titanium build plate. The heat treatment was conducted in an argon gas environment to prevent corrosion of the titanium. Following the heat treatment the nozzles were removed from the titanium build plate by cutting them from the substrate



FIGURE 3.24: EOS M280 DMLS platform was used to manufacture the micrometer supersonic gas jet.



FIGURE 3.25: Three concept nozzles printed in titanium still mounted to the solid titanium build plate. The left nozzle has a 6 mm long slit outlet, the center nozzle a 2 mm long slit outlet, and the right nozzle a 1.4 mm diameter circular outlet.

support structure by wire EDM.

Figure 3.26 is an image of the final nitrogen nozzle design produced by the EOS M280 at the CIMP-3D based on simulation results presented previously. A helium nozzle was also produced with the only difference between the two being that the nitrogen outlet slit is 2.0 mm long, and the helium outlet slit is 2.3 mm long. The left image is the top of the nozzle and the surface is visibly rougher than the bottom surface in the image at left. The right image is the bottom of the nozzle that was cut by wire EDM from the substrate. The roughness of the top surface is due to the fact that it is the weld surface created by the DMLS process.



FIGURE 3.26: Final nitrogen supersonic micrometer gas jet nozzle created in titanium after post processing. The left image is a view of the top of the nozzle with the outlet stem, and the right image is a view of the bottom of the nozzle with the 2 mm diameter inlet.

Surface characterization of the titanium slit jet nozzles was completed with optical profilometry at the PSU MCL, and with computed tomography (CT). Optical profilometry successfully characterized the exterior surfaces but was not suitable for analyzing the interior surfaces due to the nozzle geometry. To fully characterize the interior surfaces the nozzle would have to be cut to fully expose an interior wall to the optical scope. The CT scan was able to scan the expansion length of the nozzle but was unable to resolve regions such as the critical point due to interference from the nozzle base plate. Again, the nozzle would have to be cut by removing the base plate to obtain a full CT scan image of the flow length.

The titanium nozzle after post processing had three distinct types of surfaces. The first and roughest surface type is the previously mentioned weld surface. The weld surface is the surface of the material sintered by the laser during the DMLS process. The weld surface has a wavy texture that would be expected from molten metal that cools to a solid form. The second surface type is the wall surface. The wall surface of the titanium nozzle is built by the layered sintering process as the component is built vertically. The wall surface roughness results from titanium powder particles binding to the molten titanium during the production process. If any portion of the titanium metal powder grain lies within the 80 μm diameter spot laser as it sinters the weld surface, then that grain becomes part of the wall surface. The titanium grains used for this nozzle production were 35 μm in diameter, so deformities of 35 μm maximum dimension were expected on the wall surfaces. Wall surfaces are the most significant

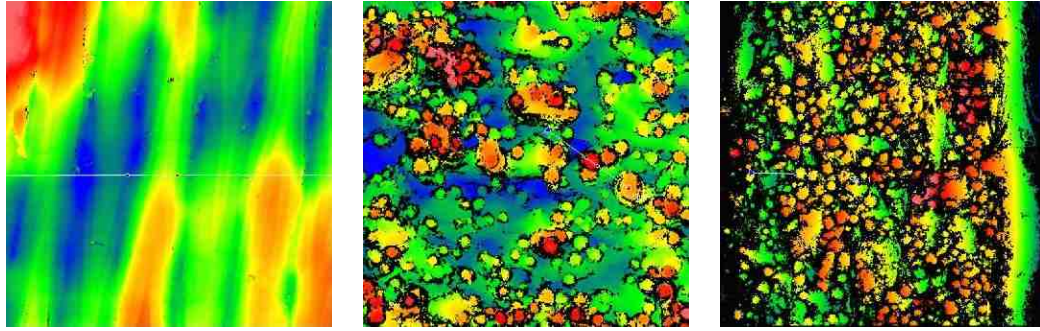


FIGURE 3.27: Optical profilometry images of the titanium nozzle surfaces. The left image is of the weld surface. The center image is of an exterior wall surface of the nozzle base. The right image is an interior surface image taken near the exit plane of the expansion length, and the transition to a top weld surface can be seen at the far right of the image. For all images blue is the lowest height and red is the highest point.

since these comprise the walls of the flow system within the nozzle. The third type of surface is the wire EDM surface, which is the right image in Figure 3.26. The EDM surface results from the separation of the nozzle from the solid titanium build plate by the EDM process. The EDM surface was the smoothest surface after post production processing and is located on the bottom of the nozzle.

Examples of optical profilometry images for the weld and wall surfaces are provided in Fig. 3.27. The left most image is an optical profile of the weld surface of the base plate of the nozzle. The maximum difference in measured height for the weld surface is 37 μm and the greatest feature width is 155 μm . The center image and the right image of Fig. 3.27 are of wall surfaces from the titanium nozzle base plate and the expansion length, respectively. In these images the spherical surface grains represent to the titanium grains captured on the during the laser sintering process. These grains have an average diameter of 35 μm as expected and of these can have lengths of hundreds of micrometers. The height across the wall surfaces can vary by as much as 110 μm . The height of these grain clusters can potentially cause turbulence and shock waves in the expansion length of the nozzle. In the far right image of Fig. 3.27 the transition of the scan from the grainy wall surface to the wavy weld surface can be seen by the solid green/yellow region at the right edge of the image, which represents the weld surface at the exterior of the exit plane of the nozzle.

CT scans of another nitrogen titanium nozzle confirmed the surface feature dimensions of the interior wall of the expansion length. The heights of the deformities on the interior surface walls varied up to 140 μm and the length of the deformities up to 300 μm . Figure 3.28 is a CT scan of a titanium nitrogen nozzle taken at the COMP-3D facilities. The flow region of the nozzle around the entrance and critical point are not resolvable due to interference from the nozzle base plate, but the wall features in the expansion length of the nozzle are clearly identifiable. Further surface characterization

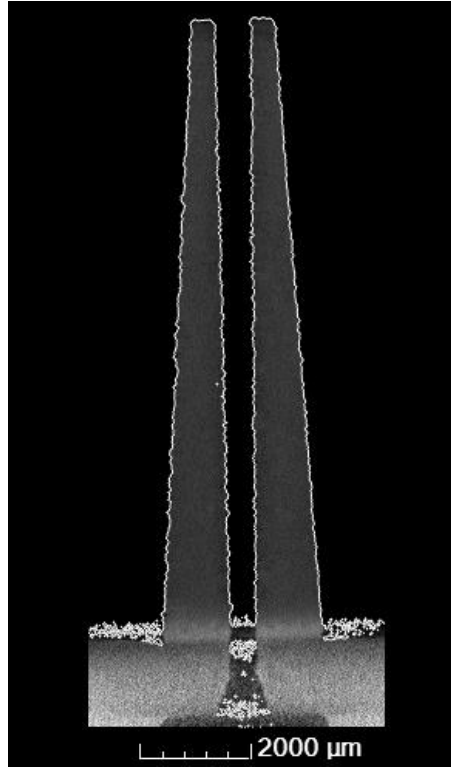


FIGURE 3.28: CT scan of a titanium nitrogen nozzle expansion length.

of the nozzle interior would either require destructive analysis of the nozzle to expose the interior for optical profilometry, cutting of the nozzle to remove the base plate for CT, or production of replicas of the nozzle without a base plate for CT.

3.3.3 Conclusions drawn from nozzle design and fabrication

The micrometer-scale supersonic slit jet nozzle was successfully designed based on the principles of compressible fluid dynamics for a 100 atm reservoir static pressure to obtain a target gas number density profile of $1.25 \times 10^{19} \text{ cm}^{-3}$ at approximately 400 μm above the nozzle outlet. The design was then simulated with COMSOL Multiphysics, which tested the first principles analysis and determined the frictional effects on the density profile. The frictional pressure loss simulations, with the feed system added, revealed that the friction effects prior to the critical point may affect the outlet density and require adjustment of the design. The frictional pressure losses resulted in a reduction of the outlet density and thus required a reduction in the outlet-to-critical-point cross sectional area ratio. The final nozzle design required an 80 psi increase in reservoir pressure to 180 psi to compensate for the wall friction effects.

The designs were fabricated with additive manufacturing techniques to the specified dimensions for asymmetrical designs that were difficult, if not impossible, to seamlessly construct through machining techniques. The titanium nozzles were rapidly constructed with minimal post-processing. More advanced design are possible through additive

manufacturing to include internal cooling manifolds for extended use if necessary, as opposed to an external cooling system built onto the nozzle surface.

The first objective of future work would be experimentation with appropriate diagnostics (shadowgraphy and interferometry) to characterize the outlet density of the helium and nitrogen nozzles. This characterization would help to validate the design and simulations of the nozzle, determine the presence of gas clustering, and observe any boundary layer or shock wave interference of the density due to internal surface deformities. Another possibility to consider is the refinement of surface characterization of the interior flow system walls. This can be accomplished by building components of the nozzle that consist of only the flow system and surrounding material without the mounting base plate. The special samples can then be cut in half and provide proper exposure of the interior wall surface for a complete optical scan. The components without the base plate can also be CT scanned over the full flow length without interference from the base plate. This research has demonstrated an ability to produce complex flow systems on a micrometer scale through additive manufacturing. While directly supporting the work on direct laser acceleration, this capability has multiple applications across industry and science in the development and application of micrometer flow systems.

Chapter 4

Radially polarized ultrashort pulse characterization

Experimental setups designed for generation and characterization of radially polarized short pulses used to drive DLA are presented in this chapter, and are related to Tasks 4 and 5 of the project. In Sec. 4.1, we present experimental results from production of femtosecond, radially polarized laser pulses with pulse energies at a level of millijoule, meeting the requirements of this DLA approach. Next, in Sec. 4.2, experimental results are introduced for a novel angle-multiplexed spatial-spectral interferometric technique capable of simultaneously reconstructing the phase and polarization of a femtosecond laser pulse for use in DLA.

4.1 Generation of ultrafast radially polarized laser pulses

Radially polarized beams are needed in DLA schemes employing waveguides such as plasma channels. As has been demonstrated by simulation, radial polarization facilitates production of strong longitudinal component of the electric field at focus [3], which can accelerate charged particles and transversely confine the electron beam traveling over extended distances. Such beams are useful not only for DLA schemes, but many other applications such as the mitigation of thermal effects in cylindrical laser amplifiers, microscopy, laser trapping, and laser materials processing [18]. Multiple passive methods have been designed to convert the laser with conventional polarization (linear or circular polarization) into the desired radial polarization state. Spatially variable polarization rotation can be achieved by segmented spatially variable $\lambda/2$ plates [19] or a liquid crystal (LC) display [20]. Those methods are more appropriate for DLA, since the required high energy (a few mJ), fs radially polarized laser pulses can be easily converted from the laser pulses produced by a CPA laser system. Figure 4.1 shows the system of a commercial LC converter [20] that has been used in our experiments. The device's principle of

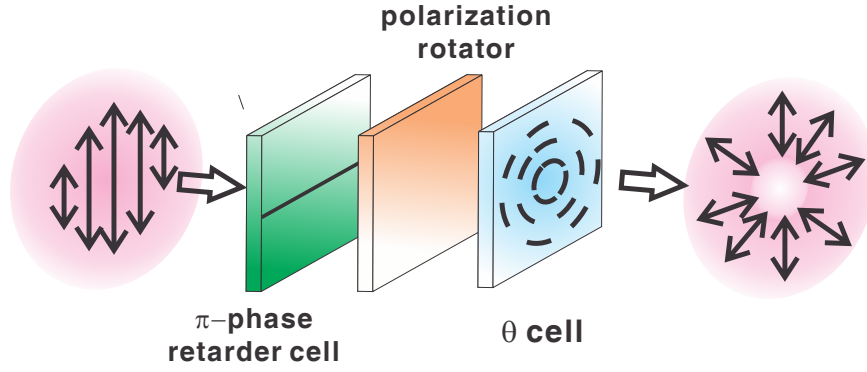


FIGURE 4.1: Configuration of the LC polarization converter.

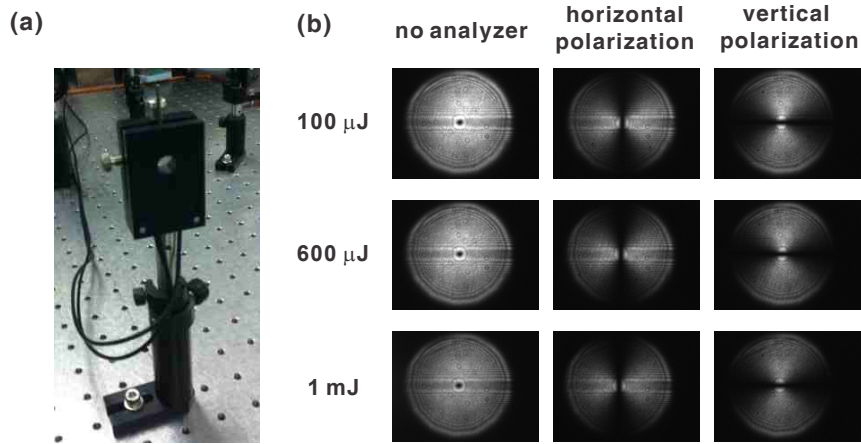


FIGURE 4.2: (a) The LC radial polarization converter; (b) intensity distributions of converted, radially polarized laser pulses (first column) and corresponding horizontal (second column) and vertical (third column) components taken with a optical analyzer.

operation is based on a 2-D array of LC cells, which can be controlled to rotate the input linearly polarized laser pulse into a radial polarization state. The θ -cell rotates the polarization of a linearly polarized laser pulse into a radial polarization. The exact phase difference adjustment between the upper- and lower-half of the field to produce a radially polarized pulse is provided by the π -phase retarder. Moreover, changing the voltage to the polarization rotator permits easy conversion between the radial and azimuthal polarization state. Compared to the converter made with segmented phase shifters, the properly arranged LC cells can continuously rotate a local polarization state of the laser field with a higher spatial resolution, which helps to improve the purity of the needed radial field for driving DLA.

An image of the LC radial polarization converter with a 10-mm diameter aperture (ARCOptix, model RADPOL4) is shown in Fig. 4.2(a). The test results in Fig. 4.2(b) show the successful conversion of linearly polarized 40-fs laser pulses from an ultrafast

laser system to radially polarized femtosecond laser pulses with increasing pulse energies, up to 1 mJ. An analyzer was inserted in front of a CCD to record the intensity distribution of vertical and horizontal components of converted laser pulse with radial polarization. The results shown in Fig. 4.2(b) match well with expected intensity distributions. The LC converter has been tested with 40-fs laser pulses and with energies of up to 2.3 mJ. As the laser pulse energy increases, no significant change of the intensity distribution is observed. This means that the nonlinear phase change of the converted laser pulse, which is proportional to the peak intensity of the laser pulse, is still insignificant in this intensity range.

4.2 Characterization of ultrafast radially polarized laser pulses

Few methods of characterization of laser beams with axially symmetric polarization have been reported to date [21], particularly for short laser pulses. A novel technique has been developed, capable of simultaneous reconstruction of the linear polarization state and the spectral phase of a short pulse, which is particularly suitable for characterization of radially polarized short pulses. Spatial-spectral interferometry techniques, such as spatially encoded arrangement for temporal analysis by dispersing a pair of light E-fields [58], can be used to extract the spectral phase difference between the signal pulse and the reference pulse [22]. We extended this technique to an angularly multiplexed geometry, in which the linear polarization state can also be simultaneously measured. Spectral interference is produced between an arbitrary polarized signal pulse and two orthogonal linearly polarized reference pulses. The accuracy of this technique has been verified by reconstructing the known relative spectral phase arising from material dispersion and the known elliptical polarization state. Measurement of the relative spectral phase and the spatially variable polarization state of a radially polarized pulse is also demonstrated. An additional independent measurement of the spectral phase of reference pulses provides absolute spectral and temporal characteristics of the signal pulse.

4.2.1 Description of the method

A signal beam with an arbitrary polarization is sent to the arrangement illustrated in Fig. 4.3(a), in which two orthogonally polarized reference beams are used. The signal pulse is temporally overlapped with the two reference pulses incident at two small angles ($\theta_1 > \theta_2$), producing interleaved fringes in the spatial (vertical) axis of the spectrometer image plane, as shown in Fig. 4.4(a). The spectral phase-retrieval algorithm is similar to the SEA TADPOLE Fourier-filtering algorithm [22]. Two reference beams are used instead of one and the polarization state of the signal pulse is subsequently measured,

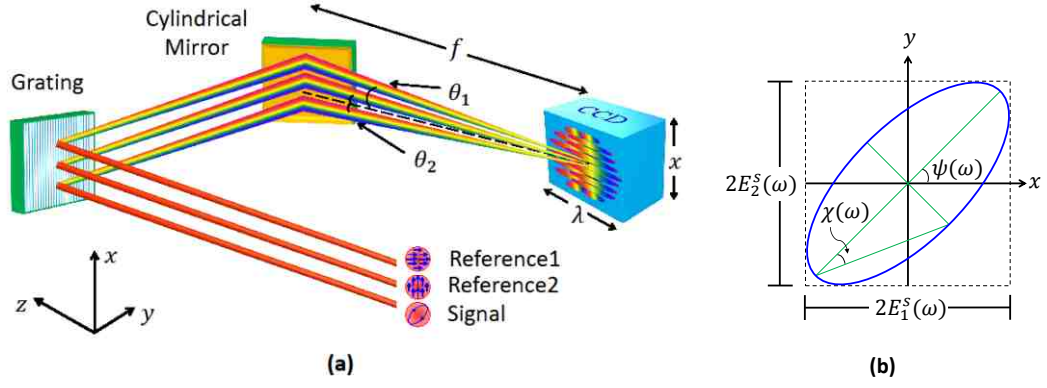


FIGURE 4.3: (a) Principle of the angle-multiplexed spatial-spectral interferometric technique. After being dispersed by a grating, two reference pulses and the signal pulse are vertically multiplexed on a cylindrical mirror and reflected at small angles θ_1 and θ_2 . A CCD camera is used to record the 2D interference pattern produced at the focus of the cylindrical mirror. (b) The orientation angle $\psi(\omega)$ and the ellipticity angle $\chi(\omega)$ of the polarization ellipse

together with its spectral phase. The retrieval process is illustrated in Fig. 4.4 and summarized as follows. A one-dimensional Fourier transform of the interleaved spectral interferogram is performed along the spatial (vertical) axis, yielding four sidebands. These sidebands can be filtered and inverse-Fourier transformed back to the spatial frequency domain. The resulting product of the interfering fields is divided by the spectral field of the reference pulse to obtain the spectral field of the signal and therefore the spectral phase difference between the signal and the corresponding reference pulses. Those two spectral phase differences are subsequently subtracted and used in conjunction with the separately measured phase difference between the two reference pulses. The relative spectral phase between the two polarization components of the signal pulse is calculated by using these phase differences. The spectral fields corresponding to two polarization components of the signal beam and their relative spectral phase difference can be used to determine the complete polarization state of the measured signal pulse.

Consider the geometry of Fig. 4.3(a), where the electric field of an arbitrary polarized signal pulse \vec{E}^s at any coordinate \vec{r} is the sum of two orthogonal polarization components with magnitudes $E_1^s(\omega) \exp[i(\vec{k}_1^s \cdot \vec{r} + \phi_1^s)]$ and $E_2^s(\omega) \exp[i(\vec{k}_2^s \cdot \vec{r} + \phi_2^s)]$, where $E_1^s(\omega)$ and $E_2^s(\omega)$ are their amplitudes, \vec{k} is the wave number, x is the vertical component of \vec{r} , and ϕ is the spectral phase. The reference pulses are defined as $E_1^r(\omega) \exp[i(\vec{k}_1^r \cdot \vec{r} + \phi_1^r)]$ and $E_2^r(\omega) \exp[i(\vec{k}_2^r \cdot \vec{r} + \phi_2^r)]$. The interferogram $I(\omega, x)$ is calculated by taking the sum of $|\vec{E}_i^r + \vec{E}_i^s|^2$ and has the form

$$I(\omega, x) = \sum_{i=1}^2 \left[I_i^s(\omega) + I_i^r(\omega) + 2\sqrt{I_i^s(\omega)I_i^r(\omega)} \cos(2kx \sin \theta_i + \phi_i^s(\omega) - \phi_i^r(\omega)) \right], \quad (4.1)$$

where $I_i^s(\omega)$ and $I_i^r(\omega)$ are the spectral intensities, θ_i are the half-crossing angles between

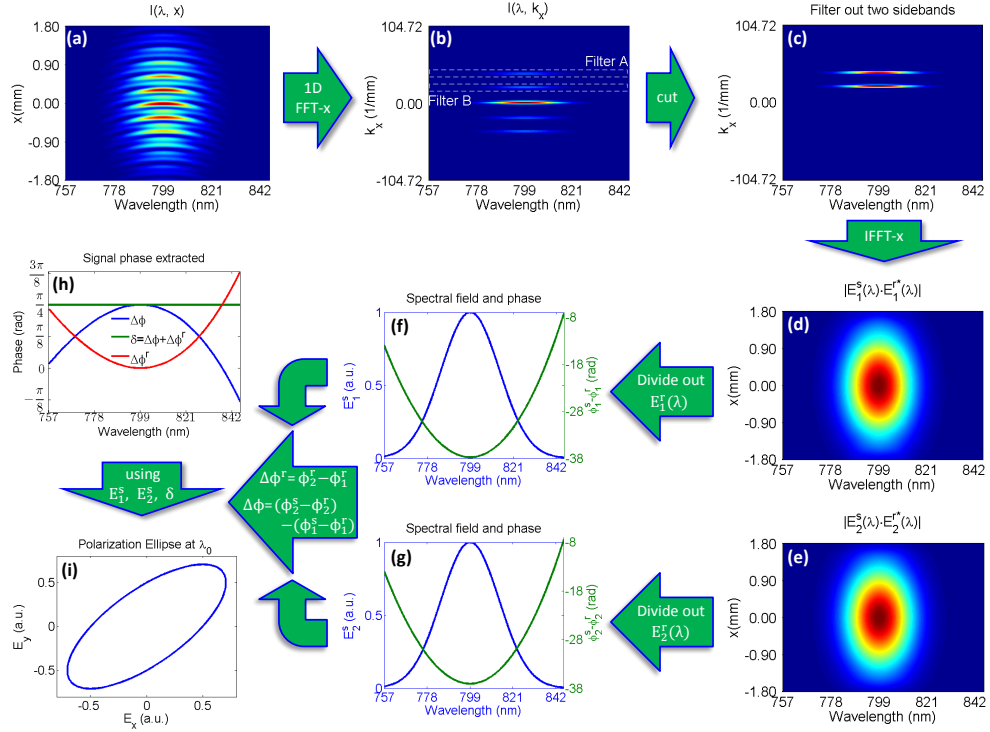


FIGURE 4.4: The spectral phase and polarization ellipse retrieval algorithm using simulated data. (a) Simulated interferogram corresponding to two orthogonal reference pulses and a signal pulse. The reference pulses have a group delay dispersion (GDD) of -100 fs^2 and -30 fs^2 and a third-order dispersion (TOD) of -250 fs^3 and -50 fs^3 , respectively. The signal pulse has a GDD of 2000 fs^2 and a TOD of 1200 fs^3 . The phase shift δ between the two polarization components of the signal pulse varies between $-\pi$ to π . (b) The 1D Fourier transform of this interferogram along x -dimension. (c) In the k_x -domain, either the top or bottom sidebands were filtered out. (d) and (e) The extracted sidebands were inverse-Fourier transformed back to the x -domain. (f) and (g) The resulting product of the interfering fields is divided by the spectral field of the reference pulse to obtain the spectral field and phase difference $\phi_i^s(\omega) - \phi_i^r(\omega)$ of the corresponding polarization components of the signal and reference pulses. (h) The spectral phase difference $\delta(\omega)$ between the two polarization components of the signal pulse was calculated by taking the sum of the extracted value of $\Delta\phi(\omega)$ and $\Delta\phi^r(\omega)$. (i) The polarization ellipse parameters at central wavelength ($\lambda_0 = 800 \text{ nm}$) was retrieved by using the extracted spectral fields $E_1^s(\omega), E_2^s(\omega)$ and spectral phase difference $\delta(\omega)$

signal and reference pulses, and $\phi_i^s(\omega)$ and $\phi_i^r(\omega)$ are the spectral phases of signal and the reference pulses, respectively, where i takes on the value for two orthogonal (S and P component labelled as 1 and 2, respectively) polarization directions. At the end of reconstruction a pair of spectral phase differences $\phi_i^s(\omega) - \phi_i^r(\omega)$ is extracted, as shown in Figs. 4.4(f) and 4.4(g). Subtracting them from one another gives another phase difference $\Delta\phi(\omega)$:

$$\Delta\phi(\omega) = [\phi_2^s(\omega) - \phi_2^r(\omega)] - [\phi_1^s(\omega) - \phi_1^r(\omega)]. \quad (4.2)$$

The spectral phase difference $\Delta\phi^r(\omega)$ between the two orthogonally polarized reference pulses is

$$\Delta\phi^r(\omega) = \phi_2^r(\omega) - \phi_1^r(\omega). \quad (4.3)$$

One can define

$$\delta(\omega) = \Delta\phi(\omega) + \Delta\phi^r(\omega), \quad (4.4)$$

where $\delta(\omega)$ is the relative spectral phase $\delta(\omega)$ between the two polarization components of the signal, defined as

$$\delta(\omega) = \phi_2^s(\omega) - \phi_1^s(\omega). \quad (4.5)$$

In the experiment, $\delta(\omega)$ is obtained using Eq. (4.4) following the extraction of $\Delta\phi(\omega)$ and $\Delta\phi^r(\omega)$. The calibration measurement to determine the relative spectral phase between the two reference pulses, $\Delta\phi^r(\omega)$, is discussed in more detail in Section 4.2.3.

The complete polarization state of the signal pulse can be represented by an ellipse shown in Fig. 4.3(b), with amplitudes $E_1^s(\omega)$ and $E_2^s(\omega)$, ellipticity angle $\chi(\omega)$, and orientation angle $\psi(\omega)$. The ellipticity angle and the orientation angle are determined by

$$\sin 2\chi(\omega) = \frac{2E_1^s(\omega)E_2^s(\omega)}{E_1^s(\omega)^2 + E_2^s(\omega)^2} \sin \delta(\omega) \quad -\frac{\pi}{4} \leq \chi(\omega) \leq \frac{\pi}{4}, \quad (4.6)$$

$$\tan 2\psi(\omega) = \frac{2E_1^s(\omega)E_2^s(\omega)}{E_1^s(\omega)^2 - E_2^s(\omega)^2} \cos \delta(\omega) \quad 0 \leq \psi(\omega) \leq \pi. \quad (4.7)$$

The auxiliary angle $\alpha(\omega)$ is a quantity to indicate the relative magnitude of the amplitudes $E_1^s(\omega)$ and $E_2^s(\omega)$, and defined by

$$\tan \alpha(\omega) = \frac{E_2^s(\omega)}{E_1^s(\omega)} \quad 0 \leq \alpha(\omega) \leq \frac{\pi}{2}. \quad (4.8)$$

Finally, with the complete information describing the polarization ellipse, Stokes parameters can be obtained in terms of ellipse parameters and then used to calculate the degree of polarization of the signal pulse at any frequency (wavelength).

4.2.2 Experimental setup

Figure 4.5 shows the experimental test setup with a total of three arms used for propagating the signal beam and two reference beams to achieve angle multiplexing in the vertical (x - z) plane. The setup includes an integrated spatially resolved spectrometer consisting of a diffraction grating (GR), a cylindrical mirror (CM), and a CCD camera. The spectrometer was calibrated using a commercial calibrated spectrometer with a spectral resolution of 0.5 nm. The beams interfere at the focal plane of the cylindrical mirror, where the CCD camera is located. The half-crossing angles (θ_1 and θ_2) between the signal and two reference spectra are $\sim 0.07^\circ$ and $\sim 0.21^\circ$, respectively.

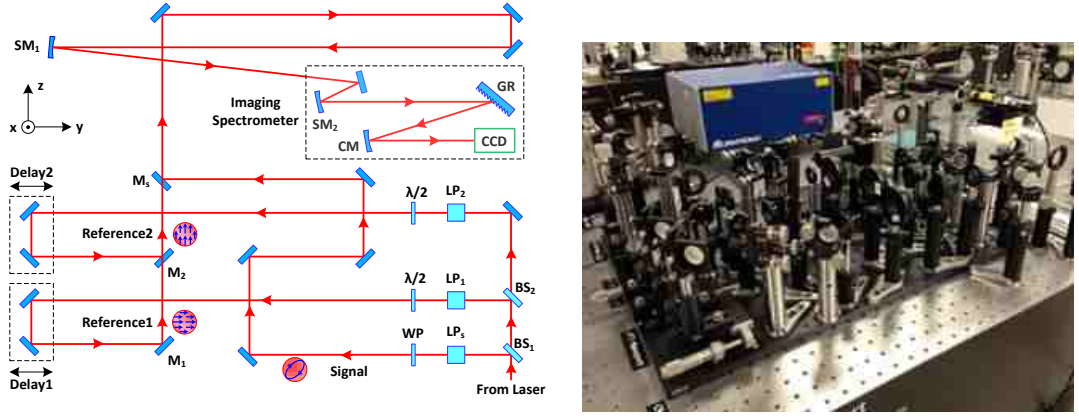


FIGURE 4.5: (a) The schematic illustrates the experimental geometry used for angle-multiplexed spatial-spectral interferometry technique. M, mirror; SM, spherical mirror. Polarization of the signal beam is rotated to an arbitrary polarization state by a zero-order wave plate ($\lambda/4$ or $\lambda/2$) after reflection from the beamsplitter BS₁. Two zero-order half-wave plates ($\lambda/2$) after two linear polarizers (LP₁ and LP₂) keep the polarization of two reference pulses highly orthogonal. Two delay lines (Delay1, Delay2) equipped with two high precision translation stages provide correct timing between signal pulse and two reference pulses. Three beams are vertically multiplexed at zero delay and collimated before being spectrally dispersed on the CCD using the grating (GR) and the cylindrical mirror (CM). (b) Photo for the device.

A diffraction grating with a 600 mm^{-1} groove density and a cylindrical mirror with a focal length of 50 mm were used to accommodate a bandwidth of $\sim 70 \text{ nm}$ over the CCD width. The CCD has a resolution of 1280×960 pixels with a pixel size of $3.75 \mu\text{m}$ and 12-bit digital output. The laser source for the experiment was a mode-locked Ti:sapphire oscillator with a center wavelength of 800 nm and FWHM bandwidth of $\sim 30 \text{ nm}$. The laser beam was split into three by two beam splitters; the first reflected beam served as the signal and the other two as references. The signal beam is rotated to an arbitrary polarization state by a zero-order wave plate ($\lambda/4$ or $\lambda/2$) and subsequently interferes with two orthogonal reference beams at zero delay. The spectral intensities of all three beams are set to be approximately equal to each other during the experiment in order to achieve a high fringe contrast in their corresponding interferograms and to reduce errors in the reconstruction process. The interferogram is recorded with a Lab-View software controlled data acquisition system and subsequently analyzed using the described reconstruction method.

4.2.3 System calibration

As pointed out in previous studies of other interferometric techniques [22, 23], accurate calibration of the system is paramount. The setup should further exhibit low jitter and low calibration drift on the time scale of the measurement. Since this approach involves two reference beams and a signal beam, any non-zero temporal overlap

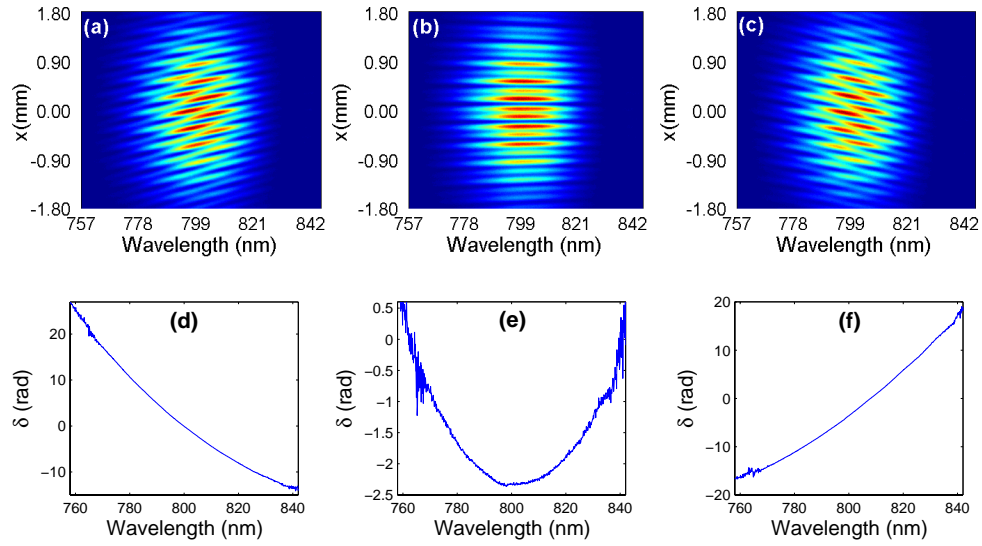


FIGURE 4.6: Experimental interferograms with three different temporal delays τ between the two reference pulses: (a) $\tau < 0$, (b) $\tau = 0$, (c) $\tau > 0$. The extracted spectral phase shift $\delta(\omega)$ corresponding to respective temporal delays of: (d) $\tau < 0$, (e) $\tau = 0$, (f) $\tau > 0$.

of the three pulses could introduce error in the measurement of $\delta(\omega)$. A non-zero delay τ between pulses results in the tilt of interference fringes along the horizontal axis of the CCD, as shown in Fig. 4.6. In the experiment, a signal beam linearly polarized at 45° was used and subsequently interfered with two orthogonal reference beams. One of the delay stages in a reference beamline was deliberately moved by equal distances in opposite directions from its reference, zero-delay ($\tau = 0$) position, while the other delay stage was kept at a zero-delay position with respect to the signal pulse. The corresponding interferograms for these cases were subsequently recorded and compared them, as shown in Figs. 4.6(a)-(c). The spectral phase shifts $\delta(\omega)$ that correspond to those cases are extracted using Eq. (4.4) and are shown in Figs. 4.6(d)-(f). Figure 4.6(e) shows a small parabolic phase which is due to small chirp caused by a beam splitter in the system. Figures 4.6(d) and 4.6(f) show curves that are similar to linear spectral phase which is introduced by a temporal delay in one of the reference arms.

The calibration first involves setting the zero delay position so that the fringes are horizontal. Second, the signal arm is blocked and the polarization of one reference arm is rotated to match the other, so that the system is reduced to a standard two-arm interferometer. Measuring the spectral phase difference between the two reference arms and subtracting out this phase from all subsequent measurements eliminates the spectral phase introduced by the setup itself.

In practice, a small change of the optical path lengths in the three arms of the interferometer can be manifested both as a fast jitter and a slow phase drift. The main causes of the jitter and drift are mechanical vibrations, air current-induced and

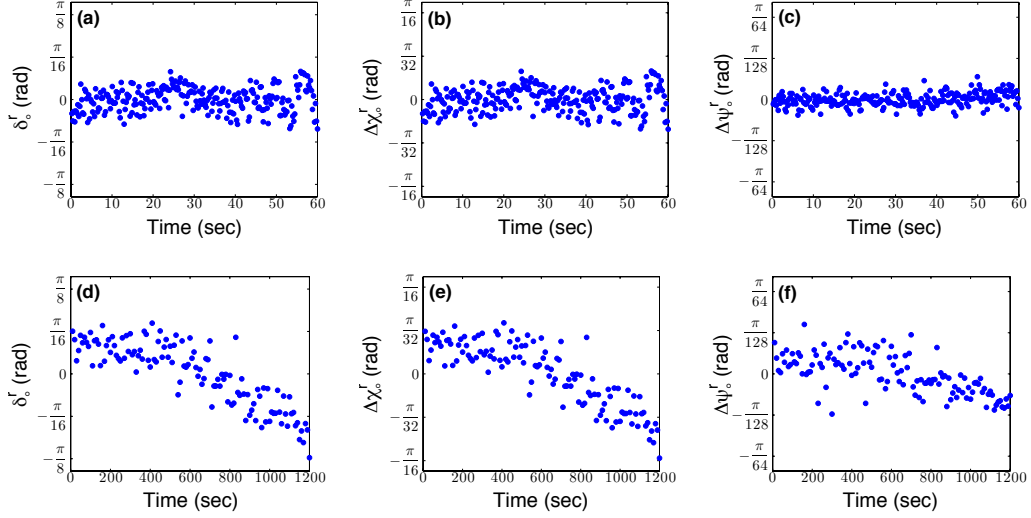


FIGURE 4.7: Effect of measured fast phase jitter: (a) phase drift corresponding to the relative phase difference between the two reference arms; drifts in corresponding polarization ellipse parameters, such as (b) ellipticity angle $\Delta\chi_o^r$ and (c) orientation angle $\Delta\psi_o^r$. The corresponding drifts for those quantities is also measured over longer time scales and shown in (d)–(f).

temperature-dependent refractive index changes and mechanical expansion, and the finite beam pointing stability. An acrylic box was built around the set-up and a tight isolation of the system against the air currents in the lab has been established. The relative spectral phase $\Delta\phi^r(\omega)$ between the two reference arms is needed for obtaining the polarization measurement of the signal pulse. In the experiment, both polarizations are rotated to be the same and the signal beam is blocked; then the interferograms corresponding to two reference pulses were subsequently obtained. The resulting reconstruction of the interferogram yields $\Delta\phi^r(\omega)$ and is used in Eq. (4.4) to extract the relative spectral phase shift $\delta(\omega)$ of the two polarization components of the signal pulse. The drift of $\Delta\phi^r(\omega)$ is monitored on short and longer time scales by continuous recording of the interferograms corresponding to two reference arms. Figure 4.7(a) shows the mean-value subtracted zeroth-order spectral phase $\delta_o^r = \Delta\phi^r(\lambda_o)$ that was monitored over one-minute period. In the measurements, the RMS variation of δ_o^r was 0.06 rad over one minute, while the RMS variations in corresponding ellipse parameters $\Delta\chi_o^r$ and $\Delta\psi_o^r$ were 0.03 rad and 3.95 mrad, respectively (Figs. 4.7(b)–(c)). The corresponding RMS delay fluctuations (δ_o^r/ω_o) for this case are calculated to be 0.02 fs. Figure 4.7(d) shows the mean value subtracted zeroth-order spectral phase $\delta_o^r = \Delta\phi^r(\lambda_o)$ that was monitored over a longer, 20-minute period. In the measurements, the variation of δ_o^r was ~ 0.6 rad over 20 minutes, (Figs. 4.7(e)–(f)). The corresponding delay drift for this case is calculated to be ~ 0.25 fs. This drift does not significantly affect the higher orders of the spectral phase (such as group delay dispersion and third-order dispersion), as previously pointed out in related spectral interferometry measurements [22].

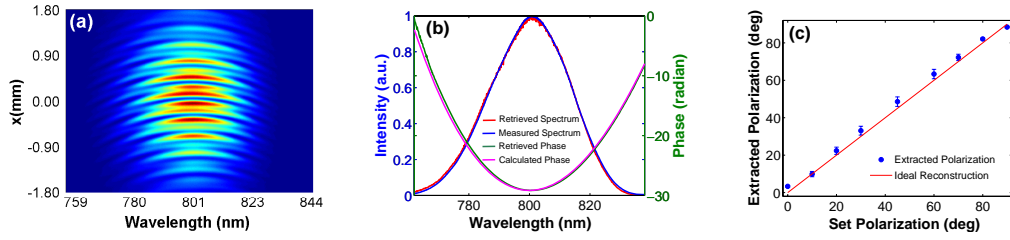


FIGURE 4.8: (a) Experimental spectral interferogram of a signal pulse linearly polarized at 45° passing through SF11 glass rod and interfering with two orthogonally polarized reference pulses. (b) The retrieved spectrum (red) is compared to the measured spectrum (blue). The extracted net spectral phase (green) introduced by the SF11 glass rod is also compared to the calculated phase (magenta) due to material dispersion. (c) Extracted polarization angles for several tested polarization states are plotted against the set linear polarization angle of the signal.

In our experiments, a measurement is performed over a relatively short period (less than a minute) following the calibration of the phase between the two reference beams. As a result, the effect of slow drift is not significant and only the fast jitter affects the accuracy of the measurement. If a more conservative, peak-to-peak criterion is used to quantify the fast phase jitter shown in Fig. 4.7(a) and can be slightly overestimated as $\pi/16$, this would be consistent with a fast time jitter of 0.085 fs. Thus with this level of short-time jitter one would expect to be able to perform measurements with $\sim 10\%$ accuracy over bandwidths > 300 nm, provided that the measurements are performed within a time period of ~ 5 minutes following the calibration.

4.2.4 Measurement of a linearly polarized pulse with dispersion

The spectral phase of the signal beam is measured by a two-step procedure. First, the interferogram produced by the setup with no additional dispersion introduced is recorded and the corresponding spectral phase shift is retrieved. Second, the interferogram with additional dispersion introduced into the signal beam is recorded. The two measured spectral phases are subtracted to obtain the dispersion introduced into the signal beam. A typical experimental interferogram of a linearly polarized signal pulse with dispersion introduced is shown in Fig. 4.8(a).

To test the accuracy of this technique, group delay dispersion (GDD) of a 2-cm thick SF11 glass rod was measured. Figure 4.8(b) shows the retrieved spectral intensity and net spectral phase corresponding to insertion of the SF11 rod. The spectra of the two polarization components were experimentally determined to be identical. The retrieved spectrum is also in close agreement with the spectrum separately measured using the same spectrometer. The GDD was calculated by fitting the extracted spectral phase to a quadratic function in frequency, resulting in an extracted value of $1952 \text{ fs}^2/\text{cm}$ which is in reasonable agreement (3% error) with the GDD calculated by the known Sellmeier equations for SF11 ($1897 \text{ fs}^2/\text{cm}$). A half-wave plate in the signal arm was

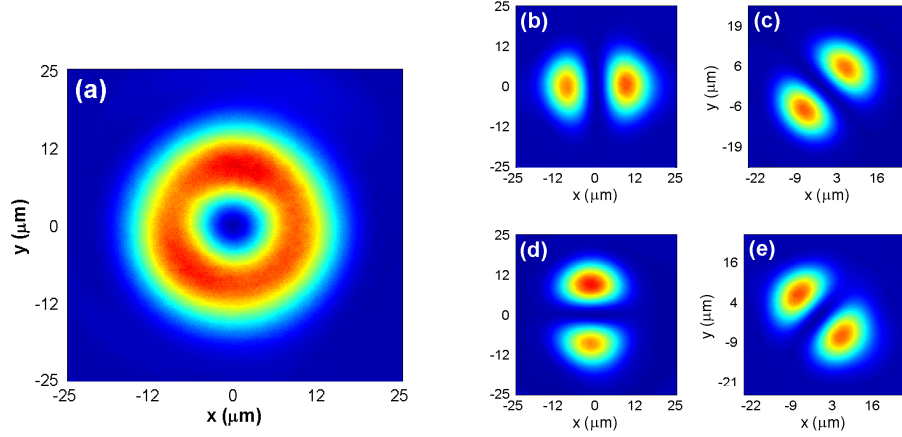


FIGURE 4.9: (a) Measured far-field image of a radially polarized beam. Also shown is the far-field image of the same beam after passing through a rotating linear analyzer set at (b) 0° , (c) 45° , (d) 90° , and (e) 135° .

used to set the linear polarization to a known polarization angle; this angle has been retrieved by analyzing the corresponding interferogram. The extracted and set linear polarization angles are shown in Fig. 4.8(c) and on average they agree at a level of 98%. The extracted polarization angles in Fig. 4.8(c) are the statistical average of 10 successive measurements for each corresponding polarization angle and the error bars represent one statistical standard deviation.

4.2.5 Radially polarized pulse measurement

The ability to perform characterization of beams with spatially varying polarization is demonstrated on an example of a radially polarized pulse. The radially polarized state was generated by sending a linearly polarized laser beam into a liquid-crystal polarization converter that operates on the basis of a twisted nematic effect [20]. When the orientation of liquid-crystal molecules of the converter with respect to the incident beam is set properly by the external voltage, the beam experiences a rotation of its polarization direction by the twist angle. This rotation is a function of the angular position with respect to the crystal axis. Figure 4.9(a) shows the measured far-field image of the radially polarized beam produced in this way, while the Figs. 4.9(b)-(e) show the same far field image after the radially polarized beam is passed through a linear polarizer oriented at various angles.

The measurement of relative spectral phase and polarization state of a radially polarized beam can be performed by sampling the output beam at different spatial positions. The insets in Fig. 4.10(c)-(d) indicate the location of the two sampling positions used for this demonstration: vertical bottom (1) and corner left (2). In this experiment, a calibrated iris with the aperture size of 1.5 mm was mounted on an x-y translation stage and used to sample the beam. The sampled beamlet in the signal arm of the

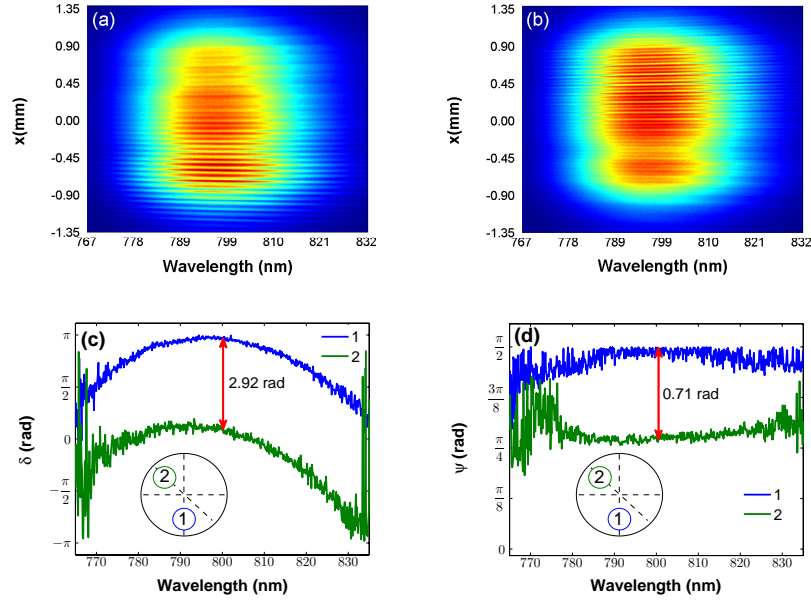


FIGURE 4.10: Two interferograms were taken with two reference beams interfere with the sampled signal beam taken at point 1 (a) and point 2 (b), respectively. (c) Extracted relative spectral phases corresponding to two sampling points (1 and 2) were compared. The inset indicates the sampling position in the beam. (d) The ellipse orientation angles ψ that represent sampled points (1 and 2) were calculated and compared.

interferometer interferes with two orthogonally polarized reference beams. The sizes of two reference beams are set to be larger than the sampled beamlet, so that the signal beamlets are overlapped with both reference beams, producing interferograms that are always be contained within the CCD field of view. Figures 4.10(a) and (b) show the interferograms corresponding to the sampling positions (1) and (2), respectively.

The extracted relative spectral phase corresponding to the sampling positions (1) and (2) is shown in Fig. 4.10(c). The difference of the relative phase between those two points at the central wavelength ($\lambda_0 = 800$ nm) is 2.92 rad, close to the expected relative phase of 3.14 rad. Their reconstructed group delay dispersion are also very similar, differing by $\sim 9\%$. The polarization ellipse orientation angle ψ for the two sampled positions is shown in Fig. 4.10(d). The difference in absolute values of ψ at central wavelength ($\lambda_0 = 800$ nm) is 0.71 rad, which is close to the expected value of $\pi/4$. The quality of the reconstruction of the spectral phase and ellipse orientation angles is reduced further from the central wavelength, mainly due to reduced fringe contrast. It is important to note that since the polarization continuously varies across the beam, the finite sampling size results in an ensemble of polarizations at the sample location being reconstructed as an average. Making the sampling size smaller could help reconstruct the local polarization with greater fidelity, at the expense of the reconstruction time needed to collect and analyze a greater number of interferograms, and is ultimately limited by the stability of the interferometer.

4.2.6 Summary of the results

In summary, a simple technique capable of simultaneous reconstruction of the relative spectral phase and the polarization state has been proposed and experimentally demonstrated. The use of angle multiplexing with two orthogonally polarized reference pulses is a convenient approach to achieve this simultaneous reconstruction. The Angle-multiplexed SSI technique has the capability to measure the relative spectral phase and polarization state of two orthogonal polarization components of an arbitrary polarized signal pulse independently and simultaneously. Similar to other interferometric techniques, the developed technique is limited by the interferometric phase drift, necessitating a calibration prior to each data taking. However, it is shown experimentally on the example of a beam with complex spatially varying polarization, a radially polarized pulse, that sufficient stability can be practically achieved, resulting in acceptable accuracies of the reconstructed spectral phase and spatially varying polarization. The slow drift in the spectral phase measurement indicates that a calibration is needed approximately every 5 minutes in this set-up in standard experimental conditions. To reduce the time between the calibration and measurement even further, a fast shutter could be placed in the signal arm of the set-up to block the signal beam while an electro-optic modulator can be placed in one of the reference arms in order to establish a fast flipping of the polarization. With the addition of this two devices, the recording of the calibration data would become hassle-free, and data collection could resume in a rather quick way so that the effects of drift would be reduced further. Shot-to-shot variations could be reduced further by improving the mechanical stability and the beam pointing stability (while the latter could also be simultaneously measured to reject measurements exhibiting too large pointing errors). More complex shaped pulses with spatially varying polarization can be characterized by the use of this technique.

Chapter 5

Conclusion and perspective

5.1 Discussion of Results

The powerful electromagnetic field associated with a focused fs laser pulse motivates the development of methods that use the laser field to provide a high acceleration gradient for electrons. In this project, the DLA scheme in which electrons are accelerated by the axial field of a focused, radially polarized laser pulse has been studied both by simulation and experiment. By guiding the radially polarized laser pulse in a density-modulated plasma waveguide, a large axial acceleration gradient (on the order of tens of GV/m) can be realized over an extended distance. In this way, DLA may provide an energy gain >100 MeV at the waveguide output, even when a moderate laser peak power ($< \text{TW}$) is used. The plasma waveguide extends the acceleration distance and the density modulation provides the quasi-phase matching (QPM) condition to improve the DLA efficiency. Through the simulations presented in Chapter 2, one of the major objectives of this research has been to develop a significantly improved understanding of the characteristics and limitations of the DLA technique. On the experimental side, an all-optical method for fabrication of density-modulated plasma structures was demonstrated. Results presented in Chapter 3 serve as a proof-of-principle foundation for fabricating density-modulated plasma waveguides using this method. In addition, micrometer-scale supersonic de Laval slit jet nozzles were designed and produced by additive manufacturing techniques with dimensions that could not be readily obtained using traditional subtractive manufacturing techniques. Lastly, a new interferometric technique that allows the characterization of radially polarized laser pulses was developed and described in Chapter 4. This is the first technique capable of characterizing the two orthogonal linearly polarized field components of a radially polarized pulse from a single measurement.

5.1.1 Injection of electrons for DLA

The initial injection energy is an important parameter that affects the DLA overall efficiency. When electrons with low initial energies $\lesssim 20$ MeV are injected, results described in Sec. 2.1.2 show that a positively chirped density modulation of the waveguide structure is required for achieving the optimal QPM condition (*cf.* Fig. 2.2). The modulation period of the axial structure has to be varied according to the rapid change of dephasing length in low-energy regions ($\lesssim 20$ MeV, *cf.* Fig. 2.1). However, even when an optimal axial structure has been applied, electrons injected with a higher initial energy ($\gtrsim 20$ MeV) are preferred in order to obtain larger axial and radial acceleration regions (*cf.* Fig. 2.4). At a low initial energy (a few MeV), electrons injected in a suboptimal phase or at a greater radial position cannot be accelerated to the required energies for consistently meeting the QPM condition along the propagation distance. Therefore, QPM of DLA is predicted to have higher acceleration efficiency if the electron bunches can be pre-accelerated to tens of MeV before injection.

Since a laser pulse propagates slower than relativistic bunch electrons in a plasma waveguide, the temporal walk-off effect among the DLA process has to be carefully considered for maximization of the energy gain. As described in Sec. 2.1.2 (*cf.* Eqs. 2.4 and 2.9), electrons injected at the trailing edge of the laser pulse experience a symmetrically distributed acceleration (laser field) envelope with respect to the waveguide dimension and acquire a maximum energy. However, the walk-off effect can limit the effective acceleration distance and lower the efficiency, especially when ultrashort (< 10 fs) laser pulses are used (*cf.* Fig. 2.3). Therefore, a longer pulse duration is more desirable for higher energy gain in DLA when the acceleration length is limited by the temporal walk-off. On the other hand, when a long pulse is used for DLA such that the effective acceleration distance is limited by the waveguide length L_{wg} , the energy gain scales as $\Delta T \propto q_e E_{x,max} L_{wg}$ and a shorter pulse duration is desirable.

5.1.2 Maintenance of the transverse bunch properties

As discussed in Sec. 2.2.2, the hollow distribution of the radially polarized beam results in a ponderomotive force that pushes the background plasma electrons to concentrate at center (*cf.* Fig. 2.6(a)), from which a transverse electrostatic force that can diverge the bunch electrons is generated. Reducing the injection delay can lead the bunch head to experience a lower on-axis plasma electron density (*cf.* Fig. 2.6(b)), so that the corresponding defocusing force toward the bunch electrons decreases as well. Therefore, when a short bunch, with a length much shorter than $\lambda_p/4$, is injected, the final bunch collimation can be improved with a smaller injection delay (*cf.* Fig. 2.8). In addition, increasing the bunch length to the scale of $\lambda_p/4$ helps to improve the collimation properties because of the enhanced focusing force from the background ions (*cf.* Figs. 2.9

and 2.10). DLA efficiency is reduced when a bunch with a greater transverse size is injected (*cf.* Fig. 2.12).

5.1.3 Improvement of the heating efficiency of plasmas for plasma waveguide production

An important challenge for effective DLA is realizing density-modulated plasma waveguides that can provide the QPM condition for efficient acceleration. By using the ignitor-heater scheme in the 90° geometry, Ar plasma channels could be fabricated with an apparent axial density structure when an spatially modulated ignitor is introduced (*cf.* Fig. 3.13). Results presented in Sec. 3.2.1 show that it is important to prevent the ionization of gas atoms by the heater itself; otherwise, the heating of plasma by the inverse bremsstrahlung mechanism is significantly inhibited (*cf.* Fig. 3.9). The limited heating efficiency of the plasma channel also resulted in significant variations of the length and plasma density distribution among the produced plasma channels (*cf.* Fig. 3.10). The heating efficiency of plasma has to be improved, so that a well-established plasma density profile [11, 13, 15, 16] with a high on-axis density $> 10^{19} \text{ cm}^{-3}$ and a density barrier $> 5 \times 10^{18} \text{ cm}^{-3}$, which fulfills the guiding condition for the laser pulse, can be realized. Using a lens with a short focal length (*e.g.*, $f = 5 \text{ cm}$) for producing a tighter focusing of the heater will be helpful to mitigate the unfavorable ionization of gas by the heater; as a result, the heating efficiency via the inverse bremsstrahlung process can be improved. The other solution can be realized by combining an intensity-modulated, transversely projected ignitor with a heater line focus made by an axicon; this may be a more practical configuration for producing density-modulated plasma waveguides.

5.2 Perspective: Future development of DLA experiments

Figure 5.1 illustrates the experimental set-up proposed to demonstrate DLA in the future. The high-power, radially polarized pump pulse for driving DLA can be produced by transmitting a laser pulse with a conventional polarization (linear or circular polarization) through a radial polarization converter. This converter can be realized using a liquid crystal cell that is introduced in Sec. 4.1, or from a segmented phase shifter made by cutting and angularly arranging standard waveplates [24]. One major future task is to realize the guiding of radially laser pulses in density-modulated plasma waveguides. The density-modulated plasma waveguide can be fabricated by introducing an intensity-modulated ignitor and a subsequent heater line focus (produced with an axicon) into the gas target. When plasma waveguides are well fabricated in the system, a radially polarized pump pulse can be coupled into a plasma waveguide to test the guided propagation. It is noted that larger axial and radial acceleration regions exist

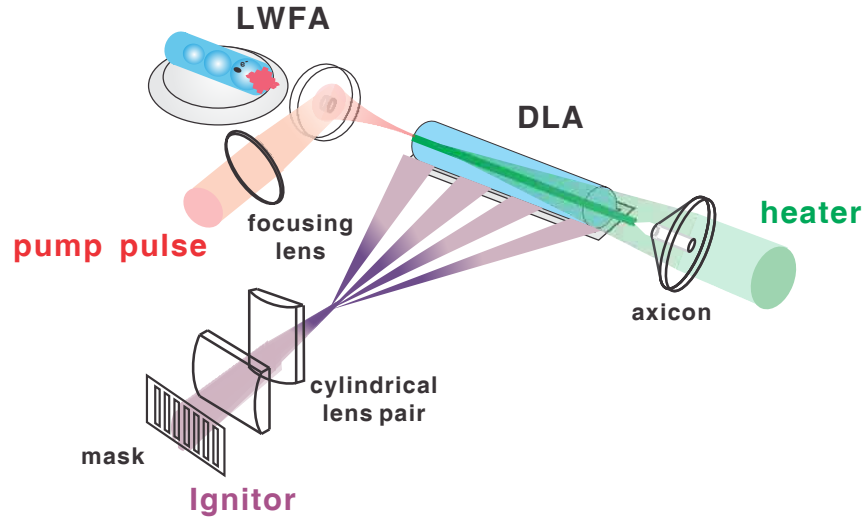


FIGURE 5.1: Illustration of a possible future DLA configuration. An electron bunch from the output of a LWFA is injected into a density-modulated plasma waveguide for subsequent DLA.

in DLA when electrons are injected with a higher initial energy; in this way a higher overall acceleration efficiency can be realized. Therefore, pre-accelerated electrons, with an initial energy of tens of MeV (for example, from the output of a LWFA) can be injected in a density-modulated plasma waveguide for the synchronized co-propagation with the DLA driving pulse. In this way, an all laser-based acceleration scheme which integrates the injection of electron bunches from a LWFA into a plasma waveguide for the subsequent DLA to higher energies can be accomplished.

Bibliography

- [1] P. Serafim, P. Sprangle, and B. Hafizi, “Optical guiding of a radially polarized laser beam for inverse cherenkov acceleration in a plasma channel,” *IEEE Trans. Plasma Sci.*, vol. 28, p. 1155, 2000.
- [2] M.-W. Lin, Y.-M. Chen, C.-H. Pai, C.-C. Kuo, K.-H. Lee, J. Wang, S.-Y. Chen, and J.-Y. Lin, “Programmable fabrication of spatial structures in a gas jet by laser machining with a spatial light modulator,” *Phys. Plasmas*, vol. 13, p. 110701, 2006.
- [3] Y. I. Salamin, “Accurate fields of a radially polarized gaussian laser beam,” *New J. Phys.*, vol. 8, p. 133, 2006.
- [4] A. G. York, H. M. Milchberg, J. P. Palastro, and T. M. Antonsen, “Direct acceleration of electrons in a corrugated plasma waveguide,” *Phys. Rev. Lett.*, vol. 100, p. 195001, 2008.
- [5] J. P. Palastro, T. M. Antonsen, S. Morshed, A. York, and H. M. Milchberg, “Pulse propagation and electron acceleration in a corrugated plasma channel,” *Phys. Rev. E*, vol. 77, p. 036405, 2008.
- [6] C. Nieter and J. R. Cary, “Vorpall: a versatile plasma simulation code,” *J. Comput. Phys.*, vol. 196, p. 448, 2004.
- [7] S. Humphries, *Charged particle beams*. New York: Wiley, 1990.
- [8] S. J. Yoon, J. P. Palastro, D. Gordon, T. M. Antonsen, and H. M. Milchberg, “Quasi-phase-matched acceleration of electrons in a corrugated plasma channel,” *Phys. Rev. ST Accel. Beams*, vol. 15, p. 081305, 2012.
- [9] N. Barov and J. B. Rosenzweig, “Propagation of short electron pulses in underdense plasmas,” *Phys. Rev. E*, vol. 49, p. 4407, 1994.
- [10] H. L. Buchanan, “Electron beam propagation in the ion focused regime,” *Phys. Fluids*, vol. 30, p. 221, 1987.

- [11] B. D. Layer, A. York, T. M. Antonsen, S. Varma, Y.-H. Chen, Y. Leng, and H. M. Milchberg, "Ultrahigh-intensity optical slow-wave structure," *Phys. Rev. Lett.*, vol. 99, p. 035001, 2007.
- [12] B. Layer, A. York, S. Varma, Y.-H. Chen, and H. Milchberg, "Periodic index-modulated plasma waveguide," *Opt. Express*, vol. 17, p. 4263, 2009.
- [13] T.-S. Hung, Y.-C. Ho, Y.-L. Chang, S.-J. Wong, H.-H. Chu, J.-Y. Lin, J. Wang, and S.-Y. Chen, "Programmably structured plasma waveguide for development of table-top photon and particle sources," *Phys. Plasmas*, vol. 19, p. 063109, 2012.
- [14] P. Volfbeyn, E. Esarey, and W. P. Leemans, "Guiding of laser pulse in plasma channels created by the ignitor heater technique," *Phys. Plasmas*, vol. 6, p. 2269, 1999.
- [15] Y.-C. Ho, T.-S. Hung, J.-G. Jhou, H. Qayyum, W.-H. Chen, H.-H. Chu, J.-Y. Lin, J. Wang, and S.-Y. Chen, "Induction of electron injection and betatron oscillation in a plasmawaveguide based laser wakefield accelerator by modification of waveguide structure," *Phys. Plasmas*, vol. 20, p. 083104, 2013.
- [16] Y.-F. Xiao, H.-H. Chu, H.-E. Tsai, C.-H. Lee, J.-Y. Lin, J. Wang, and S.-Y. Chen, "Efficient generation of extended plasma waveguides with the axicon ignitor-heater scheme," *Phys. Plasmas*, vol. 11, p. L21, 2004.
- [17] G. H. Oosthuizen, *Introduction to Compressible Fluid Flow*, 2nd ed. Boca Raton, FL: CRC Press, 2014.
- [18] Q. Zhan, "Cylindrical vector beams : from mathematical concepts to applications," *Adv. Opt. Photon.*, vol. 1, p. 1, 2009.
- [19] G. Machavariani, Y. Lumer, I. Moshe, A. Meir, and S. Jackel, "Efficient extracavity generation of radially and azimuthally polarized beams," *Opt. Lett.*, vol. 32, p. 1468, 2007.
- [20] M. Stalder and M. Schadt, "Linearly polarized light with axial symmetry generated by liquid-crystal polarization converters," *Opt. Lett.*, vol. 21, p. 1948, 1996.
- [21] K. J. Moh, X.-C. Yuan, J. Bu, D. K. Y. Low, and R. E. Burge, "Direct noninterference cylindrical vector beam generation applied in the femtosecond regime," *Appl. Phys. Lett.*, vol. 89, p. 251114, 2006.
- [22] P. Bowlan, P. Gabolde, A. Shreenath, K. McGresham, and R. Trebino, "Crossed-beam spectral interferometry: a simple, high-spectral-resolution method for completely characterizing complex ultrashort pulses in real time," *Opt. Express*, vol. 14, p. 11892, 2006.

-
- [23] C. Iaconis and I. A. Walmsley, “Self-referencing spectral interferometry for measuring ultrashort optical pulses,” *IEEE J. Quantum Electron.*, vol. 35, p. 501, 1999.
 - [24] S. Carbajo, E. Granados, D. Schimpf, A. Sell, K.-H. Hong, J. Moses, and F. X. Kärtner, “Efficient generation of ultra-intense few-cycle radially polarized laser pulses,” *Opt. Lett.*, vol. 39, p. 2487, 2014.

Executive Summary

DTRA Final Technical Report
HDTRA1-11-1-0009

All-Optical Quasi-Phase Matching for for Laser Electron Acceleration

PROJECT OBJECTIVE

Sensing of shielded fissile materials at long range in field applications is critically dependent on the development of compact, low-weight, and low-power particle accelerators. Direct laser acceleration of electrons (DLA), in which electrons are accelerated by the axial component of the electric field of a focused, radially polarized laser pulse, has the potential to meet this requirement. Field gradients on the order of tens of GV/m are expected from a moderate laser peak power below TW level, available from compact, high repetition rate laser systems. Through a set of detailed simulations and experiments, the objective of this project was to contribute to the scientific basis for implementation of this laser acceleration technique. To this end, several important scientific and engineering challenges of this approach were investigated.

BACKGROUND

Two significant challenges associated with implementation of DLA include the realization of guided propagation of intense laser pulses over extended distances and the phase matching (QPM) between the propagating electrons and laser pulses. Optical guiding using a preformed plasma waveguide has a potential to extend the accelerating distance beyond the usual Rayleigh range. Furthermore, similar to the ubiquitous quasi-phase matching in nonlinear optics, corrugated plasma waveguides exhibiting axially periodic plasma density modulation could be used to quasi-phase match the laser and electron pulses. A net acceleration can be produced by breaking the symmetry between acceleration and deceleration phases. As the number of QPM periods increases, it is possible for electrons to acquire energy above 100 MeV even for modest laser peak powers (<1 TW).

This work had two underlying thrusts: (1) develop a detailed model involving novel methods for all-optical control of QPM in DLA, and (2) conduct critical experiments to validate the key assumptions and predictions of this model, with significant impact on a broader set of promising laser acceleration schemes. The work was proposed to be conducted in two phases, corresponding to the Base and Option Period. In Phase I of this work, the necessary modeling and experimental work was conducted to demonstrate the feasibility of all-optical QPM control. In the proposed Phase II, it was planned to complete the integrated experimental demonstration of all-optically controlled DLA with laser-injected electrons. Major tasks of this project are summarized as follows:

Phase I

- Task 1: Model propagation of femtosecond radially polarized laser pulses in plasma waveguides.
- Task 2: Design of plasma channel shaping system.
- Task 3: Demonstrate an all-optical method for tailoring plasma waveguides.
- Task 4: Develop new spatially and temporally resolved diagnostics.
- Task 5: Generate radially polarized femtosecond pulses for use in DLA.
- Task 6: Characterize propagation of femtosecond radially polarized pulses in plasma waveguides.

Phase II

- Task 7: Design and construct a laser-based electron injection system.
- Task 8: Integrated demonstration of DLA on laser-injected electrons.

The majority of the goals of Phase I, concluding the Base Period of the Project, have been accomplished. The personnel involved in this project were:

- Igor Jovanovic (PI)
Professor of Nuclear Engineering, Penn State
- Abdurahim Rakhman (Tasks 2, 4 and 5) 2011-2013
Postdoctoral fellow, Nuclear Engineering, Penn State
- Ming-wei Lin (Tasks 1-6) 2010-2015
Ph.D. student, Nuclear Engineering, Penn State
- Bryan Morgan (Task 2) 2014-2015
M.S. student, Nuclear Engineering, Penn State
- Daniel Abercrombie (Task 2) 2012-2014
undergraduate student, Nuclear Engineering, Penn State
- Bilan Yang (Task 4) 2014 summer student internship
undergraduate student, Mechanical Engineering, Rice University

PROCESS

- To accomplish Task 1, a test particle model was developed to simulate the trajectory and momentum changes of electrons when interacting with laser field in DLA and was used to optimize DLA designs for the axial density structure of the plasma channels. Next, 3-D plasma particle-in-cell (PIC) simulations of DLA were conducted to resolve the relationship between the initial bunch parameters (injection delay, bunch length and bunch size) with the variation of bunch energy spectrum, emittance, and density (or electron particle) distribution throughout the DLA process.
- To accomplish Tasks 2, 3 and 6, an all-optical method, based on the ignitor-heater scheme for plasma waveguide fabrication, was designed and experimentally implemented to fabricate the density-modulated plasma waveguides. Experimental results from fabricating plasma channels in Ar were obtained and analyzed. Micrometer-scale supersonic gas jets were designed, simulated and produced via additive manufacturing techniques in titanium and aluminum. Surface quality of the nozzles was evaluated with X-ray computed tomography.

- To accomplish Tasks 4 and 5, femtosecond, radially polarized laser pulses with millijoule-level pulse energies were produced using a liquid crystal converter. A novel angle-multiplexed spatial-spectral interferometric technique, capable of simultaneously reconstructing the phase and polarization of a laser pulse, was developed and experimentally implemented. Measurement of the relative spectral phase and the spatially variable polarization state of a radially polarized pulse was also demonstrated.

IMPORTANT FINDINGS AND CONCLUSIONS

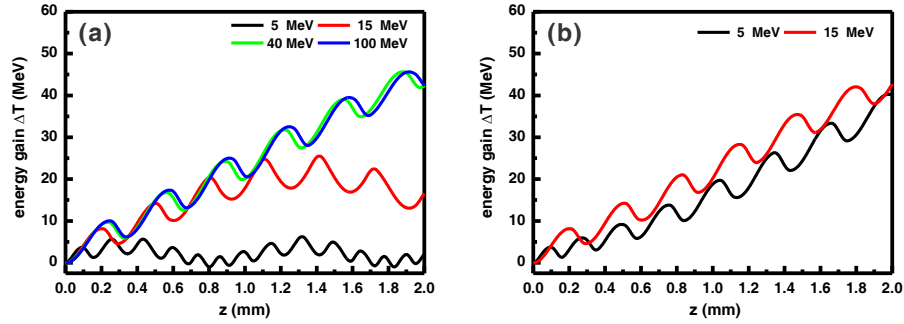


FIGURE 2: Dependence of electron energy gain ΔT on propagation distance z for electrons with $T_0 = 5, 15, 40$ and 100 MeV in plasma waveguides with (a) constant and (b) chirped, aperiodic density modulation (only applied for $T_0 = 5$ and 15 MeV).

The developed test particle mode was applied to study the optimal plasma structure for realizing efficient QPM of DLA. Figure 2(a) shows the dependence of electron energy gain ΔT on axial position z in waveguides with constant density modulation periods according to dephasing lengths. The results indicate that quasi-phase matched DLA by constant density modulation can only be achieved for electrons having higher initial kinetic energies ($T_0 = 40$ and 100 MeV). Using the same parameters as in Fig. 2(a) for low electron initial energies $T_0 = 5$ and 15 MeV but varying plasma structure lengths, quasi-phase matched DLA by aperiodic density modulation is illustrated in Fig. 2(b). It is important to carefully tune the plasma structure lengths in the first few sections so that electrons can continue to reach the acceleration phase. The modulation lengths are also increased with the increase in electron energy and gradually converge to DLA dephasing lengths at higher electron energies. Results show that aperiodic modulation of corrugated plasma waveguides are required for DLA with low electron kinetic energies ($\lesssim 20$ MeV). In this region, DLA dephasing length changes rapidly with the increased electron energy and the plasma structure should be varied accordingly so that electrons can continue to reach the acceleration phase along the propagation distance. The periodicity of the density modulation will converge to constants as electrons are accelerated to high energies ($\gtrsim 40$ MeV). The simulation work provide the proof-of-principle for quasi-phase matched DLA with corrugated waveguides.

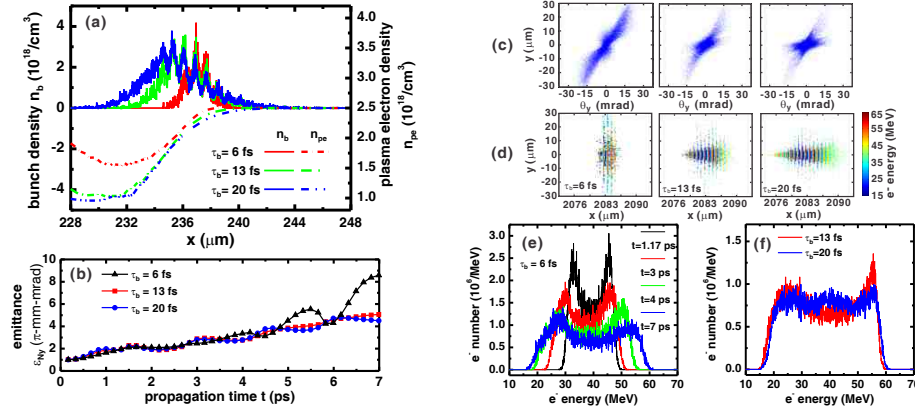


FIGURE 3: For bunches with durations $\tau_b = 6$ fs, 13 fs and 20 fs: (a) the on-axis bunch density n_b and plasma electron density n_{pe} at $t = 0.832$ ps; (b) emittance $\epsilon_{N,y}$ as a function of propagation time t ; final (c) trace space and (d) particle distributions. (e) Variation of the energy spectrum throughout the DLA for the 6-fs bunch. (f) Final energy spectra for bunches with $\tau_b = 13$ fs and 20 fs.

The PIC mode was applied to study DLA of variable-length electron bunches in plasma waveguides. Figure 3(a) shows the comparison of on-axis plasma density $n_{pe}(x)$ when bunches with durations $\tau_b = 6$ fs, 13 fs and 20 fs propagate in the first waveguide section. Since the variation of $n_{pe}(x)$ is of order $\lambda_p/4 \simeq 5.3 \mu\text{m}$ near the trailing edge, increased durations of the electron bunch of $\tau_b = 13$ fs and 20 fs and the corresponding bunch lengths $L_b = 3.9 \mu\text{m}$ and $6 \mu\text{m}$ are closer to the value of $\lambda_p/4$, such that more bunch electrons can be confined in the created ion channel. Consequently, the collimation and emittance $\epsilon_{N,y}$ of the DLA-accelerated bunch, as shown in Fig. 3(b), can be considerably improved by increasing the bunch duration. The reduced final emittance $\epsilon_{N,y}$ for $\tau_b = 13$ fs and 20 fs is consistent with the θ_y - y trace space results shown in Fig. 3(c), in which electrons are more concentrated near the waveguide center because of the enhanced ion-focusing effect. The final electron particle distributions shown in Fig. 3(d) reveal the effect of the electron injection phase on the acceleration or deceleration process in DLA. As illustrated in Fig. 3(e), the energy spectrum gradually broadens when it propagates throughout the plasma waveguide. Particle distributions for bunches of $\tau_b = 13$ fs and 20 fs in Fig. 3(d) also show that more electrons at the leading and trailing edges cannot be effectively accelerated/decelerated when the bunch duration becomes comparable to the laser pulse duration (20 fs), such that the final energy spectra in Fig. 3(f) become more uniform with a increased bunch duration τ_b . Results show the injection of an electron bunch with a long bunch length is preferred for maintaining the favorable bunch transverse properties in DLA in a plasma waveguide. Under those conditions, the ion-focusing force can effectively collimate the bunch, so that a small emittance can be obtained following the DLA process.

Figure 4(a) shows the schematic diagram of the system developed to produce plasma waveguides. In the experiments, the Ar gas jet was produced by a 1.6-mm long slit

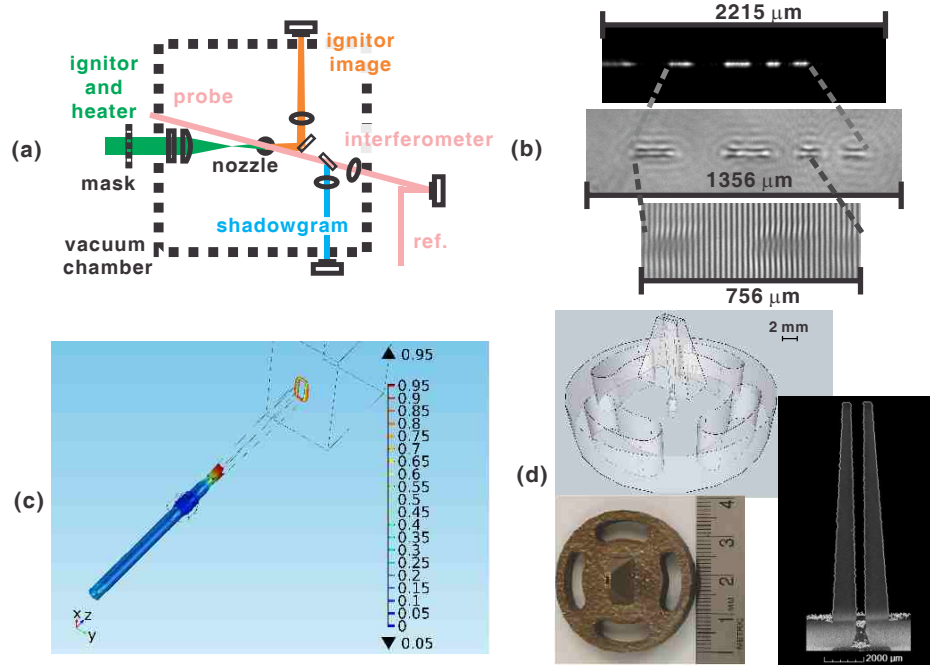


FIGURE 4: (a) Experimental layout of the plasma waveguide shaping system. (b) Intensity-modulated ignitor (upper) and the measured shadowgrams (center) and interferograms (lower) of the corresponding Ar plasma structure. (c) Simulation for the nozzle by COMSOL to examine shockwave development. (d) Final supersonic micrometer slit jet design presented within the surrounding transparent support structure and manufactured in titanium through additive manufacturing.

nozzle, in which a 1.2-mm flat-top density profile can be obtained. By using the 90° geometry, the ignitor and heater beams are overlapped on top of the gas nozzle. The ignitor imaging system is used to monitor the on-target intensity pattern for laser pulse shaping. The shaped axial-structure of plasma waveguide can be diagnosed by the shadowgraphic image and the interferometer. Using of 6.3-mJ ignitor, 36-mJ heater, and an ignitor-heater delay of 100 ps, Fig. 4(b) shows the intensity-modulated ignitor pattern, the corresponding transverse shadowgrams, and interferograms of the density-modulated Ar plasma structure. The ignitor pattern was created by passing the ignitor through a periodically cut mask and then imaging the ignitor with a demagnification of 5 on the target plane. The resulting shadowgrams and interferograms confirm the prediction that the plasma is produced in the regions where the ignitor and heater are spatially overlapped. This result provides the proof-of-principle foundation for producing the density-modulated plasma waveguides via the laser machining technique for future DLA experiments. Supersonic micrometer gas jet nozzles were designed and simulated based upon the de Laval valve using isentropic compressible fluid dynamic as illustrated in Figs. 4(c) and (d). COMSOL Multiphysics high Mach number flow simulation was used to test the isentropic compressible fluid dynamics design solution, to examine the effects of wall friction on the flow, and to identify shock wave development regions in the flow. Computed tomography was used to examine the surface feature size of the nozzles

fabricated from titanium by additive manufacturing techniques at the Pennsylvania State University's Applied Research Laboratory.

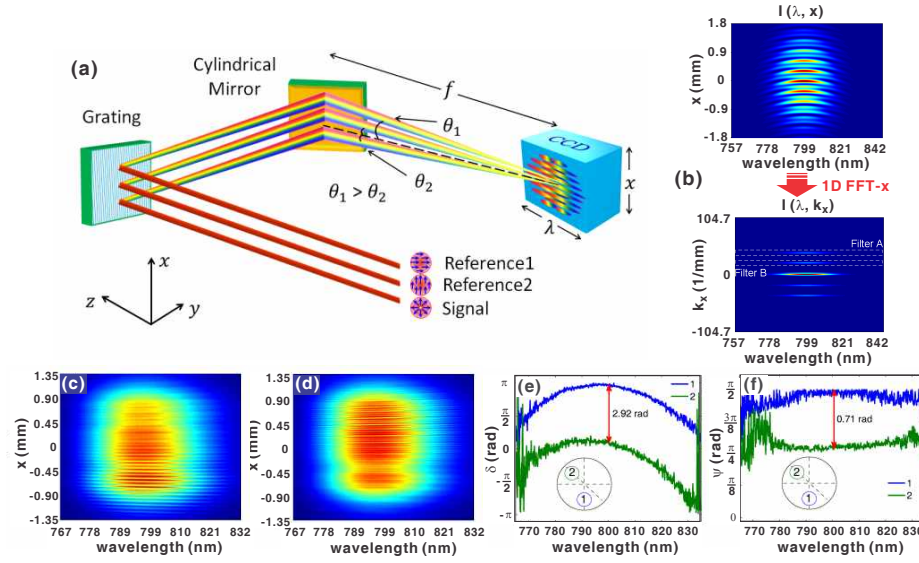


FIGURE 5: (a) Principle of the angle-multiplexed spatial-spectral interferometry. (b) A example for the measured interferogram and the 1D Fourier transform of this interferogram from which the sidebands are extracted (red) and filtered out. Interferograms ((c) and (d)) taken with sampled fields of point 1 (a) and point 2 (b) of a radially polarized pulse illustrated in the inset in (e) and (f). The retrieved (e) relative phases and (f) ellipse orientation angles ψ the the sampled fields.

As shown in Fig. 5(a), a novel technique, having an angularly multiplexed geometry that can record a spatial-spectral interferogram (illustrated in Fig. 5(b)) between an arbitrary polarized signal pulse and two orthogonal linearly polarized reference pulses, is demonstrated for characterizing the polarization state and relative spectral phase of a radially polarized laser pulse. The measurement of relative spectral phase and polarization state of a radially polarized pulse is performed by sampling the fields at the vertical bottom (1) and corner left (2) points illustrated in the insets in Figs. 5(e) and 5(f) with a calibrated 1.5 mm iris. Figures 5(c) and (d) show the interferograms taken with the 2 sampling positions. In Fig. 5(e), the measured difference of the relative phase between those two points at the central wavelength ($\lambda_0 = 800$ nm) is 2.92 rad, close to the expected relative phase of 3.14 rad. The difference in absolute values of polarization angles at central wavelength λ_0 in Fig. 5(f) is 0.71 rad, which is close to the expected value of $\pi/4$.

Publications stemming from this project are listed below:

Dissertation and thesis

- Ming-wei Lin, "Direct laser electron acceleration in a density-modulated plasma waveguide," Ph.D. dissertation, The Pennsylvania State University, University Park, Pennsylvania, 2015 [Online Content](#)

- Bryan Morgan, “Micrometer-Scale Supersonic Slit Jet Nozzle Design, Simulation, and Additive Fabrication for Direct Laser Acceleration,” M.S. Thesis, The Pennsylvania State University, University Park, Pennsylvania, 2015 [Online Content](#)

Journal publications

1. M.-W. Lin and I. Jovanovic, “Test particle simulation of direct laser acceleration in a density-modulated plasma waveguide,” *Phys. Plasmas* **19**, 113104 (2012). DOI: [10.1063/1.4766166](#)
2. A. Rakhman, M.-W. Lin, and I. Jovanovic, “Angle-multiplexed spatial-spectral interferometry for simultaneous measurement of spectral phase and polarization state,” *Opt. Express* **21**, 26897 (2013). DOI: [10.1364/OE.21.026896](#)
3. M.-W. Lin, Y.-L. Liu, S.-H. Chen, and I. Jovanovic, “Particle-in-cell simulations of quasi-phase matched direct laser electron acceleration in density-modulated plasma waveguides,” *Phys. Plasmas* **21**, 093109 (2014). DOI: [10.1063/1.4896245](#)
4. M.-W. Lin and I. Jovanovic, “Direct electron acceleration in plasma waveguides for compact high-repetition-rate x-ray sources,” *J. Phys. B: At. Mol. Opt. Phys.* **47**, 234002 (2014). DOI: [10.1088/0953-4075/47/23/234002](#)

Conference proceedings

1. M.-W. Lin and I. Jovanovic, “Modeling of quasi-phase matching for laser electron acceleration,” in 2011 Particle Accelerator Conference, New York, USA, March 28–April 1, 2011, Paper MOP097.
2. I. Jovanovic and M.-W. Lin, “Modeling and experimental update on Direct laser acceleration,” in 2nd International Particle Accelerator Conference, San Sebastián, SPAIN, September 4–9, 2011, Paper WEPZ010.
3. M.-W. Lin and I. Jovanovic, “Modeling of quasi-phase matching in an aperiodic corrugated plasma waveguide for high efficiency direct laser electron acceleration,” in The International Particle Accelerator Conference IPAC’12, New Orleans, Louisiana, USA, May 20–25, 2012, Paper WEPPP014.
4. M.-W. Lin and I. Jovanovic, “Modeling of aperiodic quasi-phase-matched direct laser electron acceleration,” in Frontiers in Optics/Laser Science FIO/LS 2012, Rochester, New York, USA, October 14–18, 2012, Poster FW3A19.
5. M.-W. Lin, A. Rakhman, D. R. Abercrombie, and I. Jovanovic, “Modeling and experimental update on quasi-phase matched direct laser electron acceleration in density-modulated plasma waveguides,” in 4th International Particle Accelerator Conference IPAC’13, Shanghai, CHINA, May 12–17, 2013, Paper TUPEA089.
6. M.-W. Lin, I. Jovanovic and S.-H. Chen, “3-D PIC Simulation of Quasi-Phase Matched Direct Laser Electron Acceleration with Introduction of a Precursor Electron Bunch,” in The 41st IEEE International Conference on Plasma Science (ICOPS) and the 20th International Conference on High-Power Particle Beams (Beams), Washington DC, USA, May 25–29, 2014, Poster 1P-10.

7. M.-W. Lin and I. Jovanovic, “3-D particle-in-cell simulations for quasi-phase matched direct laser electron acceleration in density-modulated plasma waveguides,” in 5th International Particle Accelerator Conference IPAC’14, Dresden, Germany, June 15-20, 2014, Paper TUMPE046.
8. M.-W. Lin, A. Rakhman, and I. Jovanovic, “Angle-multiplexed spatial-spectral interferometry for simultaneous measurement of spectral phase and polarization state,” in Conference on Lasers and Electro-Optics CLEO:2014, San Jose, California, USA, June 8-13, 2014, Oral presentation STu3E2.
9. M.-W. Lin, I. Jovanovic, Y.-L. Liu and S.-H. Chen, “Quasi-phase-matched direct laser electron acceleration of variable-length electron bunches in plasma waveguides,” in Frontiers in Optics /Laser Science FiO/LS 2014, Tucson, Arizona, USA, October 19-23, 2014, Oral presentation FW5E.5.
10. M.-W. Lin, B. W. Morgan, I. Jovanovic, C.-Y. Hsieh, Y.-L. Liu and S.-H. Chen, “Progress on the Study of Direct Laser Electron Acceleration in Density-Modulated Plasma Waveguides,” in 6th International Particle Accelerator Conference IPAC’15 ,Richmond, Virginia, USA, May 3-8, 2015, Paper WEPJE024.

RECOMMENDATIONS FOR FURTHER ACTION

Our results in plasma waveguide fabrication show that it is important to prevent the ionization of gas atoms by the heater itself; otherwise, the heating of plasma by the inverse bremsstrahlung mechanism is significantly inhibited. The limited heating efficiency of the plasma channel also resulted in significant variations of the length and plasma density distribution among the produced plasma channels. To improve the quality of the produced plasma waveguides, the heating efficiency of plasma has to be increased, such that a well-established plasma density profile with a high on-axis density $> 10^{19} \text{ cm}^{-3}$ and a density barrier $> 5 \times 10^{18} \text{ cm}^{-3}$, which fulfills the guiding condition for the laser pulse, can be realized. An improvement can be made by combining an intensity-modulated, transversely projected ignitor with a heater line focus made by an axicon for producing density-modulated plasma waveguides. When plasma waveguides are well fabricated in the system, a radially polarized pump pulse will be coupled into a plasma waveguide to test the guided propagation and test the injection of external electron bunched for DLA (Phase II of this project). It is noted that larger axial and radial acceleration regions exist in DLA when electrons are injected with a higher initial energy; in this way, a higher overall acceleration efficiency can be realized. Therefore, pre-accelerated electrons, with an initial energy of tens of MeV (from the output of a laser wakefield acceleration (LWFA), for example) can be injected in a density-modulated plasma waveguide for the synchronized co-propagation with the DLA driving pulse. In

this way, an all laser-based acceleration scheme which integrates the injection of electron bunches from a LWFA into a plasma waveguide for the subsequent DLA to higher energies can be accomplished.

DISTRIBUTION LIST
DTRA-TR-16-65

DEPARTMENT OF DEFENSE

DEFENSE THREAT REDUCTION
AGENCY
8725 JOHN J. KINGMAN ROAD
STOP 6201
FORT BELVOIR, VA 22060
ATTN: D. PETERSEN

DEFENSE TECHNICAL
INFORMATION CENTER
8725 JOHN J. KINGMAN ROAD,
SUITE 0944
FT. BELVOIR, VA 22060-6201
ATTN: DTIC/OCA

**DEPARTMENT OF DEFENSE
CONTRACTORS**

QUANTERION SOLUTIONS, INC.
1680 TEXAS STREET, SE
KIRTLAND AFB, NM 87117-5669
ATTN: DTRIAC